UNIVERSITY OF OSNABRUECK

DOCTORAL THESIS

Nanoporous block copolymer stamps:
design and applications

Author   Peilong Hou

Supervisor   Prof. Dr. Martin Steinhart

Institute of Chemistry of New Materials

October 2019, Osnabrueck

To My Two Sons Minmu Hou, Xuwen Hou, and My Wife Feifei Zou.

Table of contents

Abstract

This thesis focuses on the surface patterning by using nanoporous block copolymer (BCP) stamps. Polystyrene-*block*-poly(2-vinylpyridine) (PS-*b*-P2VP) was used as model BCP. Nanoporous BCP stamps were fabricated by replication of lithographically patterned silicon molds. Nanopores inside of BCP stamps were generated by swelling-induced pore formation. A method for scanner-based capillary stamping (SCS) with spongy nanoporous BCP stamps was developed. First, in the course of stamps design using replication molding of PS-*b*-P2VP against surface-modified macroporous silicon molds, PS-*b*-P2VP fiber rings remaining on the macroporous silicon molds were obtained that allow immobilization of water drops on the hydrophobically modified surfaces of the macroporous silicon molds. Water drops immobilized by these rings can be prevented from dewetting within the PS-*b*-P2VP fiber rings. Second, after spongy nanoporous PS-*b*-P2VP stamps had been obtained, preliminary experiments with non-inked PS-*b*-P2VP stamps revealed that parts of the stamps' contact elements can be lithographically transferred onto counterpart surfaces. As a result, arrays of nanostructured submicron PS-*b*-P2VP dots with heights of ~100 nm onto silicon wafers and glass slides were produced. Lastly, the SCS technique was developed, which overcomes the limitation of time-consuming re-inking procedures associated with classical soft lithography including microcontact printing (µCP) and polymer pen lithography (PPL) with solid stamps, as well as the limitations regarding throughput of scanning probe-based serial writing approaches such as nanoscale dispensing (NADIS) and other micropipetting techniques. In addition, sizes of stamped droplets can be controlled by adjusting surface wettability and dwell time.

1. Introduction

Surface patterning techniques, including chemical and topographical patterning of surfaces, by contact lithography provide significant momentum for the advance of modern science and technology. The last past two decades have witnessed the evolution of new surface patterning techniques, which have found applications in the fields of surface chemistry, materials science, microelectromechanical systems, optics, sensing, and cell biology. A variety of methods has been developed to this end. Generally, contact lithography can be divided into two categories based on the patterning strategy: (i) scanning probe-based serial writing approaches yielding arbitrary patterns; (ii) stamp-based parallel stamping approaches producing large-area patterns. The latter group of contact-lithographic approaches includes classical soft lithography with elastomeric stamps [1,2] such as microcontact printing (μCP) [3,4] and polymer pen lithography (PPL) [5-7]. Stamp-based parallel stamping approaches involve the transfer of molecules adsorbed on the stamp surface to a counterpart surface, on which consequently thin ink layers are deposited. Both μCP and PPL rely on solid elastomeric stamps so that continuous ink supply is impossible, resulting in reduced pattern quality without re-inking by adsorption. Scanning probe-based approaches include dip pen nanolithography (DPN) [6-9], micropipetting techniques [10], nanoscale dispensing (NADIS) [11], nanofountain probe (NFProbe) [12], scanning ion pipetting (SIP) [13], nanofountain pen (NFPen) lithography [14], scanning ion conductance microscopy (SICM) [15], and the bioplume technique [16]. Scanning probe-based approaches are usually conducted in a "single pen" fashion. Although they provide great patterning flexibility and high resolution, throughput and the size of the areas that can be patterned are limited such as in the case of DPN. The fabrication of the devices used for lithographic material deposition is also costly and complicated.

On the one hand, parallel stamping methods such as PPL do not allow continuous ink supply and require tedious re-inking procedures. On the other hand, methods based on scanning probe techniques and micropipetting are, while involving continuous ink supply, slow serial methods.

The main goal of this thesis is to develop a micro/nanodroplet stamping technique, scanner-based capillary stamping (SCS) with spongy nanoporous block copolymer stamps, which combines the advantages of state-of-the-art parallel and serial stamping techniques in parallel patterning with continuous ink supply. Thus, parallel stamping operations do not need to be interrupted by re-inking. To this end, stamps penetrated by continuous nanopore networks are designed and applied. In this way, ink can be transferred from the backside of the stamp through the nanopore system to the stamp's contact surface, which is in turn topographically patterned with ink dispensing elements. In addition, the spongy nanopore system itself may act as an ink reservoir. By computer-assisted control of the stamp movement, complicated and arbitrary droplet patterns can be produced. For this purpose, polystyrene-*block*-poly(2-vinylpyridine) (PS-*b*-P2VP) is used to make stamps, and nanopores can be obtained by selective swelling-induced pore formation [17-20].

Wang et al. pioneered generation of nanoporous block copolymer (BCP) nanorods [19,21,22] obtained *via* anodic aluminum oxide (AAO) molds and BCP monoliths [23] by non-destructive swelling-induced morphology reconstruction. BCPs treated with solvents selective to the minority domains selectively swell because osmotic pressure drives the selective solvent into the minority domains. To accommodate the increased volume of the swollen minority domains, the glassy matrix of the BCP majority component undergoes structural reconstruction. Swelling can be quenched by evaporation of the selective solvent, and the extended chains of the minority component undergo entropic relaxation forming pores in place of the swollen minority domains. Therefore, continuous pore networks open to the environment can be produced with adjustable pore diameters depending on the swelling conditions. In ~ 100 μm thick PS-*b*-P2VP substrates bearing PS-*b*-P2VP nanorods (length 1.5 μm, diameter 300 nm) swelling-induced morphology reconstruction in ethanol at 60 °C produced continuous pore systems with P2VP pore walls penetrating the entire specimens, as revealed by porosimetry [23,24], adhesion tests [25] and preconcentration sensing experiments [26]. The pores are permeable for poly(1-decene), glycerin, mineral oil, ethanol and water. What is more, for the obtained pores, contact with

ethanol at room temperature lead to no structure change.

In the course of the stamp design using replication molding of PS-*b*-P2VP against surface-modified macroporous silicon molds, PS-*b*-P2VP fiber rings remaining on the macroporous silicon molds were obtained. These PS-*b*-P2VP fiber rings allow immobilization of water drops on the hydrophobically modified surfaces of the macroporous silicon molds. Water drops immobilized by these rings do not dewet within the PS-*b*-P2VP fiber rings. Discrete water drops immobilized on substrates have been explored for a diverse range of applications including the trapping of bioactive molecules, nonadherent cells, and microorganisms [27]. Moreover, immobilized water drops are employed for enzymatic reactions [28], synthesis and profiling of enzyme inhibitors [29], combinatorial discovery of fluorescent pharmacophores [30], high-throughput screenings of embryonic stem cells [31], whole-organism screenings using fish embryos [32], as well as for the creation of cell type patterns [33], microdrop-derived hydrogel particles [34], and metal-organic framework (MOF) microstructures [35]. The most common and viable method to immobilize water drops is the use of hydrophobic-hydrophilic micropatterns: The water drops are located on hydrophilic areas bordered by hydrophobic areas. Such chemically patterned substrates are typically produced by top-down lithographic methods including photolithography and μCP [27,36-38]. Immobilization of water drops on hydrophobic surfaces has generally been realized only by means of 3D topographic patterns, such as geometric poly(dimethylsiloxane) (PDMS) obstacles [28], hydrophobic Si pillars [39], and superhydrophobic black silicon indentations generated by photolithography and deep reactive ion etching [40]. Therefore, it is highly attractive to immobilize water drops on hydrophobic surfaces that are typically inert, repulsive to adsorbates and characterized by antifouling behavior.

After spongy nanoporous PS-*b*-P2VP stamps had been obtained, preliminary experiments with non-inked PS-*b*-P2VP stamps revealed that parts of the stamps' contact elements can be lithographically transferred to counterpart surfaces. Therefore, arrays of nanostructured

submicron PS-*b*-P2VP dots with heights of ∼100 nm can be generated on silicon wafers and glass slides. BCPs are an interesting class of materials because they may combine the specific properties of their chemically distinct blocks. In the case of the BCP PS-*b*-P2VP, the nonpolar PS blocks may serve as rigid glassy scaffold. The polar P2VP blocks can be functionalized taking advantage of the presence of the pyridyl group in each P2VP repeat unit. Lithographic deposition of BCPs by a parallel lithographic process would be a powerful approach to pattern and to functionalize surfaces but has not yet been established.

Finally, the SCS technique is developed that overcomes the need of time-consuming re-inking in classical parallel stamping methods based on the use of solid stamps including μCP and PPL, as well as the low-throughput of scanning probe-based serial writing approaches such as in the case of NADIS, by the use of porous stamps. In addition, sizes of stamped droplets can be controlled by adjusting surface wettability and dwell time.

This thesis is organized in the following manner. Chapter 2 describes the relevant state-of-the-art. Chapter 3 deals with the immobilization of water drops on hydrophobic surfaces by contact line pinning on PS-*b*-P2VP fiber rings protruding from macroporous silicon molds. Chapter 4 focuses on sacrificial stamping of nanororous PS-*b*-P2VP nanodots onto substrates. In Chaper 5, the main goal of this thesis, the establishment of the SCS technique, is discussed. The last Chapter contains a brief summary and an outlook.

2. State of the art

2.1. Immobilization of microdroplet arrays

Microdroplet arrays are important for a wide range of applications including cell-based high-throughput screenings [27], hydrogel micropads [34], polymer deposition [41-43], nanoparticle assembly [44], sensor microchips [45,46], and microreactors [30]. Generally, methods for immobilization of microdroplet arrays can be divided into two strategies: (i) using physical topographical patterns; and (ii) using chemical patterns.

2.1.1. Formation of microdroplet arrays using physical topography patterns

Commercial microtiter plates used as physical topographical patterns for immobilization of microdroplet arrays have important advantages such as simple indexing of each well and easy time-lapse measurements. Moreover, the physical walls within microtiter plates prevent chemical and optical crosstalk between neighboring wells. However, common commercial microtiter plates are 96-, 384-, and 1536-well microtiter plates [47,48]. It is challenging to deal with large numbers of samples using conventional microtiter plates. Therefore, the increase of the well densities of microtiter plates by miniaturization becomes more and more important. The Whitesides group produced large, up to 45 cm^2, arrays of microwells with well diameters down to 2 μm and high densities of 10^7 wells/cm^2 on PDMS substrates (Figure 2.1A), and filled these microwells arrays uniformly and rapidly with solutions using a method termed as discontinuous dewetting (Figure 2.1B,C), which occurs when a drop of liquid drains from a surface bearing discrete depressions and having a surface free energy lower than that of the liquid. The holes remain filled as the liquid dewets the surface of the material [49]. Whitesides' group also fabricated arrays of small crystals (Figure 2.1D) encapsulated in the microwells with control over their size, orientation, and arrangement in space [50].
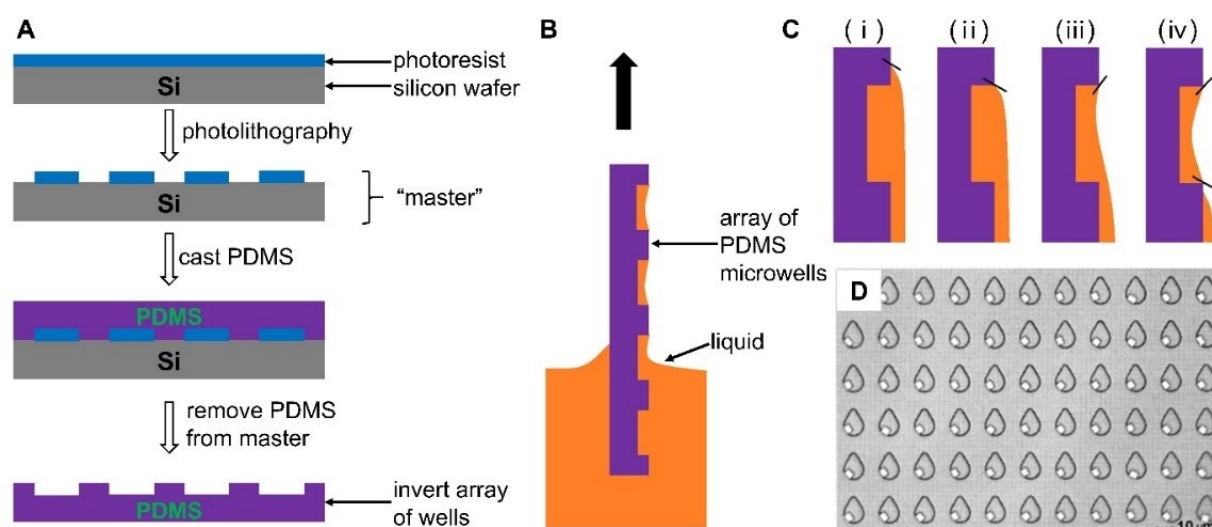
Figure 2.1. (A) Schematic illustration of the fabrication of microreactor wells. Master mold produced by photolithography using either a chrome mask or a high-resolution transparency mask. PDMS prepolymer was cast against the master. After curing the PDMS at 65 °C for 2h, the PDMS mold patterned with microwell arrays was removed from the master. (B) Schematic illustration of the filling of an array of microreactors with liquid by discontinuous dewetting. (C) Tangent on the liquid surface indicating the liquid contact angle during discontinuous dewetting. (D) Optical image of ordered arrays of KBr microcrystals with a density of 2×10^5 crystals cm^{-2}. (A–C) are adapted with permission from ref [49]. Copyright 1998 American Chemical Society. (D) is adapted with permission from ref [50]. Copyright 2002 American Chemical Society.

2.1.2. Formation of microdroplet arrays using chemical patterns

Another approach for creating microdroplet arrays is to generate chemical patterns. The Whitesides group developed a strategy that uses patterned, self-assembled monolayers (SAMs) of alkanethiolates on gold substrates to organize two immiscible liquids, such as in the case of water and hydrocarbon, in contact with the SAM into simple three-dimensional microstructures at its surface by using selective wetting [51]. In recent years, Levkin and co-workers fabricated microdroplet arrays using superhydrophilic-superhydrophobic patterns [27,33,52-60], and reported various applications for microdroplet arrays, including their use as high-density cell microarrays (Figure 2.2C,E) [61] and the investigation of cell-cell communication [33]. The Levkin group also fabricated superhydrophilic micropattern arrays on superhydrophobic

substrates. When an aqueous solution moves over a superhydrophilic-superhydrophobic patterned surface (Figure 2.2A), the discontinuous dewetting effect [49] arising from the difference in water contact angles between the superhydrophilic and superhydrophobic regions can be utilized to passively dispense aqueous solution into the superhydrophilic micropatterns without wetting the superhydrophobic matrix (Figure 2.2B,C) [61].
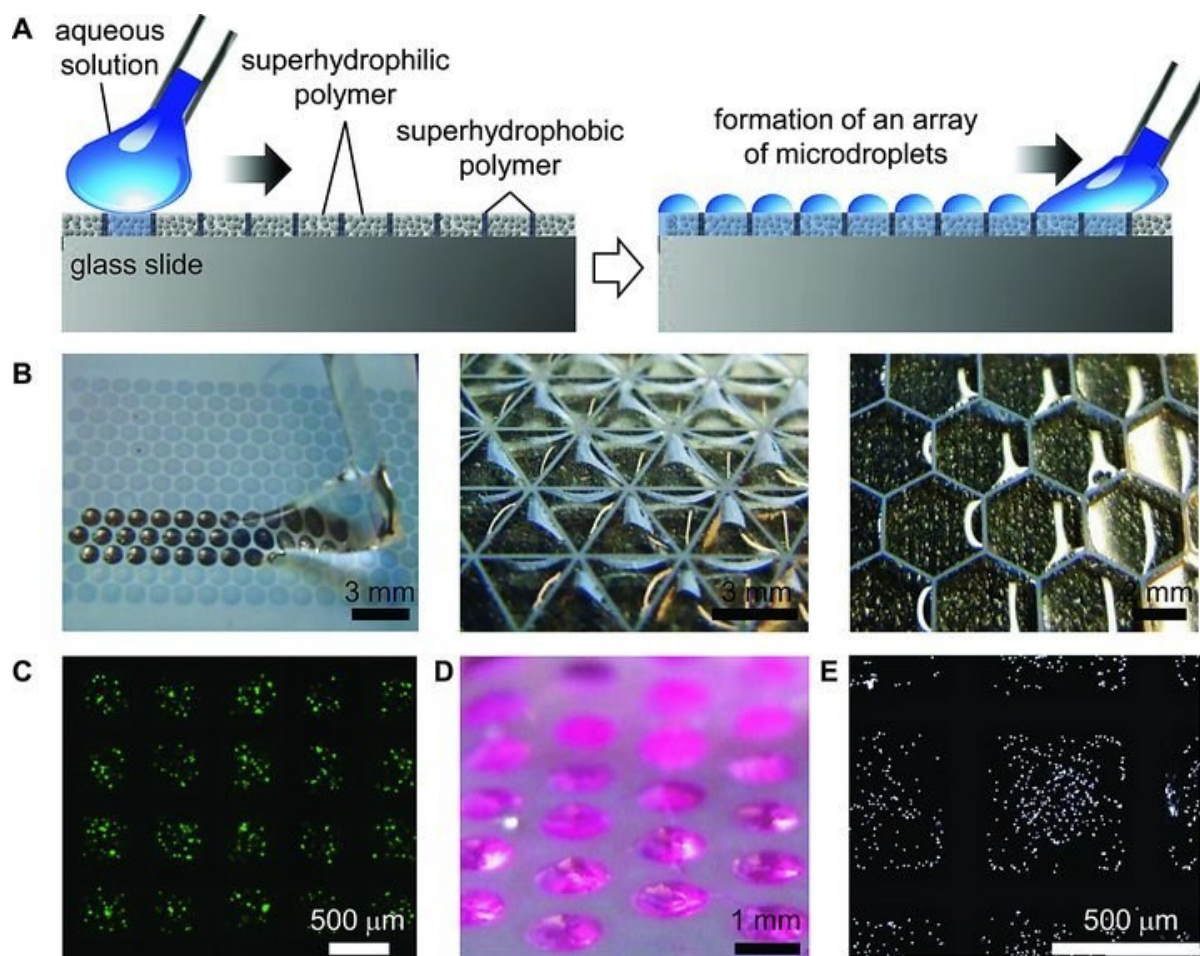
Figure 2.2. Formation of microdroplet arrays for encapsulating of cells in arrays of microdroplets and hydrogel micropads. (A) Schematic illustration of an aqueous solution being rolled over superhydrophilic-superhydrophobic patterns. The wettability contrast of superhydrophilic spots on a superhydrophobic matrix leads to the formation of a high-density array of completely separated microdroplets. (B) Optical images of water being rolled along superhydrophilic-superhydrophobic patterns to form droplets in the superhydrophilic spots. (C) Fluorescent HeLa-GFP cells cultured in each microdroplets. (D) Hydrogel micropads coloured with Rhodamine 6G. (E) DAPI-coloured (white) human stem cells encapsulated in hydrogel micropads. Reproduced with permission from ref [61]. Copyright 2013 Wiley-VCH Verlag GmbH & Co. KGaA, Weinheim.

Immobilization of water drops on hydrophobic surfaces has generally been realized only by means of 3D topographic patterns, such as in the case of geometric PDMS obstacles [28]. On the other hand, water drops immobilized by chemical patterns can generally be located in the hydrophilic areas. Therefore, it is highly attractive to immobilize water drops on hydrophobic surfaces that are typically inert, repulsive to adsorbates and characterized by antifouling behavior.

2.2. Sacrificial printing

The principle of sacrificial printing is common in our everyday life. Scientists applied the principle of sacrificial printing to nanofabrication, producing nanoscale patterns. Ha and coworkers developed a PDMS pattern-transfer technique termed as buffered-oxide etchant (BOE) printing [62] (Figure 2.3). The principle of the BOE printing was investigated by considering the strong adhesion force between the BOE-treated PDMS and the SiO_2 substrate. PDMS patterns with feature sizes ranging from a few micrometers to the sub-micrometer size were transferred to the SiO_2 substrate by pressing a stamp that had been immersed in BOE solution onto the SiO_2 substrate.

Lu and coworkers reported a surface treatment-assisted transfer printing technique, named as switchable transfer printing (sTP) [63] (Figure 2.4). In the sTP technique, both patterned stamps and substrates were made of PDMS. Initially, both patterned stamps and substrates were somewhat soft that can be defined as "soft" sides. These "soft" sides can be finely switched to be "hard" sides by a surface oxidation treatment. When pressing a "soft" side of the stamp to a target "hard" side of the substrate, thin films of the stamp can be transferred to the substrate. Similarly, when pressing a "hard" side of the stamp to a target "soft" side of the substrate, thin films of the substrate can be transferred to the surface of the stamp.

At the moment, there are few publications about sacrificial printing. Moreover, materials used

for sacrificial printing are limited to PDMS.
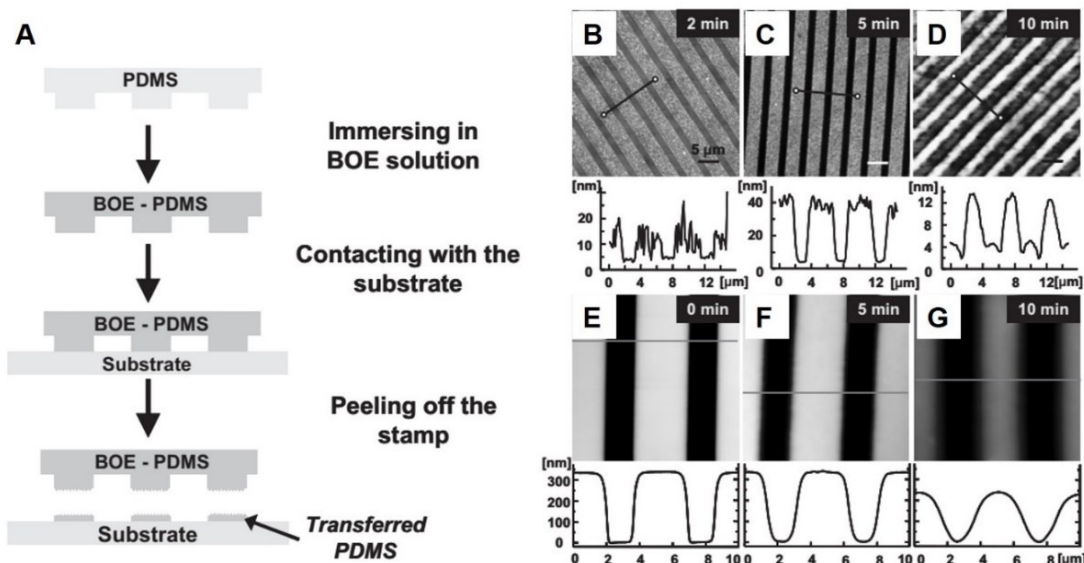
Figure 2.3. BOE-printing. (A) Schematic illustration of the BOE-printing procedure. AFM images and line profiles of the SiO$_2$ substrates patterned with a BOE-treated PDMS stamp that was treated in BOE solution for (B) 2 min, (C) 5 min, and (D) 10 min. (E–G) AFM images and line profiles of BOE-treated PDMS stamps with treated times of 0 min, 5 min, and 10 min. Adapted with permission from ref [62]. Copyright 2007 Wiley-VCH Verlag GmbH & Co. KGaA, Weinheim.
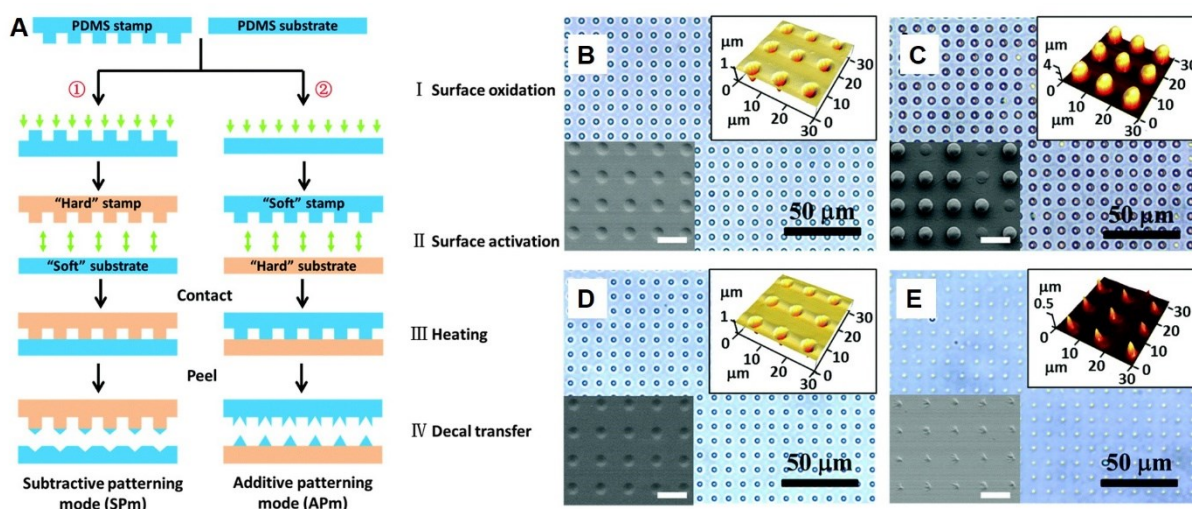
Figure 2.4. Surface treatment-assisted switchable transfer printing (sTP). (A) Schematic illustration of the sTP process to pattern the PDMS substrate in the SPm and APm switchable transfer modes, in the case of the combination of "hard" stamp/"soft" substrate (①) and "soft" stamp/"hard" substrate (②), respectively. (B–E) Optical images of the resulting patterned PDMS substrates. Adapted with permission from ref [63]. Copyright 2016 Royal Society of Chemistry.

2.3. Techniques for droplet printing

Manipulation of liquids by dispensing them at the femtolitre level (corresponding to micron features) in a controlled way has increasing relevance to applications such as surface patterning, surface modification, localized growth, engineering of bioarrays and bottom-up fabrication of devices.

Various methods are available for manipulating droplets at different volume ranges with the aim to allow deposit any soluble molecules with high spatial resolution [64]. The range of feature sizes made by these techniques spans 12 orders of magnitude in deposited volumes from the microliter range to the attoliter range, as shown in Figure 2.5.
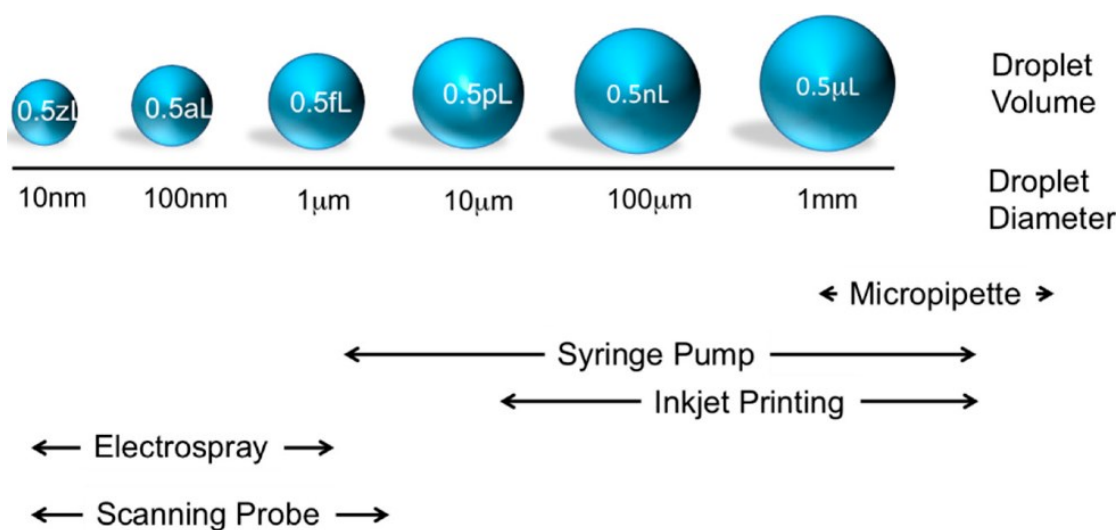
Figure 2.5. Various dispensing techniques as well as the characteristic droplet diameters and droplet volume ranges associated with the dispensing techniques. Reproduced with permission from ref [64]. Copyright 2014 MDPI.

Generally, droplet patterning methods can be divided into two different categories: ballistic non-contact methods and contact methods. Non-contact methods comprise deposition of droplets onto the counterpart surface by a droplet ejector, such as in the case of inkjet printing. Contact methods transfer droplets to the substrate *via* the liquid meniscus formed between a dispensing element/pen and the counterpart surface.

2.3.1. Liquid delivery by non-contact methods

The non-contact method involves the ejection of droplets from a nozzle located above the substrate using different strategies. The non-contact method has the advantage to be compatible with any type of substrates, especially with substrates having curved surfaces.

2.3.1.1. Inkjet printing

Inkjet printing is a mature technique that has had significant commercial success in digital printing for several decades [65,66]. In the inkjet printing, liquid droplets are ejected through a nozzle. The inkjet printing techniques can be categorized into two general classes, as illustrated in Figure 2.6. One is the "continuous inkjet" (CIJ) technology, and the other one is "drop-on-demand" (DOD) printing. In the CIJ technology, a continuous stream of liquid droplets is produced and oriented toward the substrate or deflected by an electric field on a droplets collector. In the DOD printing, the liquid is emitted through the nozzle to form a short jet, which then condenses into a droplet only as it is needed. The droplet diameters used in inkjet printing, typically from 10 to 100 μm, correspond to drop volumes from 0.5 to 500 picoliter. The direct printing of droplets with sizes much smaller than 10 μm is rather difficult, if not impossible.
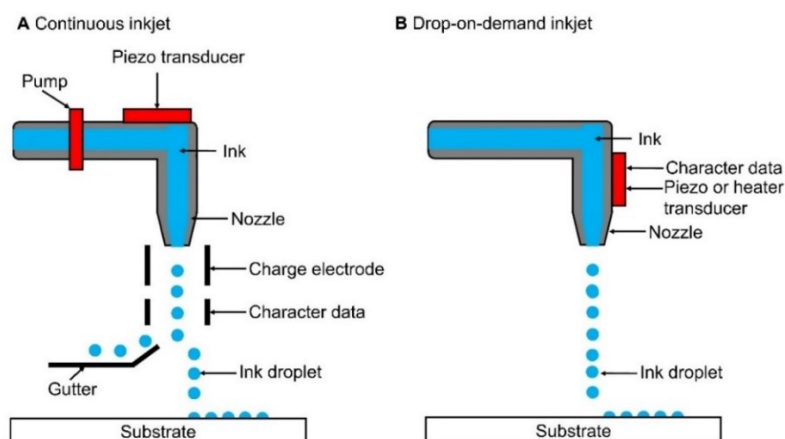
Figure 2.6. Two inkjet printing approaches: (A) continuous inkjet printing and (B) drop-on-demand inkjet printing. Adapted with permission from ref [66]. Copyright 2012 Emerald Publishing Limited.

2.3.1.2. Electrohydrodynamic jet printing

Electrohydrodynamic jet printing (e-jet printing) (Figure 2.7A) uses an electric field-induced flow through microcapillary nozzles to deliver the ink onto a substrate [67]. In the e-jet printing, a syringe is connected to a nozzle, usually a glass capillary, to deliver the liquid ink. A voltage is applied, between the nozzle and the substrate, to drive the ink onto the counterpart substrate. When a suitable voltage is applied between the nozzle and the electrode, an electric field is generated that drives the ions to the nozzle. As the ions in the ink accumulate near the tip of the nozzle, mutual Coulomb repulsion among the ions deforms the meniscus into a conical shape, termed as the Taylor cone [68,69]. When the electrostatic stress overcomes the surface tension at the tip of the Taylor cone, the ejection of the ink from the Taylor cone will be realized.
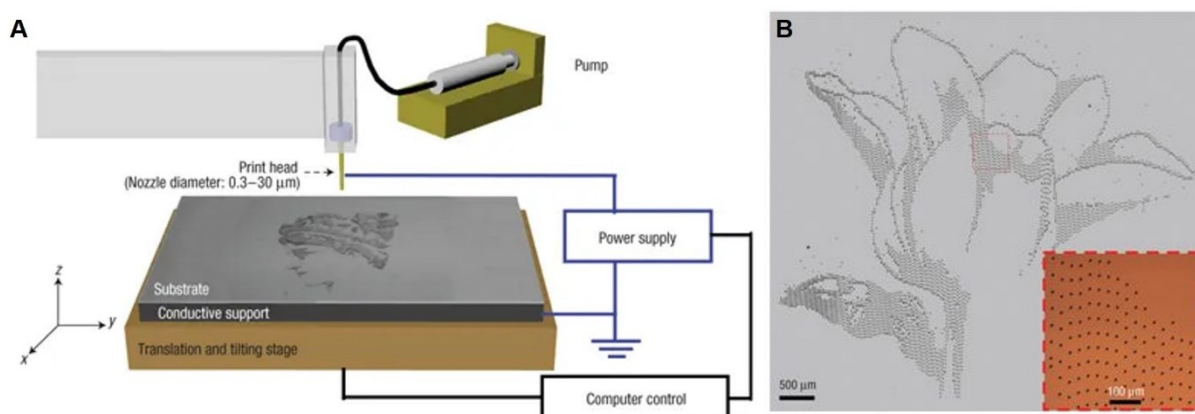
Figure 2.7. Schematic illustration of the e-jet printing (A) and image of a flower (B) printed by e-jet printing. The dots (about 10 μm in diameter) are composed of SWNTs, printed with a nozzle with internal diameter of 30 μm. Adapted with permission from ref [70]. Copyright 2007 Springer Nature.

Rogers' group adapted the e-jet printing method to print high-resolution patterns [70,71]. Figure 2.7B [70] shows an image of a flower that composed of printed dots (average diameter ~10 μm) of single-walled carbon nanotubes (SWNTs) deposited as aqueous solution by e-jet printing. Rogers' group also used a much finer nozzle (500 nm inner diameter) to generate dots with diameters of about 490 nm. High-resolution e-jet printing overcomes the resolution limitation of conventional ink-jet printing. However, the construction of micrometer and sub-micrometer-

sized electrically conductive nozzles with a high reproducibility is still complex and intricate, and the need of conductive substrates or specific electrode configurations limits the applicability of e-jet printing.

2.3.1.3. Pyroelectrodynamic printing

When a liquid is subjected to a sufficiently strong electric field, the emission of thin fluid jets from conical tip structures that form at its surface can be induced [72]. Vespini and coworkers described a method to draw attoliter-sized liquid droplets from one or multiple sessile drops or liquid film reservoirs using a pyroelectrohydrodynamic dispenser [73]. Local pyroelectric forces, which are activated by scanning a hot tip or an infrared laser beam over a lithium niobate substrate, draw liquid droplets from the reservoir below the substrate, and deposit them on the underside of the lithium niobate substrate (Figure 2.8A) [73]. Vespini's group also pointed out that the pyroelectrodynamic printing technique is able to produce droplets with much reduced dimensions by decreasing the volume of the drop reservoir (for example, after a certain number of shots) (Figure 2.8B,C). The smallest dispensed droplets had volumes as low as about 3.6 aL and radii of about 300 nm. This technique has several advantages compared with e-jet printing, including: (i) The ink itself does not need to be conductive. (ii) The pyroelectrodynamic printing system does not require electrodes, nozzles or circuits, and is expected to have many applications in biochemical assays and various transport and mixing processes. However, all components used need to be thermally stable and non-volatile.
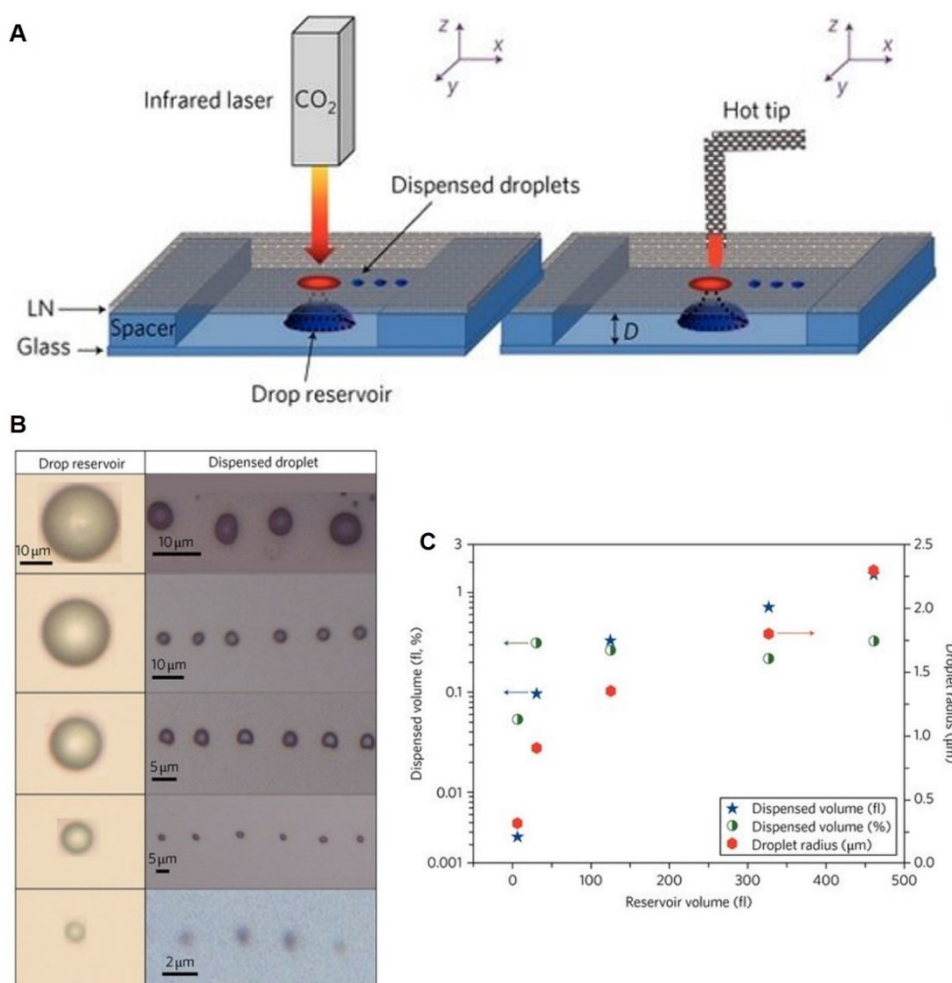
Figure 2.8. Pyroelectrodynamic printing. (A) Schematic illustration of the microfluidic system consisting of two plates and a heat source (an IR laser or hot tip of a conventional soldering iron). (B) Optical images of different drop reservoirs and corresponding dispensed tiny droplets of oleic acid. (C) Corresponding volume and radius values of the dispensed droplets versus those of the reservoir (the left y-scale is logarithmic). Adapted with permission from ref [73]. Copyright 2010 Springer Nature.

2.3.1.4. Acoustophoretic printing

Lewis and coworkers reported an acoustophoretic printing method that enables drop-on-demand patterning of a wide range of soft materials, including Newtonian fluids with viscosities span more than four orders of magnitude (0.5 to 25,000 mPa·s) [74]. By using the acoustic properties of a subwavelength Fabry-Perot resonator, they have produced an accurate, highly localized acoustophoretic force that can exceed the gravitational force by two orders of magnitude to eject microliter-to-nanoliter volume droplets (Figure 2.9A). When the

acoustophoretic force dominates the gravitation force ($F_a > 10F_g$), droplets can be ejected in any direction by rotating the printing platform in space. By controlling the acoustophoretic force and the nozzle diameter, diameters of the printed droplets can be adjusted (Figure 2.9B). In addition, acoustophoretic forces are independent from any electromagnetic properties. Therefore, acoustophoretic printing has an advantage over e-jet printing that requires the ink to have specific electromagnetic properties.
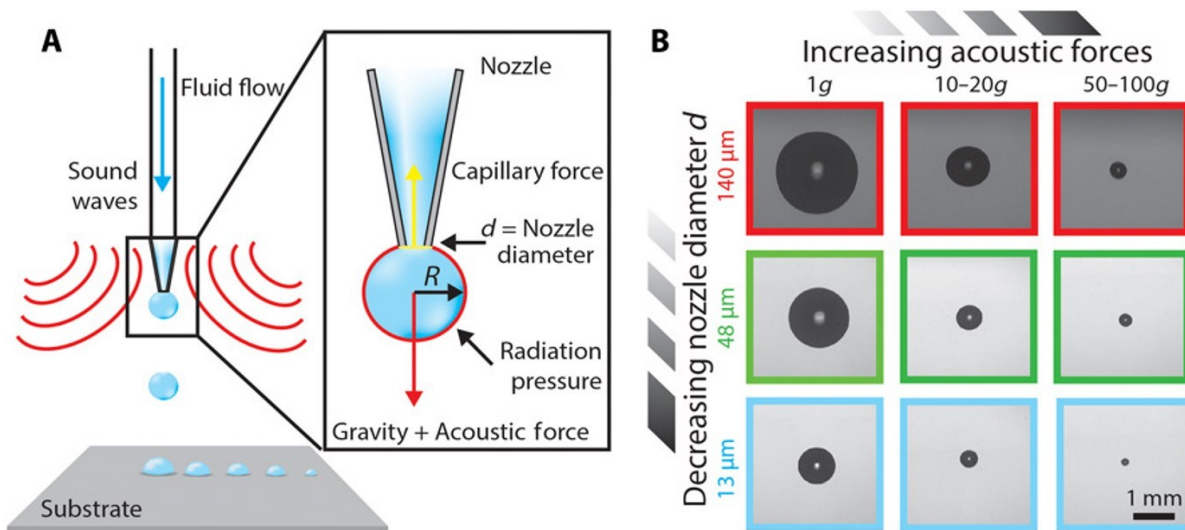
Figure 2.9. Acoustophoretic printing. (A) Schematic illustration of the acoustophoretic printing, in which the radiation pressure provides an additional force that aids drop formation and ejection. (B) Optical images of droplets formed as a function of varying acoustophoretic forces and nozzle diameters. Adapted with permission from ref [74]. Copyright 2018 AAAS.

2.3.2. Liquid delivery by contact methods

The contact method uses stamps, solid tips or extremities of capillaries to touch the surface to be patterned, allowing inks to be transferred or fluidic drops to be deposited, respectively. The contact method is a passive delivery technique using adsorption processes or capillary forces acting on the liquid. Therefore, there is no need for liquid actuation, and the corresponding setups are, therefore, often simpler than in the case of ballistic printing. Generally, contact methods comprise parallel stamping approaches such as in the case μCP [1], and serial writing approaches like DPN [8].

2.3.2.1. Microcontact printing

Whitesides and coworkers developed the µCP technique [1] using elastomeric stamps with reliefs on their surface to generate patterned SAMs on both planar and curved substrates (Figure 2.10). The µCP technique is experimentally simple and inherently parallel. The elastomeric stamps are fabricated by casting and polymerizing PDMS prepolymer in master molds, which are usually prepared by photolithography. Ink is adsorbed on the surface of the stamp. Then, the inked stamp contacts the counterpart substrate and transfers the ink onto the surface of the latter.
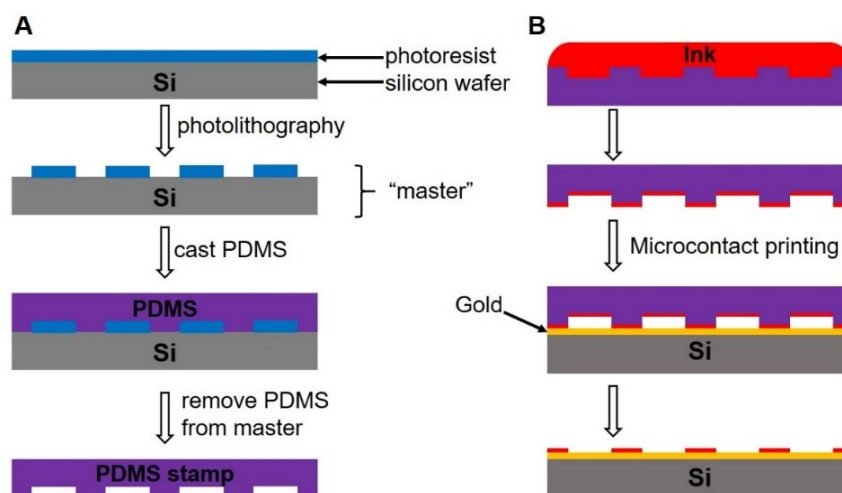
Figure 2.10. Microcontact printing (µCP). (A) Procedure for the fabrication of the PDMS stamp. Photolithography using either a chrome mask or a high-resolution transparency mask produced a master. PDMS prepolymer is cast against the master. After curing, the PDMS stamp is removed from the master. (B) Schematic illustration of the µCP procedure. Thiol is adsorbed on the stamp.Thiols bind to a gold-coated counterpart surface in the areas where the stamp contacts the gold-coated substrate. Adapted with permission from ref [1]. Copyright 1998 ANNUAL REVIEWS, INC.

2.3.2.2. Dip pen nanolithography

Butt et al. first demonstrated the use of a cantilever tip to deposit aggregates of octadecanethiol onto mica using an AFM [75]. Deposition occurs immediately after contact between the tip and the mica substrate or starts from small, randomly placed spots that grow during scanning.
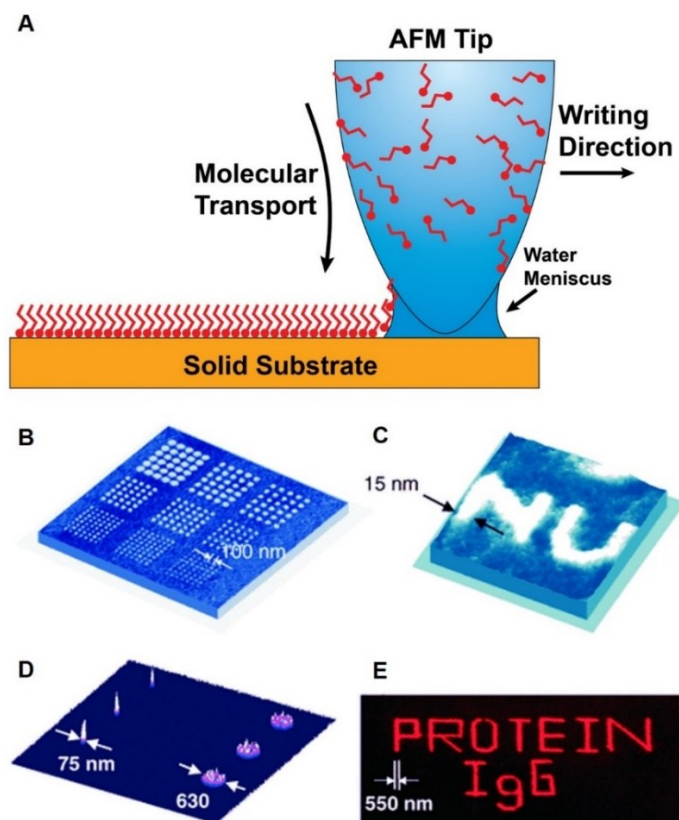
Figure 2.11. Schematic illustrating of the DPN technique (A) and fabricated patterns. (B) Nanoscale dot arrays written on a polycrystalline Au surface with MHA by DPN and (C) nanoscale letters written on an Au (111) surface with MHA by DPN. (D) AFM image of gold nanoparticles hybridized to surface DNA templates generated with direct-write DPN. (E) Fluorescence image of direct-write DPN patterns of fluorescently labeled immunoglobulin G (IgG) on SiO$_x$ substrate. (A) is adapted with permission from ref [8]. Copyright 1999 AAAS. (B–D) are adapted with permission from ref [76]. Copyright 2004 WILEY-VCH Verlag GmbH & Co. KGaA, Weinheim.

Later, Mirkin and coworkers reported a direct-write method termed as DPN based on an AFM that works under ambient conditions (Figure 2.11) [8]. The ink adsorbed onto the AFM tip is delivered to the substrate by a water meniscus that forms between the tip and the surface (Figure 2.11A). This meniscus serves as a medium for ink transport with nanometric precision. Early results showed that DPN could be used to pattern alkanethiol SAMs onto gold surfaces with high-resolution and registration (Figure 2.11A,B) [8,77,78]. Importantly, it was also shown that DPN technique offered the ability to pattern multiple chemical species with sub-100-nm alignment. It was also shown that DPN-defined SAMs were of high-quality (crystalline in the case of 1-octadecanethiol (ODT) and 16-mercaptohexadecanoic acid (MHA; thiohexadecanoic

18

acid)). DPN has also been developed to pattern a variety of "ink-substrate" combinations, from small organic molecules, to organic and biological, polymers (Figure 2.11C,D), and from colloidal particles, to metal ions and sols. DPN can be used to pattern surfaces ranging from metals to insulators and to pattern on top of functional monolayers adsorbed on a variety of surfaces.

2.3.2.3. Polymer pen lithography

Also, the Mirkin group developed the PPL technique [5], which combines the features of DPN and μCP while eliminating many of the limitations of the two techniques. A typical PPL array (Figure 2.12A–C) is made from an elastomer, which is cured in a Si mold and then mounted on a flat, transparent substrate (glass). The array is then used in an AFM as one would use a cantilever in a DPN experiment. They have fabricated PPL arrays with up to ~11,000,000 pens, which allows high-throughput, large-scale patterning at a low cost. In addition, in PPL, tip-substrate contact force can be used to control feature size that allows rapid generation of micro and nanoscale features by varying the compression of the tips. By using the Si master that has an inkwell [79], multiplexed patterns can be generated by individually addressing each tip with different inks (Figure 2.12D). This methodology is an example of scanning probe lithography performed in a cantilever-free mode: the tip is used as both the spring and printing tool. Mirkin's group used protein patterns made by PPL to address fundamental questions pertaining to cell-surface interactions and stem cell growth and differentiation.
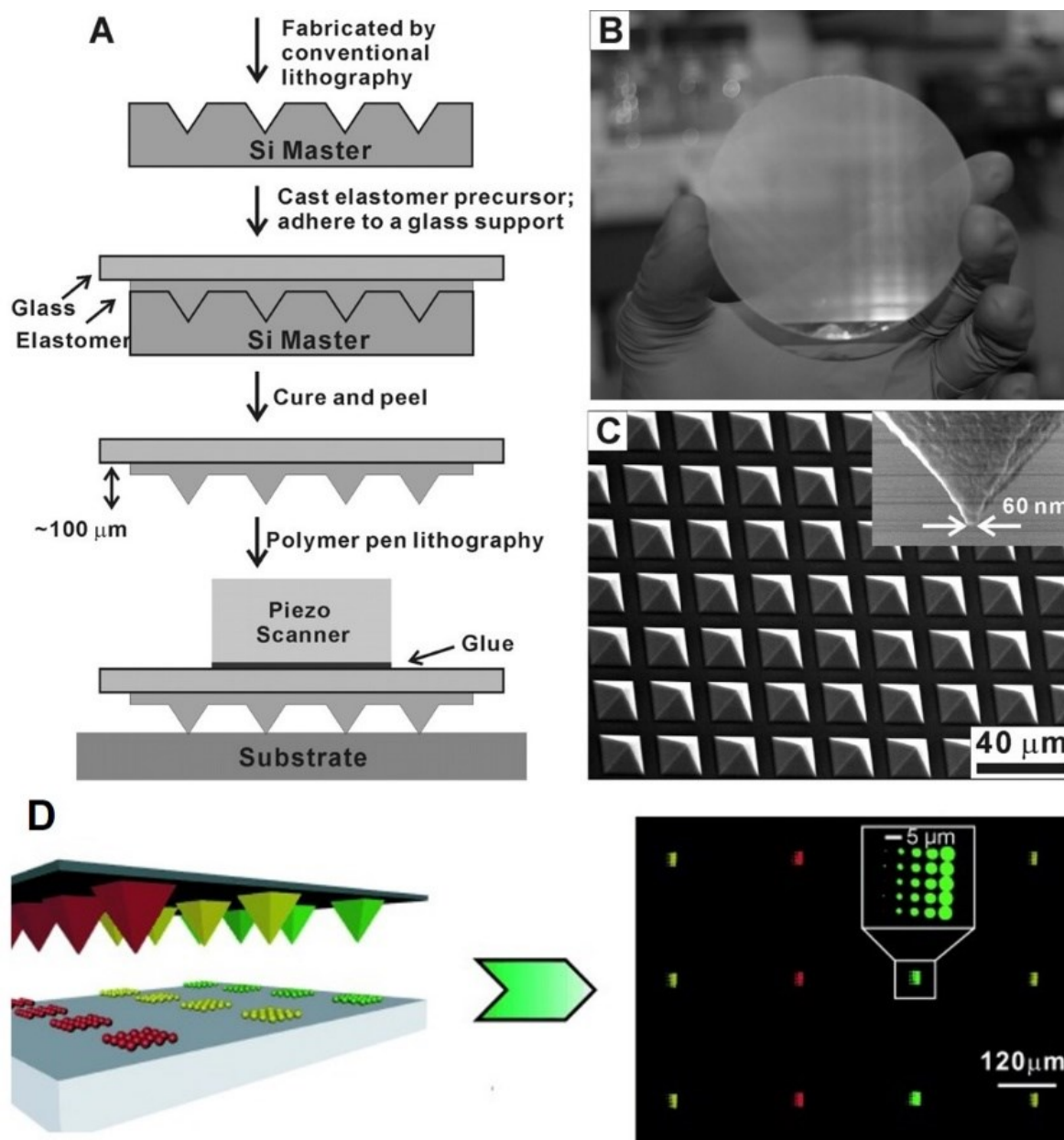
Figure 2.12. (A) Schematic illustration of the PPL setup. (B) Photograph of an 11-million-pen array. (C) SEM image of the polymer pen array. (D) Schematic representation of multiplexed protein printing by PPL and fluorescence image of the resultant multiplexed PPL patterns of fluorophore-labeled proteins patterns. (A–C) are adapted with permission from ref [5]. Copyright 2008 AAAS. (D) is adapted with permission from ref [79]. Copyright 2009 WILEY-VCH Verlag GmbH & Co. KGaA, Weinheim.

2.3.2.4. Material deposition by micropipetting and scanning probes with integrated ink supply

Micropipettes are common equipment in wet labs to manipulate liquids with controlled volumes.

Klenerman and coworker described a nanopipetting technique for controlled chemistry in small arrayed water droplets using a double-barrel pipet (Figure 2.13) [10]. Glass-fabricated double-barrel nanopipets were fabricated to controllably produce arrayed water droplets with volumes as small as a few attoliters under an organic layer.
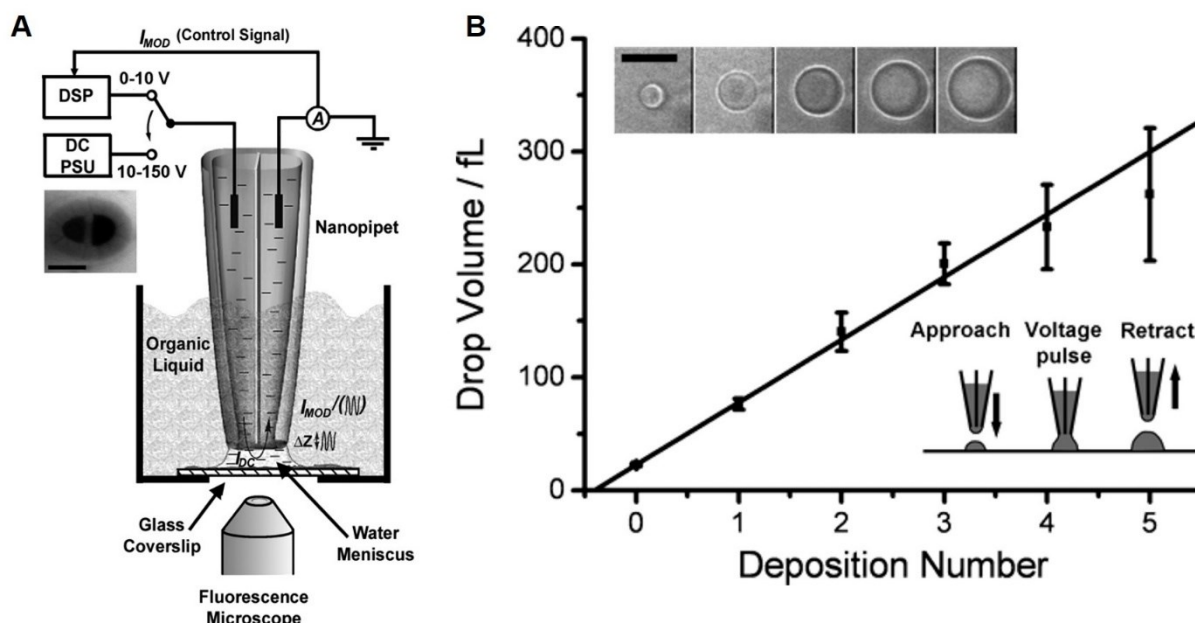
Figure 2.13. Nanoscale Pipetting. (A) Schematic illustration of the apparatus. (B) Linear fit to the increase in drop volume with subsequent addressing. The top inset shows representative optical images of an initial drop and its increases in size with four subsequent addressing pulses (scale bar: 5 μm). The bottom inset shows the process of sequential addressing of a droplet. Adapted with permission from ref [10]. Copyright 2006 American Chemical Society.

The Yu group developed an electrodeposition method that exploited the thermodynamic stability of a microscale or nanoscale liquid meniscus to "write" pure copper and platinum three-dimensional structures of designed shapes and sizes in an ambient air environment (Figure 2.14A–C) [80]. They demonstrated an automated wire-bonding process that enabled wire diameters of less than 1 micrometer and bond sizes of less than 3 micrometers, with a breakdown current density of more than 10^{11} amperes per square meter for the wire bonds (Figure 2.14D–H). This technology can also be further used to fabricate high-density and high-quality interconnects, as well as complex three-dimensional microscale and even nanoscale metallic structures.
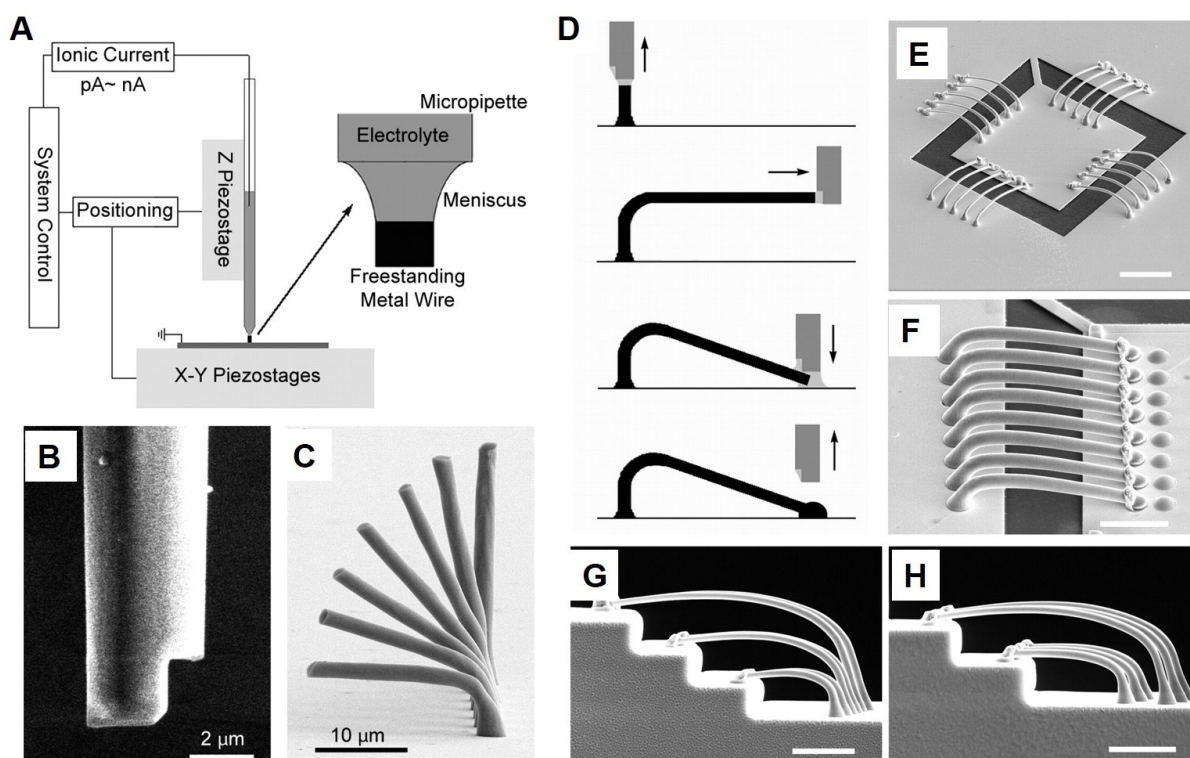
Figure 2.14. Meniscus-confined 3D electrodeposition using micropipette. (A) Schematic illustration of the setup. (B) SEM image of the nozzle. (C) Electrodeposited Cu wires with different inclination angles fabricated with the use of a side-cut micropipette. (D) Schematic showing the steps involved in the wire-bonding process with the meniscus-confined 3D electrodeposition. (E) SEM image of the 20 electrodeposited interconnects. (F) SEM image of the uniform quality of the first and the second bonds. (G) SEM image of the multilayered interconnection over three steps of 5 μm each in height. (H) SEM image of the overlap interconnects over steps of 5 μm in height. Scale bar, 10 μm. Adapted with permission from ref [80]. Copyright 2010 AAAS.

For controlled dispensing of small volumes of attolitre (10^{-18} L; aL) to zL volumes, scanning probe microscope (SPM) based techniques with integrated ink supply can be used. SPM methods take advantages of high resolution of the AFM resulting so far in the minimum feature sizes patterned by add-on processes (sub-100 nm). There are many approaches in SPM techniques, detailed hereafter.

Ondarçuhu and coworkers developed nanoscale dispensing (NADIS) of liquid through an apertured AFM probe milled by focused ion beam lithography (Figure 2.15) [11]. In NADIS, the size of deposited droplets can be reproducibly defined by controlling the aperture size on

the probe and the surface energies of both tip outer wall and substrate surface. Tips with aperture diameters as small as 35 nm enabled the deposition of regular arrays of nanodroplets with diameters down to 70 nm on an alkylamine-modified surface. The fine control of droplet volumes down to a few tens of zeptoliters (10^{-21} L) provides a tool for creating devices and probing the fundamentals of wetting at the nanometer scale.
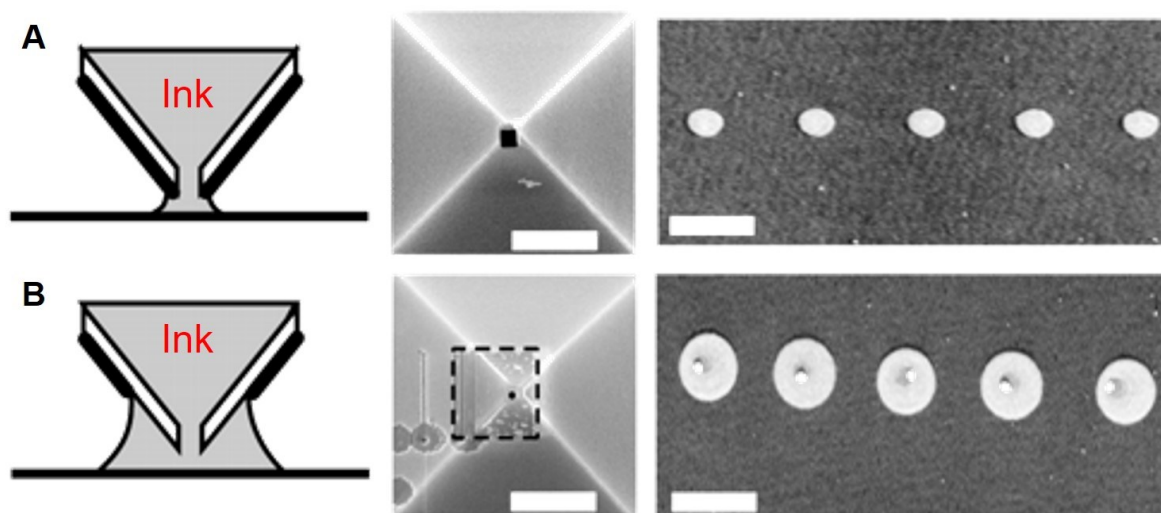
Figure 2.15. NADIS technique. Deposition on amine-treated surface with functionalized tips. The liquid meniscus is schematized on the left with the thick black part of the tip corresponding to the hydrophobic gold layer obtained by dodecanethiol functionalization. SEM images of the tip outer wall and AFM images of deposited droplets are shown in the center and right, respectively. All images are reported at the same scale (scale bar: 1 μm). (A) Hydrophobic tip with an aperture of 200 nm at the tip apex. (B) Mixed tip with an aperture of 80 nm and the gold coating removed within an area of 800 × 800 nm around the tip apex to make it inert to dodecanethiol treatment. Adapted with permission from ref [11]. Copyright 2006 American Chemical Society.

The Espinosa group described the nano fountain pen lithography (NFP) technique using a glass or quartz capillary that has a tapered tip and an aperture of a few hundred nanometers to deliver liquid from the capillary onto a substrate to be patterned [81]. When liquid fills the capillary, it flows to the end of the tapered tip by capillary forces. The liquid flows out from the capillary only when it contacts the substrate due to the surface tension of the droplet formed at the end of the capillary. Espinosa and coworkers demonstrated a sub-100 nm patterning capability in the fountain-pen mode that was realized by implementing a volcano-like tip that has an annular

aperture to control the position of the liquid-air interface at the aperture (Figure 2.16) [81]. The microfluidic AFM probe, named as "Nanofountain Probe" (NFP), consists of a "volcano tip", integrated microchannels, and an on-chip reservoir. When an ink solution is fed into the reservoir, it is driven by capillary action through the microchannel to the volcano tip to form a liquid-air interface around the volcano core. The chip was designed and microfabricated to be mounted on commercial AFMs to use the scanner and optical deflection detection scheme of AFM instruments.
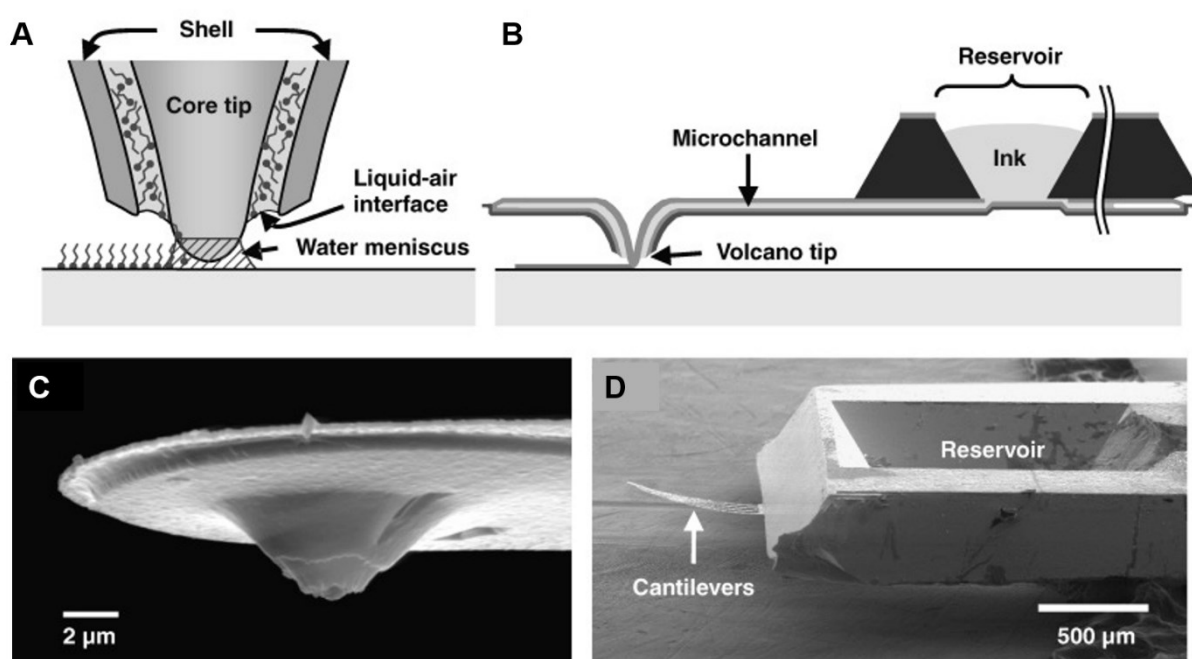
Figure 2.16. Nano fountain pen lithography. (A) Writing mechanism of the NFP device. (B) Ink from the reservoir is delivered to the dispensing tip *via* capillary force. (C, D) SEM images of a volcano dispensing tip (C) and an on-chip reservoir (D). Reproduced with permission from ref [81]. Copyright 2005 WILEY-VCH Verlag GmbH & Co. KGaA, Weinheim.

Hence, either parallel stamping methods such as PPL are available that do not allow continuous ink supply and that require tedious re-inking procedures, or methods based on micropipetting that are, while involving continuous ink supply, slow serial methods. Therefore, a technique that combines parallel stamping of large areas with continuous ink supply is demanding but has not yet been established. This is also the main goal/motivation of this thesis.

2.4. Spongy BCP structures by selective swelling-induced pore formation of BCPs

Russell and coworkers reported swelling-induced morphology reconstruction in the case of thin films of asymmetric block copolymers (BCPs) [17]. The preferential interaction ofthe BCP minority component with a selective solvent reconstructs the BCP film that, after drying, contains arrays of nanopores formed at the locations of the BCP's minority domains. The area density of the nanopores is the same than the area density of the minority domains in the original copolymer thin film. The process is fully reversible. Upon heating the copolymer film above the glass transition temperatures of its components, the original morphology of the BCP film is recovered.

Wang et al. pioneered generation of nanoporous BCP nanorods [19,21,22] obtained *via* anodic aluminum oxide (AAO) molds nanoporous and BCP monoliths [23] by non-destructive swelling-induced pore generation. BCP minority domains treated with selective solvents selectively swell because osmotic pressure drives the selective solvent into the minority domains. The glassy matrix consisting of the BCP majority component undergoes structural reconstruction to accommodate the increased volume of the swollen minority domains. When swelling is quenched by evaporation of the selective solvent, the extended chains of the minority component undergo entropic relaxation, and pores form in place of the swollen minority domains. Depending on the swelling conditions, continuous pore networks open to the environment having adjustable pore diameters result. In 100 µm thick polystyrene-*block*-poly(vinyl pyridine) (PS-*b*-P2VP) substrates bearing PS-*b*-P2VP nanorods (length 1.5 µm, diameter 300 nm) swelling-induced morphology reconstruction in ethanol at 60 °C generated continuous pore systems with P2VP pore walls penetrating the entire specimens (Figure 2.17A), as revealed by porosimetry [23,24]. The pores were permeable for mineral oil, ethanol and water; contact with ethanol at room temperature led to no structure change.
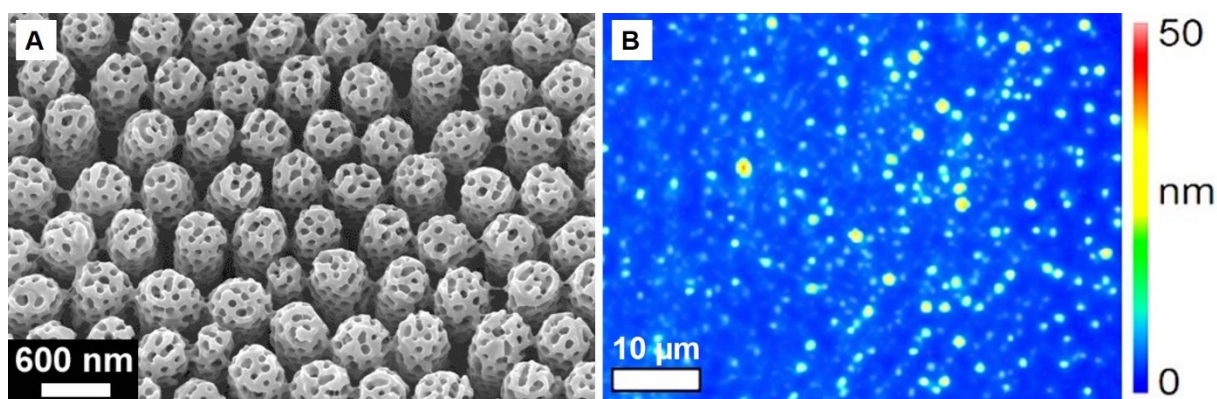
Figure 2.17. (A) Arrays of porous PS-*b*-P2VP nanorods obtained by moulding with AAO and swelling-induced pore generation. (B) A PS-*b*-P2VP nanorod array was infiltrated with mineral oil and placed on a glass slide in such a way that the nanorod tips contacted the glass slide. After detachment of the nanorod array, the glass slide was investigated by white light interferometry to visualize the mineral oil transferred on contact. Adapted with permission from ref [18]. Copyright 2015 Springer Nature.

Imbibition of porous 100 µm thick PS-*b*-P2VP monoliths generated by swelling-induced morphology re-construction with mineral oil revealed Lucas-Washburn-like imbibition kinetics (movement of imbibition front could be monitored by transparency changes) [18]. To test ink supply from the reverse side to the nanorod tips, reverse sides of porous 100 µm thick PS-*b*-P2VP substrates bearing PS-*b*-P2VP nanorods were placed on tissue. The tissue was infiltrated with mineral oil. Manually placing the tips of the porous PS-*b*-P2VP nanorods on a glass slide resulted in deposition of mineral oil nanodroplets on the glass slide (Figure 2.17B).

3. Immobilization of water droplets on hydrophobic surfaces by contact line pinning at non-lithographically generated polymer microfiber rings

3.1. Introduction

This Chapter describes the discovery in the course of the stamp design that after replication molding of PS-*b*-P2VP against surface-modified macroporous silicon molds, swelling-induced pore formation and detachment of the nanoporous PS-*b*-P2VP stamps PS-*b*-P2VP fiber rings remain on the macroporous silicon molds. These PS-*b*-P2VP fiber rings allow immobilization of water drops on the hydrophobically modified surface of the macroporous silicon molds. Water drops immobilized by these rings are prevented from dewetting within the PS-*b*-P2VP fiber rings.

As a result, a nonlithographic approach for the creation of polymeric barriers that efficiently immobilize water drops on hydrophobic perfluorinated surfaces is presented here. A solution of asymmetric PS-*b*-P2VP with P2VP as the minority component was dropped onto hydrophobically modified macroporous silicon (mSi) [82,83]. The obtained circular PS-*b*-P2VP films were subjected to selective-swelling induced pore formation [84,85]. Subsequent mechanical detachment of the circular PS-*b*-P2VP films yielded rings of ruptured PS-*b*-P2VP fibers located in the mSi macropores within annular areas having diameters of a few mm and a width of ~0.2 mm. While water drops deposited onto hydrophobically modified mSi without PS-*b*-P2VP fiber rings rolled off, the PS-*b*-P2VP fiber rings immobilized water drops having volumes up to 50 µL even when the hydrophobically modified mSi was turned into a vertical orientation.

3.2. Experimental section

3.2.1. Materials

Macroporous silicon was provided by SmartMembranes (Halle, Saale); asymmetric PS-*b*-P2VP (M_n(PS) = 101 000 g mol^{-1}; M_n(P2VP) = 29 000 g mol^{-1}; M_w/M_n(PS-*b*-P2VP) = 1.60, volume fraction of P2VP 21%; bulk period 51 nm) was obtained from Polymer Source Inc., Canada. 1*H*,1*H*,2*H*,2*H*-perfluorodecyltrichlorosilane (PFDTS) (97%, stabilized with copper) was supplied by ABCR GmbH. Tetrahydrofuran (THF), ethanol, 98% H_2SO_4, 30% H_2O_2, and deionized water were supplied by local manufacturers in the analytical grade.

3.2.2. Generation of PS-*b*-P2VP fiber rings

To hydrophobically modify mSi with PFDTS [86,87], mSi was treated with a boiling mixture containing 98% H_2SO_4 and 30% H_2O_2 at a volume ratio of 7:3 for 30 min, followed by rinsing with deionized water and drying in an argon flow. Then, the mSi was heated for 5 h at 100 °C in the presence of 0.2 mL PFDTS under room pressure. Defined volumes of a solution containing 0.1 g PS-*b*-P2VP per mL THF were dropped onto the hydrophobically modified mSi using an Eppendorf pipette. The THF was allowed to evaporate for 90 h under ambient conditions. Then, the samples were immersed into ethanol heated to 60 °C for 1 h, followed by drying in an argon flow. The circular PS-*b*-P2VP films were detached with tweezers.

3.2.3. Characterization

SEM investigations were carried out on a Zeiss Auriga microscope operated at an accelerating voltage of 5 kV. Prior to SEM investigations, the samples were coated with a ~5 nm thick iridium layer. Water contact angles were measured in the sessile drop mode at a humidity of 48.40% and a temperature of 23.09 °C using a drop shape analyzer DSA100 (Krüss, Germany).

All contact angle measurements for a specific sample type were repeated on six different samples.

3.3. Results and discussion

3.3.1. Preparation of PS-*b*-P2VP fiber rings

The mSi contained macropores with a depth of ~1.8 µm arranged in hexagonal arrays with a lattice constant of 1.5 µm (Figure 3.1) and was prepared by a combination of photolithography and photoelectrochemical etching [82,83]. Below their inverse-pyramidal pore mouths the mSi macropores had necks with a diameter of ~530 nm. Below the necks the mSi macropores widened to ~710 nm (Figure 3.1B). PFDTS was grafted onto the native oxide layer covering the mSi following procedures reported elsewhere (Figure 3.2) [86,87]. In this way, hydrophobically modified mSi covered by perfluorinated alkyl moieties that exhibited a water contact angle of 127° ± 4° was obtained (average of 6 measurements on different samples; the volume of the deposited water drops was 20 µL). Dropping a solution containing 0.1 g PS-*b*-P2VP (Figure 3.3) per mL THF onto the hydrophobically modified mSi (Figure 3.4A) resulted in the formation of transparent, circular PS-*b*-P2VP films. The mSi macropores were filled with PS-*b*-P2VP rods that formed monolithic units with the transparent circular PS-*b*-P2VP films on the hydrophobically modified mSi (Figure 3.4B,C). In the next step selective-swelling induced pore formation was carried out by treatment with ethanol heated to 60 °C for 1 h (section 2.4).
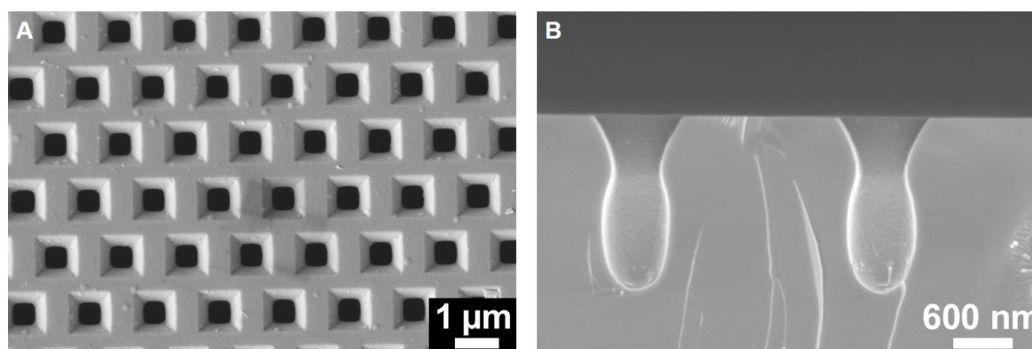
Figure 3.1. SEM images of macroporous Si (mSi). (A) Top view. (B) cross-sectional view.
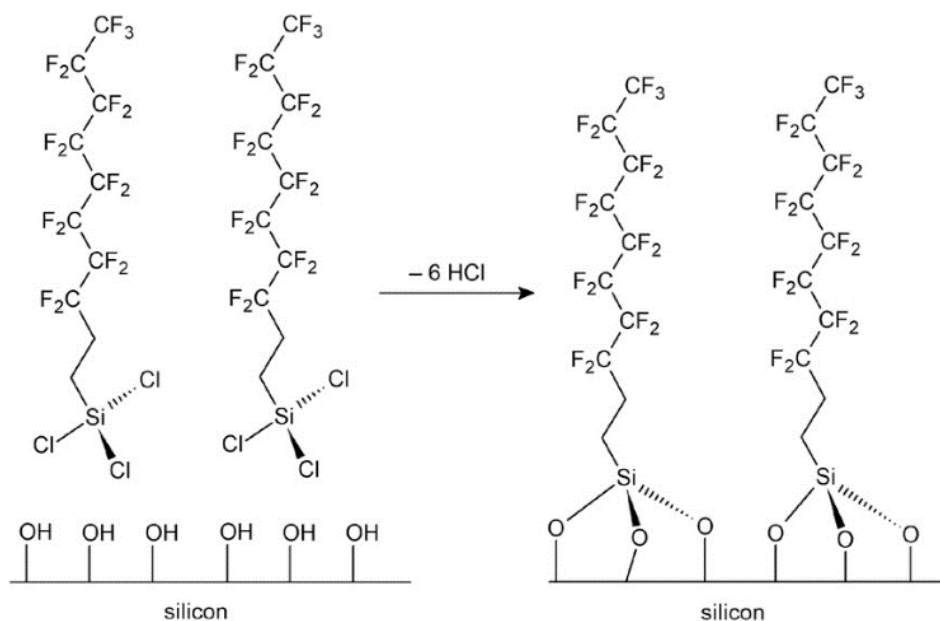
Figure 3.2. Idealized reaction scheme of the grafting of PFDTS onto the native silicon oxide layer covering the mSi macropore walls.
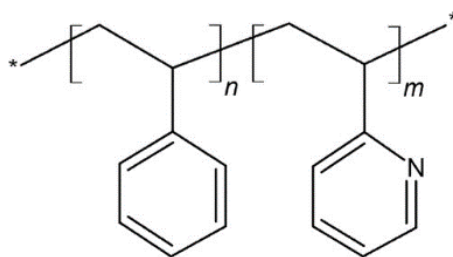
Figure 3.3. Skeletal formula of PS-*b*-P2VP.

The overall volume of the circular PS-*b*-P2VP films increased in the course of swelling-induced pore formation. However, the PS-*b*-P2VP nanorods located in the mSi macropores impeded lateral expansion of the circular PS-*b*-P2VP films, as obvious from the comparison of panels C and E of Figure 3.4. Therefore, volume expansion nearly exclusively occurred in the direction normal to the mSi surface, as determined from SEM images taken at 10 different locations for each sample. The thickness of a circular PS-*b*-P2VP film with a diameter of ∼4.4 mm obtained by deposition of 20 µL PS-*b*-P2VP solution onto hydrophobically modified mSi increased from 111 ± 1 µm prior to selective-swelling induced pore formation to 151 ± 1 µm after selective-swelling induced pore formation. The thickness of a circular PS-*b*-P2VP film with a diameter of ∼6.9 mm obtained by deposition of 60 µL PS-*b*-P2VP solution onto hydrophobically

31
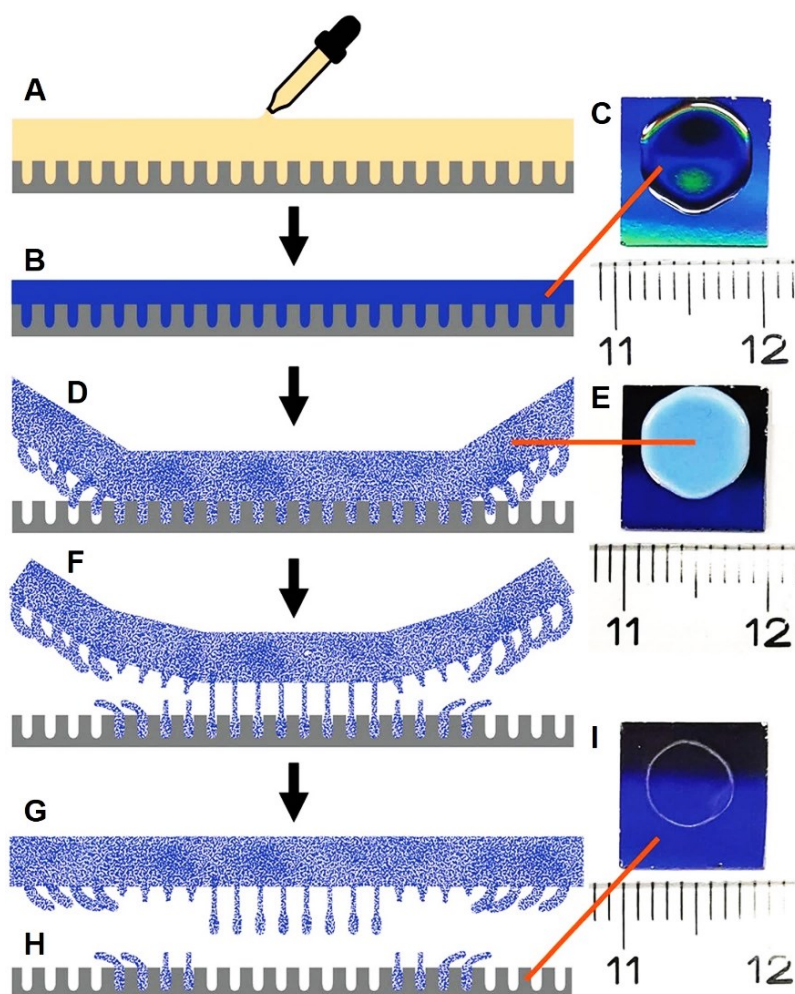
Figure 3.4. Nonlithographic generation of PS-*b*-P2VP fiber rings on hydrophobically modified mSi (gray). (A) PS-*b*-P2VP/THF solution (ocher) is dropped onto hydrophobically modified mSi so that (B,C) a transparent circular film of solid PS-*b*-P2VP (blue) connected to PS-*b*-P2VP fibers located in the mSi macropores forms. (D,E) The circular PS-*b*-P2VP film subjected to selective-swelling induced pore formation gets opaque and mesoporous. Volume expansion pushes the PS-*b*-P2VP fibers at the outermost rim out of the mSi macropores. (F) The PS-*b*-P2VP fibers in an annular region next to the outermost rim are wedged in the mSi macropores because of the volume expansion associated with selective-swelling induced pore formation. Detachment of the circular PS-*b*-P2VP film results in rupture of these PS-*b*-P2VP fibers, which remain located in the mSi macropores. In the center of the circular PS-*b*-P2VP film the PS-*b*-P2VP fibers are only weakly swollen so that they are completely pulled out of the mSi macropores. (G) Detached circular PS-*b*-P2VP film. (H,I) After detachment of the circular PS-*b*-P2VP film a ring of ruptured PS-*b*-P2VP fibers located in the mSi macropores remains on the hydrophobically modified mSi.

modified mSi increased from 110 ± 0 µm prior to selective-swelling induced pore formation

(the standard deviation was rounded to avoid reporting insignificant figures; the rounded

standard deviation amounts to 0 µm) to 147 ± 1 µm after selective-swelling induced pore formation. Moreover, selective-swelling induced pore formation altered the appearance of the circular PS-*b*-P2VP films from transparent (Figure 3.4C) to opaque (Figure 3.4E).

The PS-*b*-P2VP fiber rings remaining on the hydrophobically modified mSi have smaller outer contour diameters than the circular PS-*b*-P2VP films they originate from. Dropping 20 µL PS-*b*-P2VP solution onto hydrophobically modified mSi followed by selective-swelling induced pore formation and detachment of the circular PS-*b*-P2VP films with a diameter of ~4.4 mm yielded PS-*b*-P2VP fiber rings with an outer contour diameter of ~4.1 mm. Dropping 60 µL PS-*b*-P2VP solution onto hydrophobically modified mSi followed by selective-swelling induced pore formation and detachment of the circular PS-*b*-P2VP films with a diameter of ~6.9 mm yielded PS-*b*-P2VP fiber rings with an outer contour diameter of ~6.5 mm. The outer contour diameter of the PS-*b*-P2VP fiber rings can be controlled by the amount of PS-*b*-P2VP solution deposited onto the hydrophobically modified mSi only within certain limitations. While deposition of 5 µL or 10 µL PS-*b*-P2VP solution onto hydrophobically modified mSi yielded circular PS-*b*-P2VP films with diameters of ~2.7 mm and ~3.6 mm, no PS-*b*-P2VP fiber rings remained on the hydrophobically modified mSi after selective-swelling induced pore formation and removal of the circular PS-*b*-P2VP films. Below a certain diameter threshold of the circular PS-*b*-P2VP films annular regions, in which the interplay of swelling and detachment results in the formation of PS-*b*-P2VP fiber rings, do, therefore, no longer form.

Instead, the PS-*b*-P2VP fibers are completely pulled out of the macropores of the mSi. Since the hydrophobically modified mSi pieces used in this work had edge lengths of 1 cm, 60 µL was the largest solution volume that could be deposited. Larger PS-*b*-P2VP fiber rings should, in principle, be accessible. It was assumed that a soft upper limit to the outer contour diameter of the PS-*b*-P2VP fiber rings might be related to the deposition of the PS-*b*-P2VP solution onto the hydrophobically modified mSi. As the drop volume increases, effects such as contact line instabilities, contact line pinning, or Marangoni convection may become more relevant so that

PS-*b*-P2VP films formed on the hydrophobically modified mSi exhibit no longer approximately circular shapes.

3.3.2. PS-*b*-P2VP fiber rings: mechanism of formation

Selective-swelling induced pore formation is crucial for the formation of the PS-*b*-P2VP fiber rings. Figure 3.5A shows a SEM large-field view of a PS-*b*-P2VP fiber ring obtained by dropping 20 µL PS-*b*-P2VP solution onto hydrophobically modified mSi (corresponding to Figure 3.4H,I). Figure 3.5B,C shows details of the outermost rim of the PS-*b*-P2VP fiber ring seen in Figure 3.5A captured at the top (Figure 3.5B) and at the opposite position on the bottom (Figure 3.5C), as marked in Figure 3.5A. Larger-field SEM views were taken on the left (Figure 3.6B), on the right (Figure 3.6C), at the top (Figure 3.6D) and on the bottom (Figure 3.6E) of the outermost rim of the PS-*b*-P2VP fiber ring, as indicated in Figure 3.6A. Within the outermost rim with a width of 10–15 µm the PS-*b*-P2VP fibers protruding from the mSi macropores are bent radially outward. However, away from the outermost rim the PS-*b*-P2VP fibers protruding from the mSi macropores do no longer show anisotropic orientation (Figure 3.5D,E; Figure 3.6F).

Further light on the formation of the PS-*b*-P2VP fiber rings is shed by the investigation of the circular PS-*b*-P2VP films after their detachment from hydrophobically modified mSi (Figure 3.4G). Figure 3.7 shows a detached circular PS-*b*-P2VP film that is the counterpart to the PS-*b*-P2VP fiber ring displayed in Figure 3.5A. Figures 3.8 and 3.9 comprise series of SEM images taken at the positions indicated in Figure 3.7 along a radial line from the top to the bottom of the shown detached circular PS-*b*-P2VP film. The outermost rim of the circular PS-*b*-P2VP film (position U1, Figures 3.8A and 3.9A; position D1, Figures 3.8B and 3.9B; position U2, Figures 3.8C and 3.9C; and position D2, Figures 3.8D and 3.9D) is directly exposed to the swelling agent ethanol. Therefore, selective-swelling induced pore formation starts here and volume expansion pushes the PS-*b*-P2VP fibers out of the mSi macropores. Hence, the outermost rims

of the circular PS-*b*-P2VP films detach from hydrophobically modified mSi in such a way that intact PS-*b*-P2VP fibers remain attached to the circular PS-*b*-P2VP films.

As selective-swelling induced pore formation proceeds into the circular PS-*b*-P2VP films, at positions U3 (Figures 3.8E and 3.9E) and D3 (Figures 3.8F and 3.9F) local shear forces pointing radially outward caused by volume expansion deform the PS-*b*-P2VP fibers. Even though the PS-*b*-P2VP fibers are slightly stretched, they are still completely pushed out of the mSi macropores and remain attached to the circular PS-*b*-P2VP film. Notably, the PS-*b*-P2VP fibers are bent radially inward.

At positions U4 (Figures 3.8G and 3.9G) and D4 (Figures 3.8H and 3.9H) on the circular PS-*b*-P2VP film a transition from the annular area in which the PS-*b*-P2VP fibers were bent inward to an annular area closer to the center in which the PS-*b*-P2VP fibers were ruptured occurs. Positions U5 (Figures 3.8I and 3.9I) and D5 (Figures 3.8J and 3.9J) on the circular PS-*b*-P2VP film are located right inside the annular area in which the PS-*b*-P2VP fibers ruptured, which is obviously the counterpart to the PS-*b*-P2VP fiber ring remaining on the hydrophobically modified mSi (Figures 3.4H,I and 3.5A). Only the outermost PS-*b*-P2VP fibers of the PS-*b*-P2VP fiber ring protruding from the mSi macropores are bent radially outward and can be considered as counterparts of the PS-*b*-P2VP fibers bent inward on the detached circular PS-*b*-P2VP film. The largest portion of the PS-*b*-P2VP fiber ring consists of unoriented PS-*b*-P2VP fibers (Figure 3.5D,E and Figure 3.6F). Therefore, radial shear can be ruled out as main origin of the rupture of the PS-*b*-P2VP fibers. Instead, it was assumed that volume expansion related to selective-swelling induced pore formation becomes effective before the PS-*b*-P2VP fibers are pushed out of the mSi macropores. When the circular PS-*b*-P2VP film is detached from the hydrophobically modified mSi, the PS-*b*-P2VP fibers within the annular areas of the PS-*b*-P2VP fiber rings are wedged in the mSi macropores and rupture. Likely, the neck close to the mouths of the mSi macropores supports the rupturing of the PS-*b*-P2VP fibers.
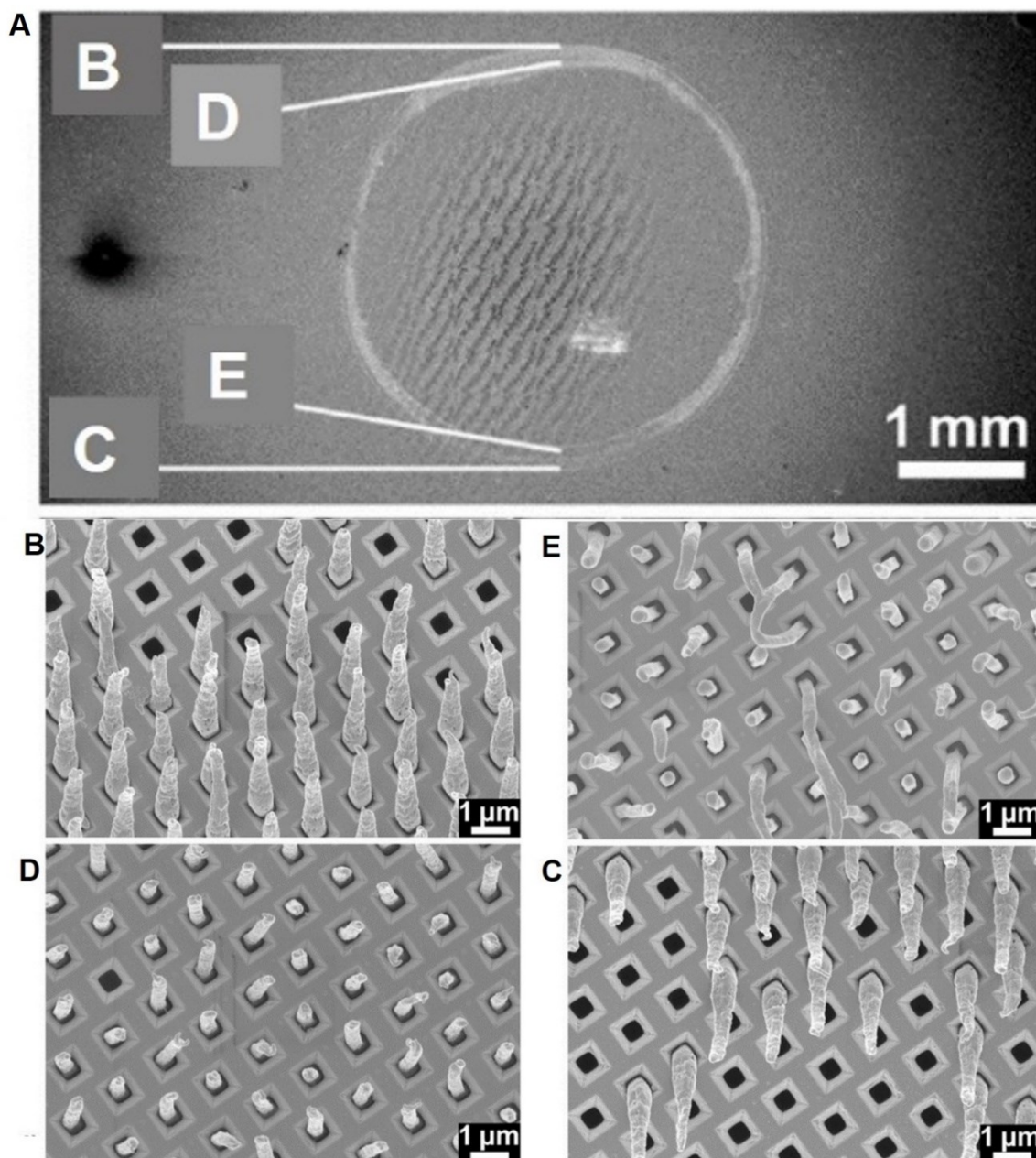
Figure 3.5. SEM images of a PS-*b*-P2VP fiber ring obtained by dropping 20 µL PS-*b*-P2VP solution onto hydrophobically modified mSi. (A) Large-field view; the approximate positions at which panels (B)–(E) were taken are indicated. Outermost rim at the top (B) and on the bottom (C) of the PS-*b*-P2VP fiber ring shown in panel (A). (D,E) Center of the PS-*b*-P2VP fiber ring shown in panel (A) at the top (D) and on the bottom (E).
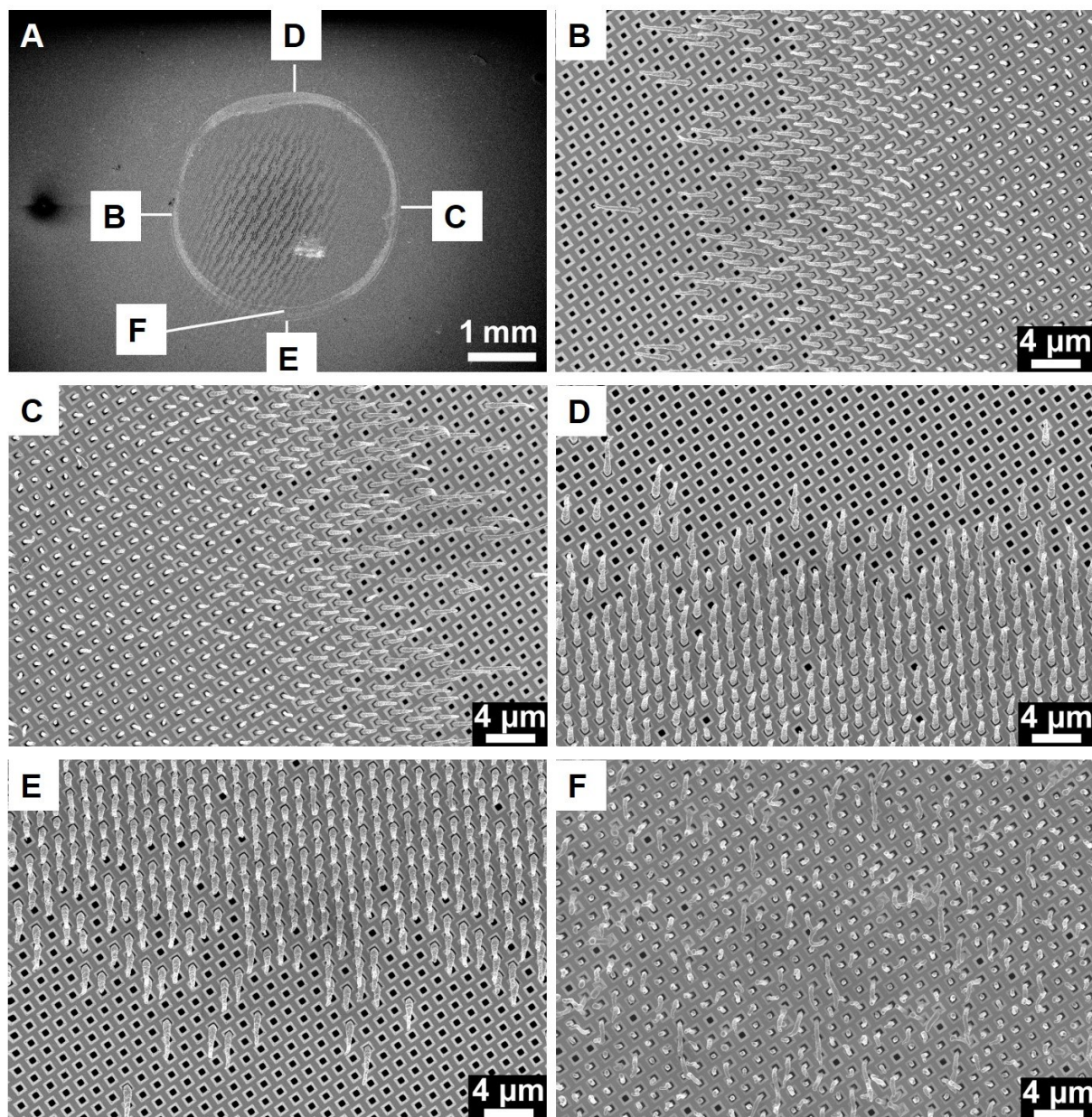
Figure 3.6. SEM images of a PS-*b*-P2VP fiber ring obtained by dropping 20 µL of a solution of 0.1 g/mL PS-*b*-P2VP in THF onto on mSi hydrophobically modified with PFDTS, followed by treatment with hot ethanol and detachment of the circular PS-*b*-P2VP film. (A) Large-field view. The approximate positions at which the micrographs displayed in panels (B) to (F) were taken are indicated. (B)–(E) Micrographs taken at the outermost rim of the PS-*b*-P2VP fiber ring (B) on the left, (C) on the right, (D) at the top and (E) on the bottom. (F) Micrograph taken on the bottom of panel a) in the center of the PS-*b*-P2VP fiber ring.

Further toward the center of the detached circular PS-*b*-P2VP film, at positions U6 (Figures 3.8K and 3.9K) and D6 (Figures 3.8L and 3.9L) the PS-*b*-P2VP fibers are completely extracted from the mSi macropores and remain, albeit somewhat stretched, attached to the detached

circular PS-*b*-P2VP film. As long as the circular PS-*b*-P2VP film is still located on the hydrophobically modified mSi the PS-*b*-P2VP fibers in the center can hardly be reached by the ethanol molecules within the exposure time. Thus, selective-swelling-induced pore formation is impeded, no significant volume expansion occurs, and the PS-*b*-P2VP fibers can be pulled out of the mSi macropores.

Figure 3.7. Large-field SEM image of a circular PS-*b*-P2VP film obtained by dropping 20 µL of a solution of 0.1 g/mL PS-*b*-P2VP in THF onto mSi hydrophobically modified with PFDTS, followed by treatment with hot ethanol and detachment from the mSi. The approximate positions at which the SEM images shown in Figures 3.8 and Figure 3.9 were taken are indicated.
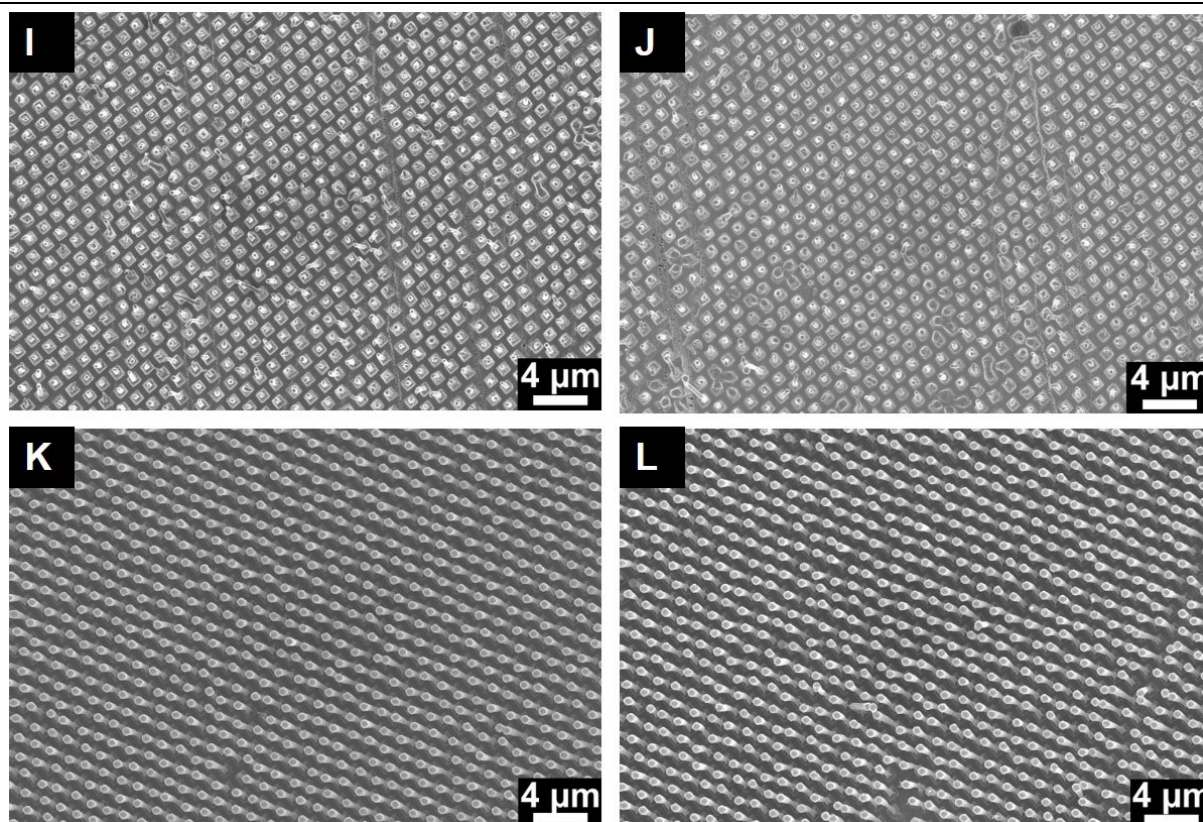
Figure 3.8. Large-field SEM images of a circular PS-*b*-P2VP film obtained by dropping 20 µL of a solution of 0.1 g/mL PS-*b*-P2VP in THF onto mSi hydrophobically modified with PFDTS, followed by treatment with hot ethanol and detachment from the mSi. The micrographs were approximately taken at the positions indicated in Figure 3.7. Panels A (position U1), C (position U2), E (position U3), G (position U4), I (position U5) and K (position U6) were taken in the upper half of the circular PS-*b*-P2VP film along a downward trajectory from the outermost rim towards the center. Panels B (position D1), D (position D2), F (position D3), H (position D4), J (position D5) and L (position D6) were taken in the lower half of the circular PS-*b*-P2VP film along an upward trajectory from the outermost rim towards the center.

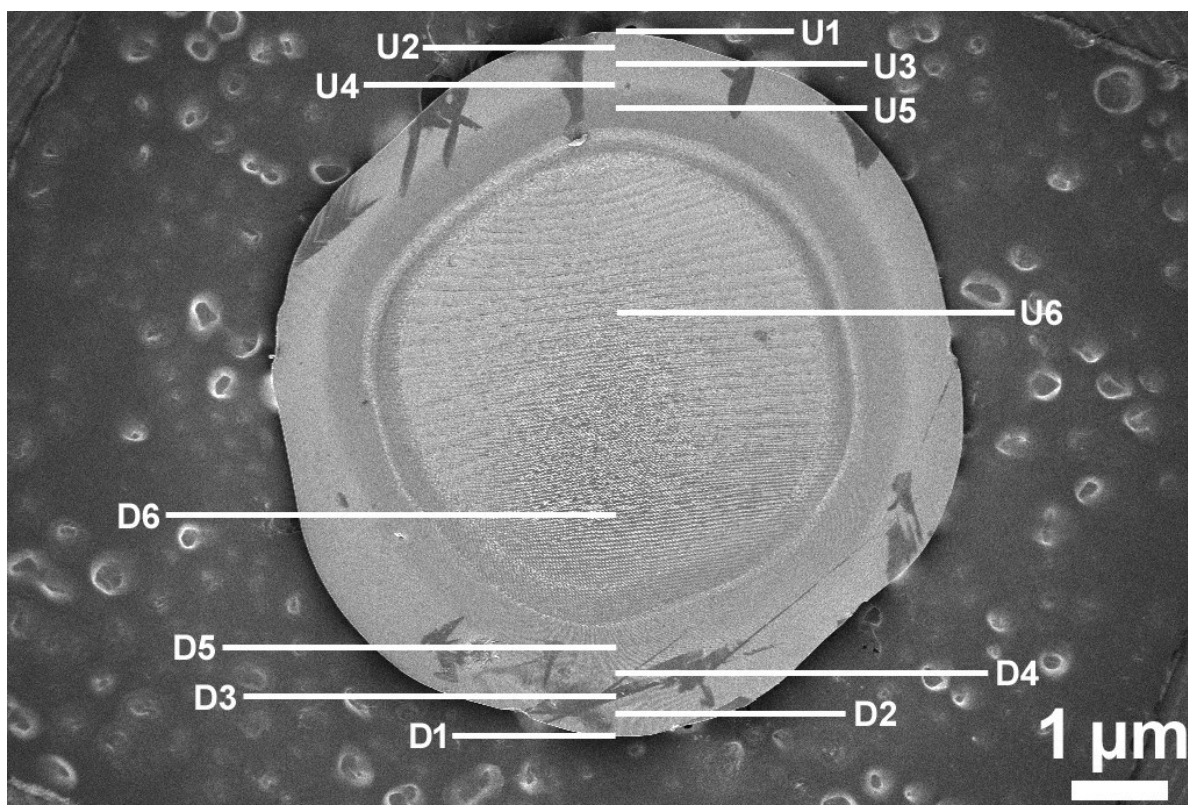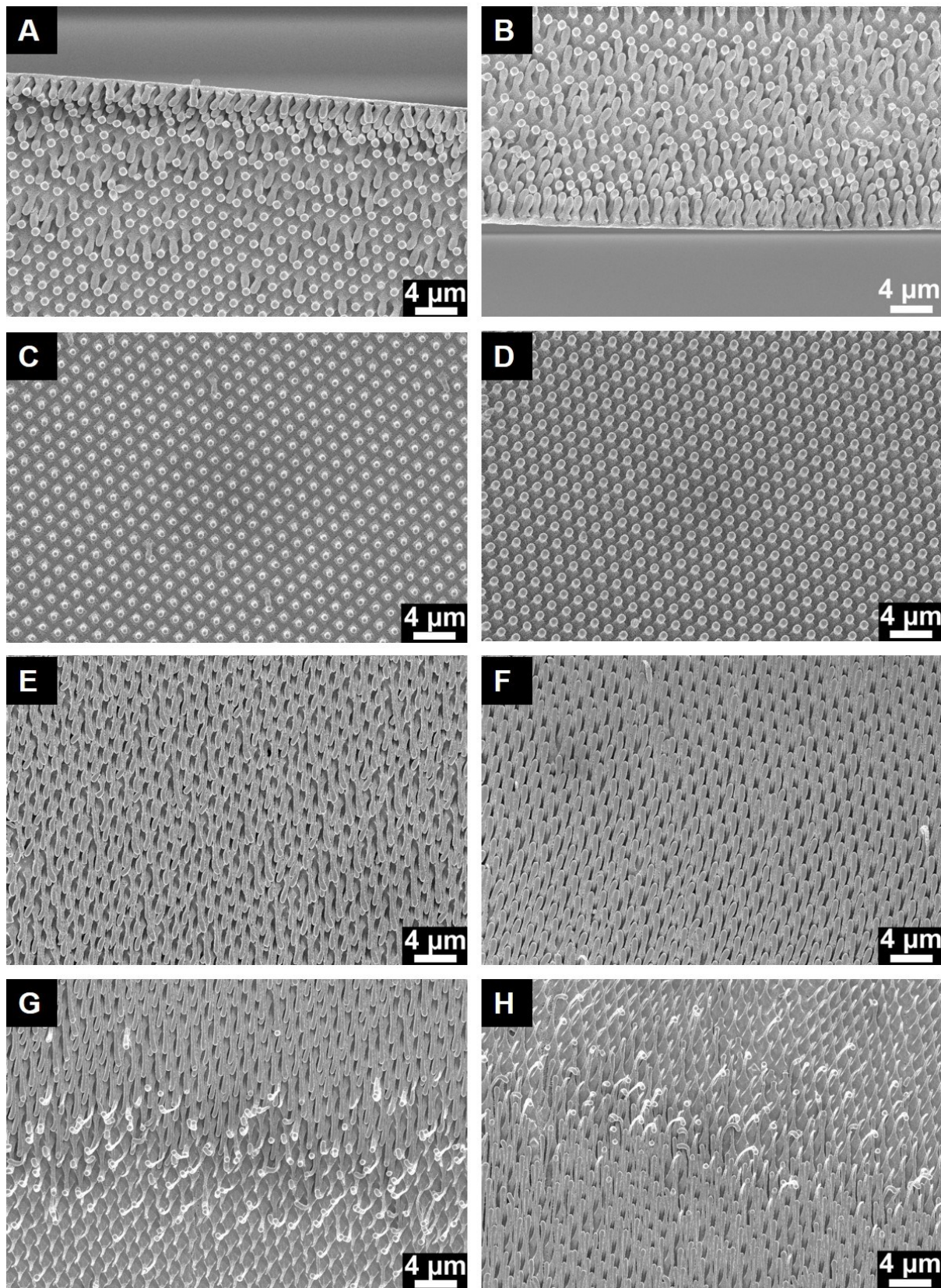**Figure 3.9.** SEM images showing details of a circular PS-*b*-P2VP film obtained by dropping 20 µL of a solution of 0.1 g/mL PS-*b*-P2VP in THF onto mSi hydrophobically modified with PFDTS, followed by treatment with hot ethanol and detachment from the mSi. The micrographs were approximately taken at the positions indicated in Figure 3.7. Panels A (position U1), C (position U2), E (position U3), G (position U4), I (position U5) and K (position U6) were taken in the upper half of the circular PS-*b*-P2VP film along a downward trajectory from the outermost rim towards the center. Panels B (position D1), D (position D2), F (position D3), H (position D4), J (position D5) and L (position D6) were taken in the lower half of the circular PS-*b*-P2VP film along an upward trajectory from the outermost rim towards the center.

3.3.3. Pinning of water drops on hydrophobically modified mSi by PS-*b*-P2VP fiber rings

Figure 3.10A shows six hydrophobically modified mSi pieces with PS-*b*-P2VP fiber rings having outer contour diameters of ~4.1 mm and widths of ~0.2 mm. Water drops with a volume of 20 µL completely covered the areas encompassed by the PS-*b*-P2VP fiber rings with outer contour diameters of ~4.1 mm and were confined by the latter (Figure 3.10B). The water drops were even immobilized when the 6 hydrophobically modified mSi pieces were tilted into perpendicular orientation-despite inertia (when the samples are moved by hand) and gravitation. The photographs shown in Figure 3.10D–G highlight the different behavior of water drops with a volume of 20 µL on hydrophobically modified mSi without (on the left) and with (on the right) a PS-*b*-P2VP fiber ring. As soon as the hydrophobically modified mSi piece without PS-*b*-P2VP fiber ring was tilted, the water drop rolled off; eventually, the water was arrested at the edge of the glass cover slip onto which the hydrophobically modified mSi was glued. However, the water drop deposited into the PS-*b*-P2VP fiber ring on the hydrophobically modified mSi piece

seen on the right was arrested even when the hydrophobically modified mSi piece was vertically oriented and despite the trembling movements inevitable when the sample is held manually. Six hydrophobically modified mSi pieces with larger PS-*b*-P2VP fiber rings having outer contour diameters of ~6.5 mm and widths of 0.2–0.3 mm are seen in Figure 3.11A. Water drops with a volume of 50 µL completely covered the areas of PS-*b*-P2VP fiber rings with an outer contour diameter of ~6.5 mm (Figure 3.11B) and remained arrested during tilting into perpendicular orientation (Figure 3.11C). A drop with a volume of 50 µL on hydrophobically modified mSi without a PS-*b*-P2VP fiber ring (on the left in Figure 3.11D–G) rolled off as soon as the hydrophobically modified mSi piece was tilted. The water drop deposited into the PS-*b*-P2VP fiber ring on the hydrophobically modified mSi piece seen on the right in Figure 3.11D–G was arrested even when the hydrophobically modified mSi piece was vertically oriented.
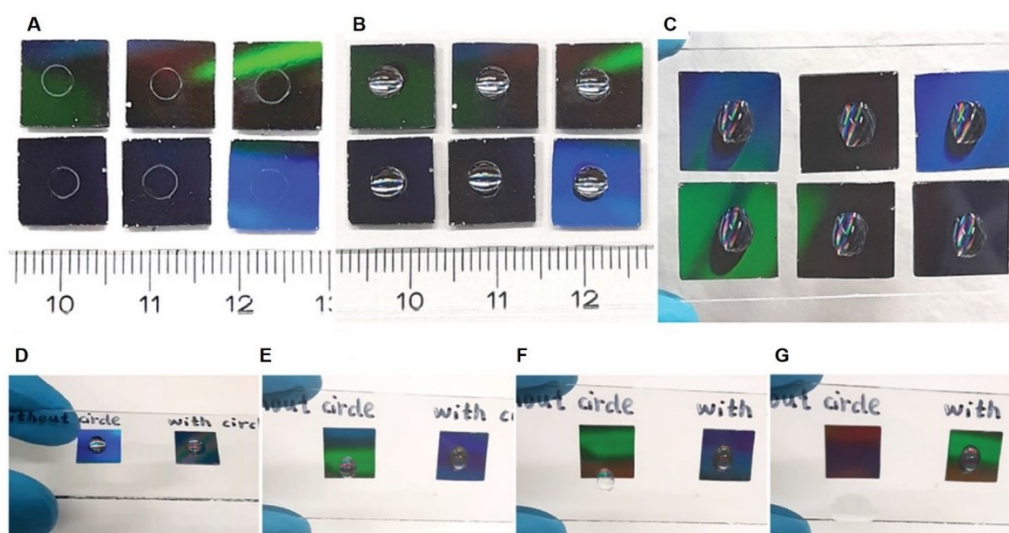
Figure 3.10. Immobilization of water drops on hydrophobically modified mSi by PS-*b*-P2VP fiber rings with an outer contour diameter of ~4.1 mm. (A) As-prepared PS-*b*-P2VP fiber rings. (B) Water drops with a volume of 20 µL deposited into the PS-*b*-P2VP fiber rings while the mSi substrate is kept in horizontal orientation. (C) Water drops with a volume of 20 µL deposited into the PS-*b*-P2VP fiber rings while the mSi substrates are kept in vertical orientation. (D–G) Comparison of the behavior of water drops with a volume of 20 µL on hydrophobically modified mSi without (left) and with (right) PS-*b*-P2VP fiber ring. When the hydrophobically modified mSi is tilted from horizontal to vertical orientation, the water drop deposited onto the mSi without PS-*b*-P2VP fiber ring rolls off. The water drop deposited onto the hydrophobically modified mSi with PS-*b*-P2VP fiber ring is held by the PS-*b*-P2VP fiber ring even if the hydrophobically modified mSi is brought into vertical orientation.

Figure 3.11. Immobilization of water drops on hydrophobically modified mSi by PS-*b*-P2VP fiber rings with an outer contour diameter of ~6.5 mm. (A) As-prepared PS-*b*-P2VP fiber rings. (B) Water drops with a volume of 50 µL deposited into the PS-*b*-P2VP fiber rings while the mSi substrate is kept in horizontal orientation. (C) Water drops with a volume of 50 µL deposited into the PS-*b*-P2VP fiber rings while the mSi substrates are kept in vertical orientation. (D–G) Comparison of the behavior of water drops with a volume of 50 µL on hydrophobically modified mSi without (left) and with (right) PS-*b*-P2VP fiber ring. When the hydrophobically modified mSi is tilted from horizontal to vertical orientation, the water drop deposited onto the mSi without PS-*b*-P2VP fiber ring rolls off. The water drop deposited onto the hydrophobically modified mSi with PS-*b*-P2VP fiber ring is held by the PS-*b*-P2VP fiber ring even if the hydrophobically modified mSi is brought into vertical orientation.

Wetting phenomena on topographically patterned substrates are complex [88,89], and it has been argued that wetting is controlled by interactions in the vicinity of the contact line, which is the intersection of the liquid phase, the gas phase and the solid substrate [90]. Water drops with volumes of 5 µL deposited into PS-*b*-P2VP fiber rings with diameters of ~4.1 mm did neither completely cover the surface area of the hydrophobically modified mSi encircled by the PS-*b*-P2VP fiber rings nor did they contact the latter. The contact angles of the water drops with a volume of 5 µL deposited into the PS-*b*-P2VP fiber rings amounted to 108° ± 1°. The contact lines of water drops with volumes ⩾10 µL and ⩽35 µL coincided with the PS-*b*-P2VP fiber rings. The apparent contact angles increased with increasing drop volume from ~73° ± 7° to

44
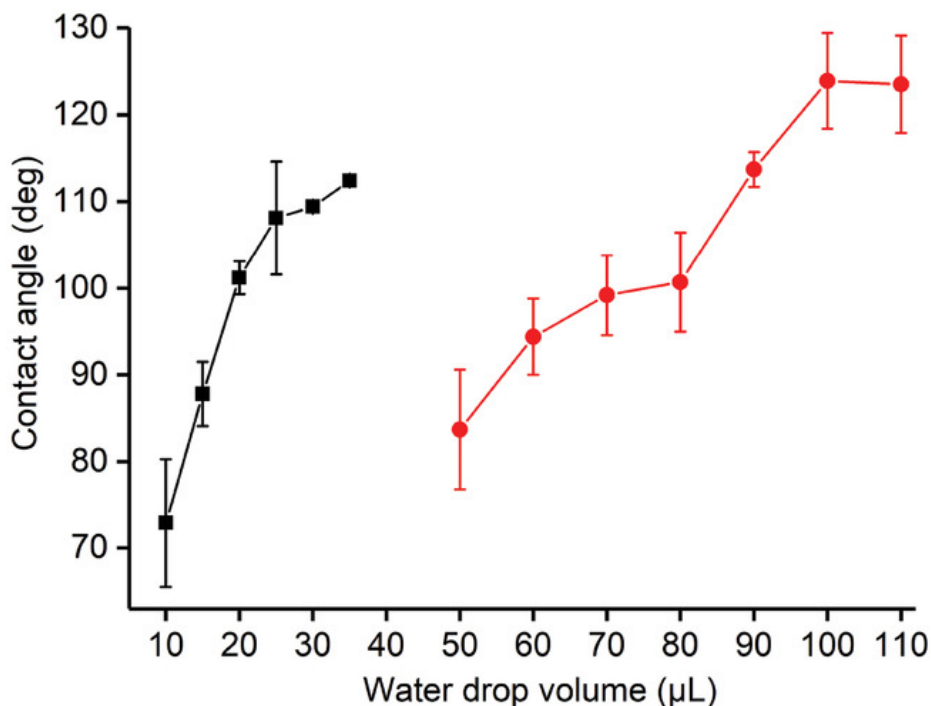
Figure 3.12. Apparent contact angles of water drops deposited into PS-*b*-P2VP fiber rings on hydrophobically modified mSi as function of the drop volume. Each data point represents 6 measurements on different samples. Black squares represent data points obtained with PS-*b*-P2VP fiber rings having an outer contour diameter of ~4.1 mm; red circles represent data points obtained with PS-*b*-P2VP fiber rings having an outer contour diameter of ~6.5 mm. The standard deviations are indicated. The lines are guides to the eyes.

~112° ± 0° (Figure 3.12). Water drops with a volume of 40 µL where no longer confined by PS-*b*-P2VP fiber rings with diameters of 4.1 mm. A similar behavior was observed for PS-*b*-P2VPfiber rings with diameters of ~6.5 mm. The contact lines of water drops with volumes ⩾50 µL and ⩽110 µL coincided with the PS-*b*-P2VP fiber rings, while the apparent contact angles increased with increasing drop volume from ~84° ± 7° to ~124° ± 6° (Figure 3.12). Water drops with a volume of 20 µL deposited into PS-*b*-P2VP fiber rings having diameters of ~6.5 mm did not contact the latter and showed contact angles of 123° ± 1°. Hence, water drops within a wide volume range show contact line pinning at the PS-*b*-P2VP fiber rings. The contact line pinning prevents displacements of the water drops out of the PS-*b*-P2VP fiber rings if the hydrophobically modified mSi is moved or tilted but also dewetting within the PS-*b*-P2VP fiber rings. Consequently, water drops may be forced to adopt macroscopic contact angles much smaller than in the absence of the PS-*b*-P2VP fiber rings. The PS-*b*-P2VP fiber rings are both

45

chemical and topographic barriers to contact line displacement. After swelling-induced pore generation the segments of the PS-*b*-P2VP fibers protruding from the mSi pores have an outer surface consisting of P2VP [19]. P2VP is slightly hydrophilic and has a water contact angle of 66° ± 1° [24]. On the other hand, the PS-*b*-P2VP fibers protruding from the mSi macropores likely pierce into the water drops.

3.4. Conclusion

In the course of the stamp design and preparation, PS-*b*-P2VP fiber rings were found. The nonlithographic preparation of PS-*b*-P2VP fiber rings with diameters of a few mm and widths of ~0.2 mm on hydrophobically modified macroporous silicon with perfluorinated surface. The rings of ruptured PS-*b*-P2VP fibers protruding from the hydrophobically modified macroporous silicon arrest water drops with volumes up to several 10 µL by contact line pinning. Thus, displacement of the water drops caused by movements or tilting of the hydrophobically modified macroporous silicon as well as dewetting inside the PS-*b*-P2VP fiber rings are prevented. Water drops deposited onto hydrophobically modified macroporous silicon without PS-*b*-P2VP fiber rings immediately roll off. To prepare the PS-*b*-P2VP fiber rings a PS-*b*-P2VP solution was dropped onto hydrophobically modified mSi. The circular PS-*b*-P2VP films thus obtained were connected with PS-*b*-P2VP fibers located inside the mSi macropores. Subsequent selective-swelling induced pore generation with hot ethanol resulted in expansion of the PS-*b*-P2VP volume. In the outer rims of the circular PS-*b*-P2VP films well accessible to the ethanol molecules swelling-induced pore formation pushed the PS-*b*-P2VP fibers out of the mSi macropores. The centers of the circular PS-*b*-P2VP films with poor accessibility to the ethanol molecules were hardly affected by swelling-induced pore formation; upon detachment of the circular PS-*b*-P2VP films the hardly swollen PS-*b*-P2VP fibers were completely pulled out of the mSi macropores. In the annular regions between the outer rims and the centers of the circular PS-*b*-P2VP films the PS-*b*-P2VP fibers were swollen prior to detachment. Hence, the PS-*b*-P2VP fibers were wedged in the mSi macropores and ruptured upon detachment of the circular

PS-*b*-P2VP films so that PS-*b*-P2VP fiber rings remained on the hydrophobically modified mSi. The immobilization of water drops on hydrophobic surfaces achieved here enables the exploitation of typical advantageous properties of hydrophobic surfaces such as chemical inertness, antifouling behavior and the repulsion of adsorbates in highly flexible lab-on-chip configurations. Water drops immobilized by PS-*b*-P2VP rings on hydrophobically modified mSi may be used as microscale reactors for chemical syntheses or for trapping nonadherent cells. Since mSi can be oxidized to glass prior to hydrophobic modification, integration into advanced optical microscopy set-ups is conceivable. The generation of the PS-*b*-P2VP fiber rings as well as the positioning of water drops into the PS-*b*-P2VP fiber rings can easily be automatized.

4. Nanostructured submicron block copolymer dots by sacrificial stamping

4.1. Introduction

This Chapter reports the result of preliminary stamping experiments with spongy non-inked PS-*b*-P2VP stamps after spongy nanoporous PS-*b*-P2VP stamps are obtained. Parts of the stamps' contact elements can be lithographically transferred onto a counterpart surface.

Chemical and topographic high-throughput patterning of surfaces by lithographic stamping is key to the preparation of a broad range of functional materials and components [91]. Nanoimprint lithography [92,93] involves embossing of plastically deformable surfaces or surface coatings, often consisting of polymeric materials, with hard stamps. Classical soft lithography with elastomeric stamps [1,2] including approaches such as μCP [3,4] and PPL [5-7] involves the transfer of molecules adsorbed on the stamp surface to a counterpart surface, on which consequently thin ink layers are deposited. Lithographic approaches that combine deposition of materials and topographic patterning may involve different types of capillary force lithography [94,95], wet lithography [96], and electrochemical lithography [97]. The stamping of functional materials characterized by complex molecular and/or mesoscopic architectures using classical soft lithography has remained demanding. Preformed nanoparticles having the desired functionality may be assembled on a first substrate, then transferred to a stamp, and finally stamped onto a second substrate [98,99]. In the case of nanoparticles characterized by complex mesoscopic morphologies, such as mesoporous silica nanoparticles, deposition onto surfaces typically requires complex bonding chemistry [100-104]; spatial distribution and ordering of the mesoporous silica nanoparticles are difficult to control.

BCPs are a particularly interesting class of materials because they may combine the specific properties of their chemically distinct blocks. In the case of the PS-*b*-P2VP the nonpolar PS blocks may serve as rigid glassy scaffold. The polar P2VP blocks can be functionalized taking advantage of the presence of the pyridyl group in each P2VP repeat unit. Also, reversible swelling of the P2VP domains can be controlled via the pH value [105]. BCPs themselves have

been employed as structure-directing agents [106]. Also, either solid or mesoporous BCP nanoparticles are accessible by different solution-based preparative approaches [107-109]. Lithographic deposition of BCPs by a parallel lithographic process would be a powerful approach to pattern and to functionalize surfaces but has not yet been established.

The sacrificial stamping procedure emerging from the preliminary stamping experiments with non-inked spongy PS-*b*-P2VP stamps yielded arrays of nanostructured PS-*b*-P2VP submicron dots. A sacrificial PS-*b*-P2VP stamp topographically patterned with contact elements approaches a counterpart surface. The PS-*b*-P2VP stamp is then pressed against the counterpart surface so that tight adhesive contact between contact elements and counterpart surface forms. Upon retraction of the sacrificial PS-*b*-P2VP stamp, the contact elements rupture so that the layer of the contact elements in intimate contact with the counterpart surface remains attached to the latter. As a result, parts of the sacrificial PS-*b*-P2VP stamp are lithographically deposited onto the counterpart surface. The deposited submicron PS-*b*-P2VP dots can be further functionalized.

4.2. Experimental section

4.2.1. Materials

Macroporous silicon (product number 620514-W23) was provided by SmartMembranes GmbH (Halle (Saale), Germany). Self-ordered AAO with a pore diameter of 300 nm, a lattice period of 500 nm, and a pore depth of 1.0 μm was prepared by anodizing aluminum chips with a diameter of 4 cm (Goodfellow, purity >99.99%) following procedures reported elsewhere [110]. The self-ordered AAO layer was connected to a ∼1000 μm thick Al substrate. Asymmetric PS-*b*-P2VP (M_n(PS) = 101 000 g/mol; M_n(P2VP) = 29 000 g/mol; M_w/M_n(PS-*b*-P2VP) = 1.60, volume fraction of P2VP 21%; bulk period ∼51 nm) was obtained from Polymer Source Inc. Tetrachloroauric(III)acid (HAuCl$_4$), trisodium citrate, and rhodamine B were purchased from

Sigma-Aldrich. PFDTS, (97%, stabilized with copper) was supplied by ABCR GmbH. The gold nanoparticles (AuNPs) were synthesized following procedures reported elsewhere [111,112]. A 1 mL portion of an aqueous 3.88×10^{-2} M citrate solution was added to 50 mL of a boiling solution of 0.01 wt% $HAuCl_4$ in water. The aqueous mixture with a pH value of 3.5 was boiled for 20 min under vigorous stirring and then cooled to room temperature. A silicon wafer stamped with submicron PS-*b*-P2VP dots was dipped into the thus-obtained aqueous AuNP suspension for 1 h, followed by three washing steps with deionized water.

4.2.2. Preparation of sacrificial PS-*b*-P2VP stamps

To modify the surface of the mSi with PFDTS, the mSi was first treated with a boiling mixture containing 98% H_2SO_4 and 30% H_2O_2 at a volume ratio of 7:3 for 30 min, followed by rinsing with deionized water and drying in an argon flow. Then, the mSi was coated with PFDTS by vapor deposition for 2 h at 85 °C and for 3 h at 130 °C following procedures reported elsewhere [86]. About 240 μm thick PS-*b*-P2VP films were prepared by dropping a solution of 100 mg of PS-*b*-P2VP per mL of THF onto a silicon wafer. After the complete evaporation of THF, the PS-*b*-P2VP films were detached by exposure to ethanol for 24 h at room temperature and sandwiched between self-ordered AAO and surface-modified mSi in such a way that the macropore openings of the self-ordered AAO and the surface-modified mSi were in contact with the PS-*b*-P2VP. The PS-*b*-P2VP was infiltrated at 220 °C for 4 h under vacuum while a load of 160 mbar was applied. The PS-*b*-P2VP was cooled to room temperature at a rate of −1 K/min and immersed into ethanol for ∼30 min. Swelling-induced pore generation was carried out in ethanol at 60 °C for 4 h. The Al substrate connected to the self-ordered AAO layer was selectively etched with a solution of 100 mL of 37% HCl and 3.4 g of $CuCl_2 \cdot 2H_2O$ in 100 mL of deionized water at 0 °C. Finally, the self-ordered AAO was removed by etching with 3 M $NaOH_{(aq)}$ followed by washing with deionized water. The sacrificial PS-*b*-P2VP stamps were finally subjected to oxygen plasma at 100 W for 4 min using a plasma cleaner Femto (Diener electronic, Ebhausen, Germany).

4.2.3. Sacrificial stamping

Silicon wafers were cut into small pieces with areas of 1 cm × 1 cm. Thus-obtained Si wafer pieces and glass slides used as substrates for sacrificial stamping were washed with acetone, dried in an argon flow, and treated with oxygen plasma (100 W; 10 min) using a plasma cleaner Femto (Diener electronic, Ebhausen, Germany). The sacrificial PS-*b*-P2VP stamp used to produce the sample was immersed into a solution of 50 mmol/L rhodamine B in ethanol for 1 h followed by three washing steps with deionized water and drying at 35 °C for 12 h. Prior to sacrificial stamping, the PS-*b*-P2VP stamps were attached to a home-made stamp holder made of stainless steel (length, 55 mm; diameter, 12 mm; mass, 40 g) using double-sided adhesive tape. Sacrificial stamping was carried out manually while applying a pressure of ~50 bar. The pressure was adjusted by carrying out sacrificial stamping on a balance and calculated from the displayed mass. The contact time amounted to ~1 s.

4.2.4. Characterization

SEM investigations were carried out on a Zeiss Auriga microscope operated at an accelerating voltage of 3 kV. For SEM, the samples were sputter-coated with a 5 nm thick iridium layer. AFM measurements were conducted in semicontact mode using a NT-MDT NTEGRA device. The cantilevers had a nominal length of 95 μm, force constants of 3.1–37.6 N/m, and a resonance frequency of 256 kHz (within the range 140–390 kHz). The tip radius was 10 nm. The AFM images were processed by using the software Nova Px. TIRFM was performed using an inverted microscope (IX71, Olympus) equipped with a motorized 4-line TIRF condenser (cellTIRF 4-Line system, Olympus), a 150-fold oil immersion TIRF objective (UAPON 150× TIRF, NA 1.45 Olympus), and a 561 nm diode-pumped solid-state laser (max power 200 mW; Cobolt Jive 561, Cobolt). Images were acquired by an electron multiplying back-illuminated frame transfer CCD camera (iXon Ultra 897, Andor). A fluorescence filter cube containing a polychroic beamsplitter (R405/488/561/647, Semrock) and a quad-band emission/blocking

filter (FF01 446/523/600/677, Semrock) was used. For each sample, 500 frames were recorded with an exposure time of 31 ms, a cycle time of 67 ms, and a laser power of 5 mW (power density approximately 150 W/cm^2).

4.3. Results and discussion

4.3.1. Preparation of sacrificial PS-*b*-P2VP stamps

Sacrificial PS-*b*-P2VP stamps were prepared as schematically displayed in Figure 4.1. To topographically pattern the surfaces of the sacrificial PS-*b*-P2VP stamps forming contact to the counterpart surfaces to be stamped, molten PS-*b*-P2VP was molded against macroporous Si (mSi) [82,83]. The mSi contained hexagonal arrays of macropores with a center-to-center distance of 1.5 μm (Figure 4.1A). The inverse-pyramidal mouths of the mSi macropores (Figure 4.1B) resulted from etch pits formed by wet-chemical pattern transfer following photolithographic prepatterning of silicon wafers. The positions of the etch pits defined the positions of the mSi macropores (pore depth ∼1.8 μm) generated by photoelectrochemical etching. The mSi macropores had a neck with a diameter of ∼530 nm directly below the inverse-pyramidal pore mouths. Below the neck, the mSi macropores widened and reached a diameter of 710 nm (Figure 4.1B). The surface of the mSi-initially consisting of a thin native silica layer-was coated with PFDTS following procedures reported elsewhere [86]. PS-*b*-P2VP sandwiched in between surface-modified mSi and self-ordered AAO was melted (Figure 4.1C) [110]. The self-ordered AAO containing arrays of nanopores with a pore diameter of 300 nm, a lattice period of 500 nm, and a pore depth of 1.0 μm reinforced the PS-*b*-P2VP specimens. In this way, bending of the PS-*b*-P2VP specimens and formation of undulations during the preparation of the sacrificial PS-*b*-P2VP stamps were prevented. During the annealing of the PS-*b*-P2VP the low surface energy of the surface-modified mSi prevented complete infiltration of the mSi macropores; only the inverse-pyramidal pore mouths were filled with PS-*b*-P2VP. Furthermore, the neck of the mSi macropores is an entropic barrier to infiltration; overcoming this barrier

would require entropically unfavorable stretching of the PS-*b*-P2VP chains (Figure 4.1D). After cooling to room temperature, the surface-modified mSi was nondestructively detached from the vitrified PS-*b*-P2VP specimens. As a result, PS-*b*-P2VP films with arrays of truncated pyramids at the initial positions of the mSi macropores were obtained, while the mSi could be reused as mold (Figure 4.1E).

In the next step, continuous nanopore systems in the topographically patterned PS-*b*-P2VP specimens still attached to self-ordered AAO were formed by swelling-induced pore generation with hot ethanol, which is a solvent selective to P2VP [20,23,85]. A protocol established for the PS-*b*-P2VP was used here that results in the formation of continuous nanopore systems (Figure 4.1F) characterized by a mean pore diameter of ~40 nm, a specific surface area of 10 m^2/g, and a total pore volume of 0.05 cm^3/g [85]. Osmotic pressure drives the ethanol into the P2VP minority domains. The volumes of the P2VP minority domains increase because the P2VP blocks tend to maximize favorable interactions with ethanol molecules by assuming stretched conformations. The glassy PS matrix in turn undergoes structural reconstruction to accommodate the increased volumes of the P2VP minority domains swollen with ethanol. Bending and the development of macroscopic waviness related to volume expansion during swelling-induced pore generation in the PS-*b*-P2VP specimens were prevented by the reinforcement with self-ordered AAO. Removal of the ethanol by evaporation results in entropic relaxation of the expanded P2VP blocks that transform to coils, while the glassy PS matrix fixates the reconstructed morphology. Consequently, nanopores with walls consisting of coiled P2VP blocks form in place of the expanded P2VP domains swollen with ethanol. To ensure that an isotropic pore network inside a sufficiently stable spongy-continuous scaffold forms, asymmetric PS-*b*-P2VP containing PS as matrix component was used. The nanoporous PS-*b*-P2VP specimens were then subjected to oxygen plasma. The sacrificial PS-*b*-P2VP stamps obtained in this way, which are still connected to self-ordered AAO, may be used for sacrificial stamping and then recovered by again molding them against mSi and repeating steps C–F displayed in Figure 4.1. Optionally, the self-ordered AAO can be selectively etched (Figure

4.1G) to facilitate the loading of the sacrificial stamps with additional components that may further modify and/or functionalize the stamped submicron PS-*b*-P2VP dots. For the sacrificial stamping experiments reported here, freestanding and nanoporous sacrificial PS-*b*-P2VP stamps with a thickness of ~240 μm were used (Figure 4.2).
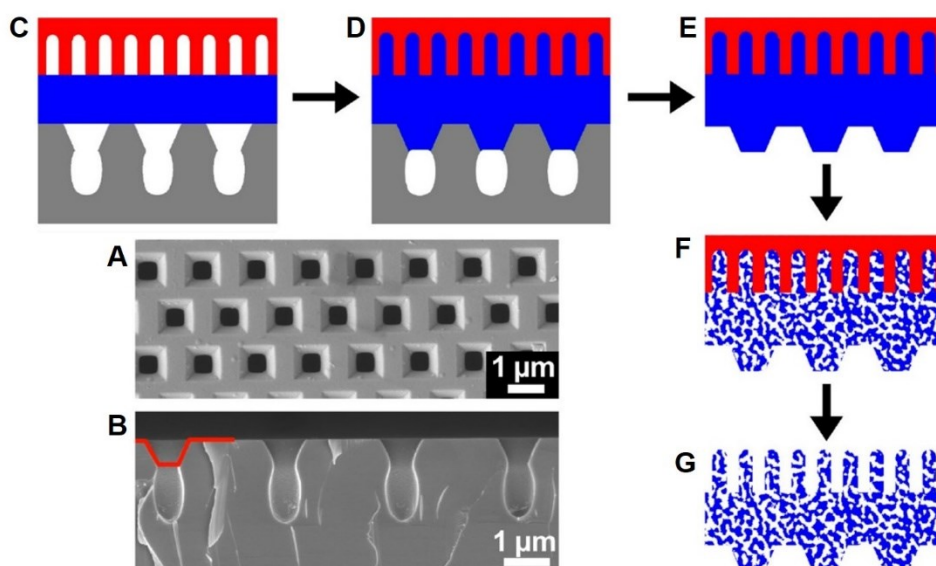
Figure 4.1. Preparation of PS-*b*-P2VP stamps. (A) Top-view SEM image and (B) cross-sectional SEM image of mSi in which the cross-section of a contact element of a sacrificial PS-*b*-P2VP stamp is indicated by a red line. (C–G) Schematic diagram displaying the preparation of PS-*b*-P2VP stamps. (C) Molten PS-*b*-P2VP (blue) is placed between self-ordered nanoporous AAO (red, on the top) and mSi (gray, at the bottom) modified with a perfluorinated silane. (D) The PS-*b*-P2VP melt partially infiltrates the macropores of the surface-modified mSi. (E) After vitrification of the PS-*b*-P2VP, the surface-modified mSi is nondestructively detached from the PS-*b*-P2VP that is patterned with arrays of truncated pyramids at the initial positions of the mSi macropores. (F) Continuous nanopore systems are generated in the PS-*b*-P2VP by swelling-induced pore generation. The self-ordered AAO reinforces the PS-*b*-P2VP specimens during swelling-induced pore generation and prevents bending and emergence of macroscopic waviness. The truncated pyramids obtained by molding the PS-*b*-P2VP against surface-modified mSi are the contact elements of the obtained sacrificial PS-*b*-P2VP stamps forming contact to the counterpart surfaces during sacrificial stamping. (G) Optionally, the self-ordered AAO can be selectively etched.
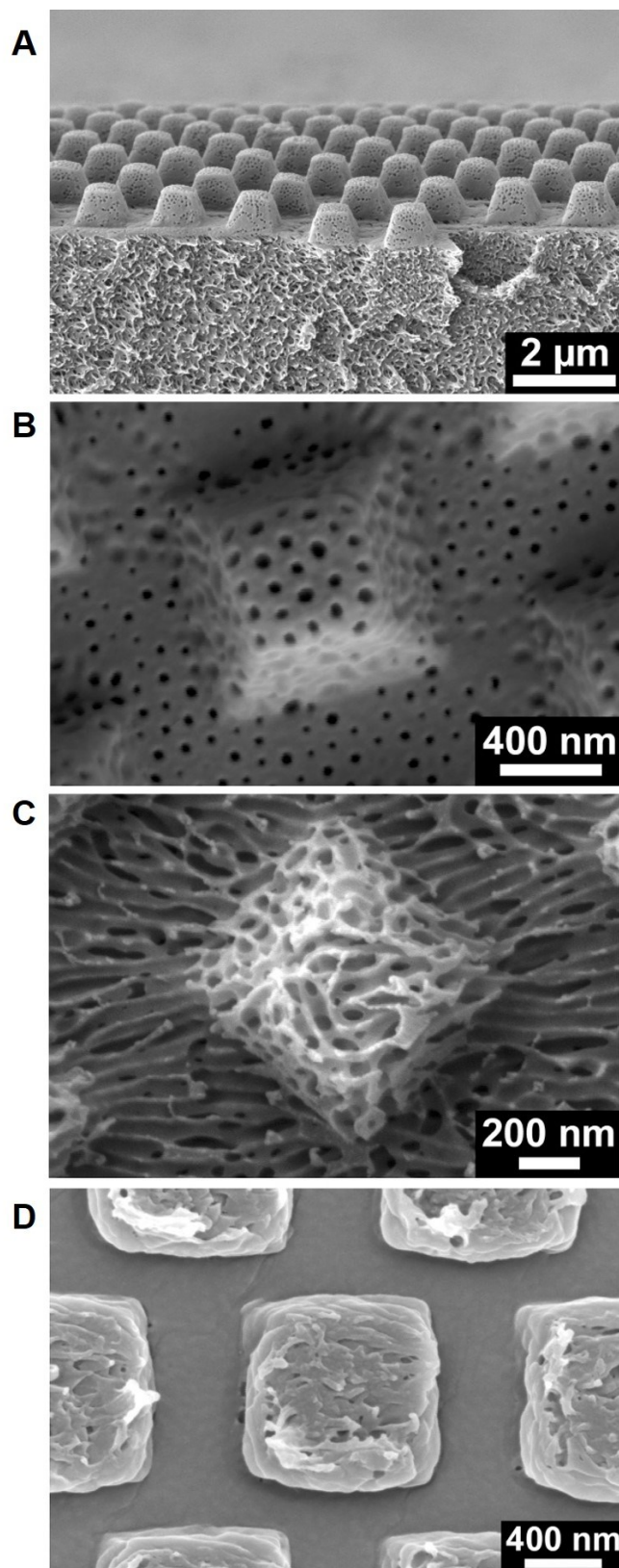
Figure 4.2. SEM images of PS-*b*-P2VP stamps. (A) Cross-section and (B) single contact element prior to oxygen plasma treatment. (C) Single contact element after oxygen plasma treatment (4 min at 100 W). (D) Contact elements of a PS-*b*-P2VP stamp after sacrificial stamping.

4.3.2. Sacrificial stamping

Sacrificial stamping was carried out by gluing sacrificial PS-*b*-P2VP stamps onto steel cylinders that were pressed against counterpart surfaces located on a balance (Figure 4.3). The load was controlled *via* the displayed mass. Using sacrificial PS-*b*-P2VP stamps, we stamped hexagonal arrays of submicron PS-*b*-P2VP dots with a lattice constant of 1.5 μm (Figure 4.4 and Figure 4.5) corresponding to the lattice constant of the mSi template initially used to topographically pattern the sacrificial PS-*b*-P2VP stamps. Sacrificial stamping requires at first the formation of adhesive contact between the contact elements of the sacrificial PS-*b*-P2VP stamps and the counterpart surfaces (Figure 4.3B). We enforced the formation of adhesive contact by controlled application of load. Moreover, formation of adhesive contact was promoted as follows.

(i) The outer surfaces of the sacrificial PS-*b*-P2VP stamps consisted of P2VP [19,22]. The counterpart surfaces used here, silicon wafers covered by a native silica layer and glass slides, had hydroxyl-terminated surfaces. It was previously reported that strong attractive interactions between the pyridyl groups of P2VP and hydroxyl groups on the surface of silica substrates exist [113]. Hence, specific chemical interactions between the P2VP surfaces of the contact elements of the sacrificial PS-*b*-P2VP stamps and the hydroxyl-terminated counterpart surfaces enhance adhesion.

(ii) The sacrificial PS-*b*-P2VP stamps were topographically patterned with hexagonal arrays of contact elements having the shape of truncated pyramids (Figure 4.2A–C). The truncated pyramids with a height of ~670 nm had flat, square-shaped upper surfaces with edge lengths of ~550 nm (Figure 4.2B,C) that were congruent to the cross-sectional areas of the macropore necks of the mSi (Figure 4.1A). These flat contact surfaces of the contact elements facilitated formation of tight adhesive contact to counterpart surfaces as compared to, for example, contact elements with hemispherical tips. Thus, the quadratic shape of the contact surfaces of the contact elements was reproduced by the stamped PS-*b*-P2VP dots.
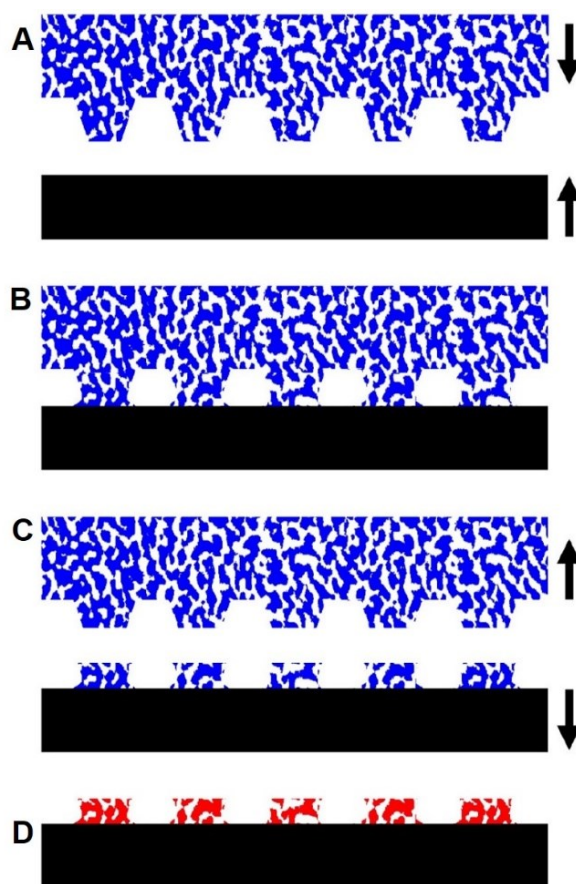
Figure 4.3. Sacrificial stamping of arrays of submicron PS-*b*-P2VP dots. (A) A monolithic nanoporous PS-*b*-P2VP stamp topographically patterned with truncated-pyramidal contact elements (blue) is pressed against a counterpart surface (black) located on a balance. (B) The contact elements of the stamp form contact with the counterpart surface under a load controlled via the mass displayed by the balance. (C) Upon retraction of the nanoporous PS-*b*-P2VP stamp, the contact elements rupture in such a way that their tips remain attached to the counterpart surface as submicron PS-*b*-P2VP dots (blue). The PS-*b*-P2VP, which the residual PS-*b*-P2VP stamp consists of, can be recycled. (D) The submicron PS-*b*-P2VP dots thus deposited onto the counterpart surface can be further modified so that functionalized submicron PS-*b*-P2VP dots (red) are obtained.

(iii) While the counterpart surfaces can be considered as rigid and nondeformable, the spongy sacrificial PS-*b*-P2VP stamps are deformable. As discussed above, the contour of the submicron PS-*b*-P2VP dots was roughly rectangular, such as the contact surfaces of the contact elements of the sacrificial PS-*b*-P2VP stamps. However, the edge lengths of the submicron PS-*b*-P2VP dots amounted to ~900 nm and exceeded, therefore, the edge lengths of the contact surfaces of the contact elements, as apparent from Figure 4.2B,C, by ~65%. Hence, in the course of

sacrificial stamping the contact elements were compressed. Sacrificial stamping converted the open spongy morphology of the sacrificial PS-*b*-P2VP stamps into a more densified morphology (Figure 4.2D). The areas of the densified contact elements matched those of the stamped submicron PS-*b*-P2VP dots. The deformability of the contact elements increases the actual contact area between a contact element and the counterpart surface, which in turn results in enhanced adhesion per contact element.

Secondly, the contact elements must rupture upon retraction of the sacrificial PS-*b*-P2VP stamps. As a result, the parts of the contact elements in adhesive contact with the counterpart surfaces remain attached to the latter after removal of the sacrificial PS-*b*-P2VP stamps (Figure 4.3C). The height of the stamped submicron PS-*b*-P2VP dots ranged from ~100 to ~200 nm (Figure 4.4C and Figure 4.6). The roughness of the surface topography of the submicron PS-*b*-P2VP dots reflects the nanoporous-spongy nature of the sacrificial PS-*b*-P2VP stamps. The crazing behavior of thin PS-*b*-P2VP films has been reported to be complex [114,115]. Nevertheless, it was assumed that the following aspects promote the rupture of the contact elements.

(i) The spongy-nanoporous morphology of the sacrificial PS-*b*-P2VP stamps reduces their tensile strength because of confinement-induced reduction in the volume density of intermolecular entanglements. The viscosity of polymers as well as their behavior when subjected to stress are crucially related to the presence of intermolecular entanglements. The molecular weight of the PS blocks forming the majority component of the PS-*b*-P2VP amounts to 101 000 g/mol and lies, therefore, well above the threshold value M_c of PS for the occurrence of intermolecular entanglements ($M_c \sim$ 31 200 g/mol at 490 K) [116]. However, PS chains in thin PS homopolymer films have been reported to be less entangled than in the bulk, corresponding to a confinement-induced increase in M_c [117,118]. The nanopore walls in the sacrificial PS-*b*-P2VP stamps have thicknesses in the 100 nm range and below so that geometric restrictions similar to those in thin PS films apply. Moreover, the high incompatibility of the PS

and P2VP blocks imposes additional constraints on the formation of intermolecular entanglements. Hence, the volume density of intermolecular entanglements within the PS domains in the PS-*b*-P2VP stamps should be lower than in bulk PS-*b*-P2VP.

(ii) Prior to sacrificial stamping, the sacrificial PS-*b*-P2VP stamps were subjected to oxygen plasma treatment. The oxygen plasma treatment increased the areas of the nanopore openings at the surface of the sacrificial PS-*b*-P2VP stamps, as is obvious from a comparison of Figure 4.2B and Figure 4.2C. The oxygen plasma also cleaves some PS-*b*-P2VP chains close to the surface of the sacrificial PS-*b*-P2VP stamps into shorter segments. It is a straightforward assumption that cleavage of PS-*b*-P2VP chains close the surface of the contact elements and, therefore, close to the contact interface between contact elements and counterpart surface facilitates the rupture of the contact elements.
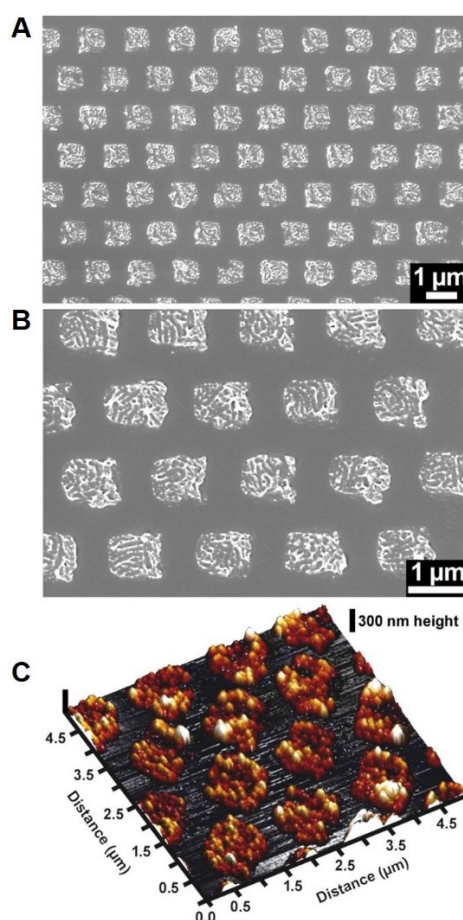
Figure 4.4. Arrays of nanostructured submicron PS-*b*-P2VP dots deposited on silicon wafers by sacrificial stamping. (A,B) Scanning electron microscopy images. (C) AFM topography image.
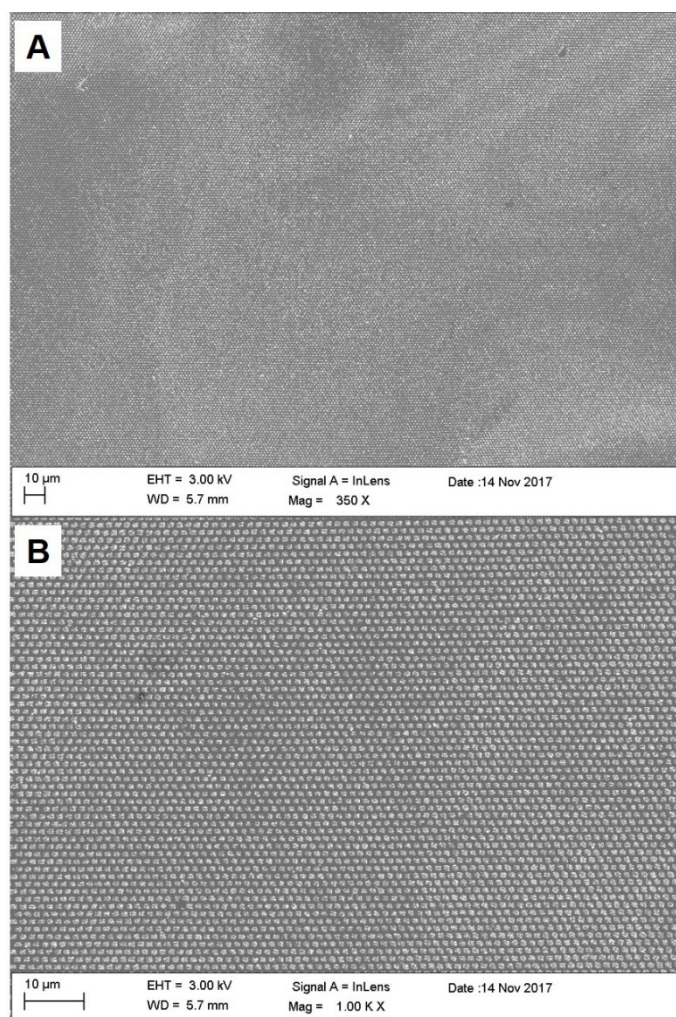
Figure 4.5. Large-area (A) and intermed asiate magnification (B) SEM image of an array of submicron PS-*b*-P2VP dots on a Si wafer generated by sacrificial stamping.
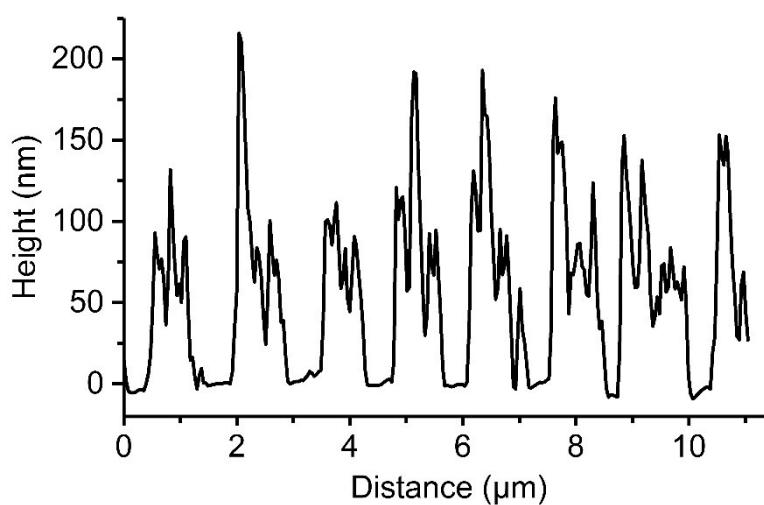
Figure 4.6. AFM topography line profile of PS-*b*-P2VP dots stamped on a Si wafer.

61

4.3.3. Modification of PS-*b*-P2VP dots

Since the outer surfaces of the submicron PS-*b*-P2VP dots consist of P2VP blocks, the pyridyl groups of the latter are exposed to the environment and can be used for further functionalization. As an example, citrate-stabilized AuNPs with a diameter of 35 nm were attached to the submicron PS-*b*-P2VP dots by immersing arrays of submicron PS-*b*-P2VP dots on Si wafers into AuNP suspensions with a pH value of 3.5. The negatively charged AuNPs adhered to partially protonated pyridyl moieties by van der Waals interactions and ionic interactions (P2VP is protonated at pH $\leqslant$ 4.1) [105]. Evaluation of 10 submicron PS-*b*-P2VP dots revealed that on average 69 ± 13 AuNPs were bound to a submicron PS-*b*-P2VP dot (Figure 4.7A). It is also possible to incubate the sacrificial PS-*b*-P2VP stamp prior to sacrificial stamping with a functional material and to transfer the latter along with the submicron PS-*b*-P2VP dots to a counterpart surface. As an example, a sacrificial PS-*b*-P2VP stamp was filled with a rhodamine B solution and let the solvent evaporate. Then, arrays of submicron PS-*b*-P2VP dots containing rhodamine B were deposited on a glass slide by sacrificial stamping. The presence of rhodamine B was made evident by total internal reflection fluorescence microscopy (TIRFM) imaging the fluorescence emission of rhodamine B (Figure 4.7B).
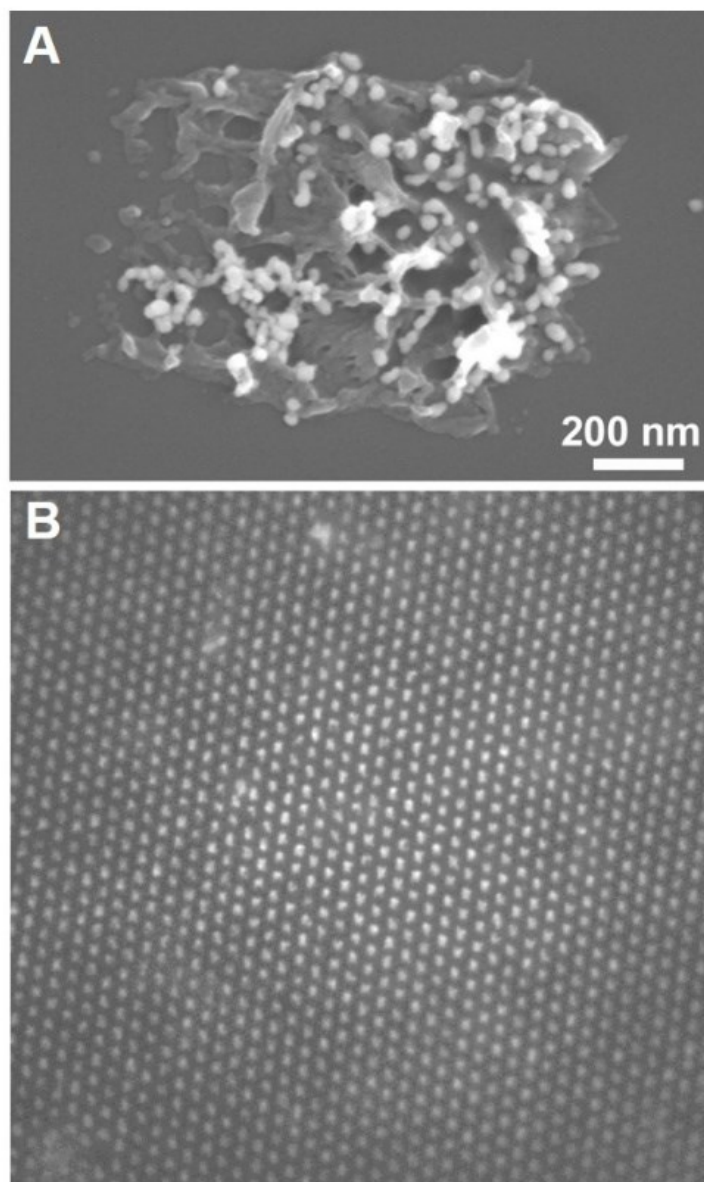
Figure 4.7. Functionalized submicron PS-*b*-P2VP dots obtained by sacrificial stamping. (A) Submicron PS-*b*-P2VP dot on a Si wafer functionalized with gold nanoparticles. (B) TIRFM image (edge length 54.5 μm) of the fluorescence of submicron PS-*b*-P2VP dots containing rhodamine B stamped on a glass slide.

4.4. Conclusion

In this Chapter, the results of preliminary contact formation and stamping experiments with spongy, non-inked PS-*b*-P2VP stamps are described. From these experiments, an ink-free lithographic approach for the transfer of parts of the sacrificial spongy PS-*b*-P2VP stamp to a counterpart surface emerged. Using sacrificial PS-*b*-P2VP stamps penetrated by spongy-

continuous nanopore systems with truncated pyramids as contact elements, arrays of spongy submicron PS-*b*-P2VP dots were stamped on silicon wafers and glass slides. Sacrificial stamping requires that adhesion of the stamp's contact elements to the counterpart surface is stronger than cohesion within the stamp. The enhanced deformability of the sacrificial PS-*b*-P2VP stamps originating from their spongy-nanoporous morphology facilitated formation of adhesive contact between contact elements and counterpart surfaces. Suppression of intermolecular entanglements induced by the confinement of the thin nanopore walls inside the sacrificial PS-*b*-P2VP stamps, as well as chain cleavage by oxygen plasma treatment, supported the rupture of the contact elements upon stamp retraction. Taking into account that the underlying polymer physics is generic, it is assumed that the methodology reported here is applicable to any polymeric stamp with spongy morphology. The PS-*b*-P2VP, which the sacrificial PS-*b*-P2VP stamps consist of, is recyclable. The pyridyl groups of the P2VP blocks forming the outer surface of the submicron PS-*b*-P2VP dots facilitated further functionalization of the latter, for example, with AuNPs or with dyes. Arrays of submicron PS-*b*-P2VP dots stamped onto glass slides can be used as substrates for advanced optical microscopy, such as TIRF microscopy, as well as for Raman microscopy. Potential applications of BCP dot arrays generated by sacrificial stamping may include locally resolved preconcentration sensing and locally resolved monitoring of cellular interactions preconcentrated at the submicron BCP dots. Moreover, sacrificial stamping may yield lab-on-chip configurations consisting of arrays of microreactors for locally confined chemical reactions.

5. Scanner-based capillary stamping

5.1. Introduction

This Chapter reports the main achievement of this thesis, the development of scanner-based capillary stamping (SCS) with spongy nanoporous BCP stamps, which combines the advantages of parallel and serial stamping with continuous operation not interrupted by re-inking.

Chemical and/or topographical patterning of surfaces as well as the generation of nanostructures and microstructures by contact lithography have been the focus of significant research efforts for more than two decades. A diverse range of methods has been developed to this end. Generally, contact lithography can be divided into two categories on the basis of the patterning strategy: (i) scanning probe-based serial writing approaches yielding arbitrary patterns; (ii) stamp-based parallel stamping approaches producing large-area patterns. The latter group of contact-lithographic approaches includes classical soft lithography with elastomeric stamps [1,2] such as μCP [3,4] and PPL [5-7] and involves the transfer of molecules adsorbed on the stamp surface to a counterpart surface, on which consequently thin ink layers are deposited. Scanning probe-based approaches include DPN [6-9], the use of single cantilever tips modified for continuous liquid supply [11,119-121], and micropipetting techniques [10]. High-throughput contact lithography would require the combination of large-scale parallel stamp-material deposition and continuous ink supply that was so far achieved only for single cantilever tips with limitations regarding the throughput. The massively parallel high-throughput deposition of large-area microdroplet arrays has remained challenging.

The SCS technique has been developed here to achieve high-throughput, low-cost, and digitized generation of large-area microdroplet arrays. Conventional parallel stamping approaches based on the use of solid stamps only allow the transfer of molecules adsorbed on the stamp surface to the substrate to be patterned and often require controlled atmospheric conditions, frequent readsorption of ink or long cycle times. The nanoporous SCS stamps consist of arrays of

polymeric ink dispensing elements that are connected by a thin polymeric film of the same material to a layer of spongy porous silica glass [122], referred to as controlled porous glass (CPG). CPG, polymeric film and polymeric dispensing elements form composite SCS stamps with continuous, spongy nanopore systems penetrating the entire SCS stamp and enabling ink transport from the reverse side of the SCS stamp to the tips of the dispensing elements. The SCS process conducted with an NLP 2000 device (Nanoink Inc., USA): (i) The nanoporous SCS stamp is filled with ink through the hole of a custom-made stamp-holder. (ii) Upon approach of the ink-soaked nanoporous SCS stamp to a substrate to be stamped, capillary bridges of the ink will form between each dispensing element and the counterpart surface. (iii) Subsequent retraction of the nanoporous SCS stamp results in redistribution of the ink between dispensing elements and counterpart surface. As a result, ink microdroplet arrays remain on the substrate; the ink microdroplets are located at the former positions of the dispensing elements of the SCS stamp. Thus, large-area arrays of non-volatile fluidic ink microdroplets are generated on the substrates to be patterned. By computer-controlled displacement of the SCS stamps, complex and arbitrary structures can be produced. Sizes of the stamped microdroplets can be controlled by adjusting both the surface wettability and the dwell time of the contact. For a proof-of-concept, the ability of SCS technique for multi-ink stamping was also demonstrated.

5.2. Experimental section

5.2.1. Materials

5.2.1.1. Chemicals

Asymmetric PS-b-P2VP (M_n(PS) = 101 000 g mol^{-1}; M_n(P2VP) = 29 000 g mol^{-1}; M_w/M_n(PS-b-P2VP) = 1.60, volume fraction of P2VP 21%; bulk period 51 nm) was obtained from Polymer Source Inc., Canada. P2VP homopolymer (M_w = 41 000 g mol^{-1}; M_n = 37 000 g mol^{-1}; M_w/M_n = 1.11) was obtained from Sigma-Aldrich. Hexamethyldisilazane (HMDS) was supplied by

ABCR GmbH. (3-Aminopropyl)triethoxysilane (APTES) and trichloro(1H,1H,2H,2H-perfluorooctyl)silane (PFOTS) were purchased from Sigma-Aldrich. Tetrahydrofuran (THF), hydrogen peroxide (30% H_2O_2), sulfuric acid (98% H_2SO_4) and ethanol were supplied by local manufacturers in the analytical grade.

5.2.1.2. Silicon master molds

Silicon master molds were prepared as reported previously [5]. The surface of the silicon master molds was topographically patterned with tetragonal lattices of pyramidal indentations with a nearest-neighbor distance of 200 μm. The edge length of the quadratic pyramid bases amounted to 50 μm. The depth of the pyramidal indentations also amounted to 50 μm. Before use, the surface of the silicon master molds covered by native oxide was silanized with PFOTS. For this purpose, silicon master molds were at first treated with a boiling mixture containing 98% H_2SO_4 and 30% H_2O_2 at a volume ratio of 7:3 for 30 min, followed by rinsing with deionized water and drying in an argon flow. Then, the silicon master molds were kept under a vacuum at room temperature for 5 h in the presence of 0.2 mL PFOTS.

5.2.1.3. Controlled porous glasses

CPG with an average pore diameter of 102 nm, a thickness of 500 μm and porosity of 54% was prepared by spinodal decomposition of alkali borosilicate glasses and subsequent leaching of the boron-rich phase following procedures reported elsewhere [122].

5.2.1.4. Silicon wafers

Silicon wafers (Part No. L14025) were obtained from Siegert Wafer GmbH, Aachen. To silanize the silicon wafers with HMDS or APTES, they were at first treated with a boiling mixture containing 98% H_2SO_4 and 30% H_2O_2 at a volume ratio of 7:3 for 30 min, followed by rinsing

with deionized water and drying in an argon flow. Then, the silicon wafers were heated for 5 h at 100 °C in the presence of 0.2 mL of the respective silane under ambient pressure. For further use, the silanized silicon wafers were cut into squares with an edge length of ~1cm.

5.2.1.5. Inks

For single-ink stamping, poly(1-decene) (Inland 45 Vacuum pump fluid; M_w = 490 g mol^{-1}; M_n = 390 g mol^{-1}; M_w/M_n = 1.26; kinematic viscosity at 40 °C as specified by the manufacturer: 53 cSt; vapor pressure < 1×10^{-7} torr) purchased from Inland Vacuum Industries (Churchville, NY) was used as ink.

For multi-ink stamping, solutions of lipid I (ink I) and lipid II (ink II) in poly(1-decene) with a concentration of 0.1 mg/ml were used as inks. Lipid I was 18:1 Liss Rhod PE (full name: [1,2-dioleoyl-sn-glycero-3-phosphoethanolamine-N-(lissamine rhodamine B sulfonyl) (ammonium salt)]; https://avantilipids.com/product/810150) and lipid II was 18:1 PE CF (full name: [1,2-dioleoyl-sn-glycero-3-phosphoethanolamine-N-(carboxy-fluorescein)]; https://avantilipids.com/product/810332). Lipids I and II were both obtained from Avanti Polar Lipids, Inc., USA.

5.2.2. Fabrication of SCS stamps

PS-*b*-P2VP films were prepared by dropping 50 µL (stamp for single-ink stamping) or 100 µL (stamp for multi-ink stamping) of a solution of 100 mg PS-*b*-P2VP per mL THF onto a silicon wafer extending 5 mm × 5 mm (stamp for single-ink stamping) or 10 mm × 5 mm (stamp for multi-ink stamping). After complete evaporation of the THF, the obtained PS-*b*-P2VP films were non-destructively and automatically detached by exposure to ethanol for 24 h at room temperature. Then, PS-*b*-P2VP films were sandwiched between CPGs and surface-modified silicon master molds at 220 °C for 4 h under a vacuum while a load of ~2.75 bar was applied.

After cooling to room temperature at –1 K/min, silicon master molds were detached from PS-*b*-P2VP by treatment with ethanol at room temperature for ∼30 min. For swelling-induced pore generation, PS-*b*-P2VP attached to CPG was treated with ethanol at 60 °C for 4 h. Under the conditions applied here, spongy-continuous pore systems with a mean pore diameter of ∼40 nm, a specific surface area of 10 m^2/g, and a total pore volume of 0.05 cm^3/g form [85].

5.2.3. Scanner-based capillary stamping

All stamping experiments were carried out with an NLP 2000 device (Nanoink Inc., USA) equipped with three encoded piezo-driven linear substrate stage displaceable in the X, Y and Z directions as well as with encoded goniometer stage (settings are referred to T_x and T_y), which can move 40 mm in the X and Y directions as well as 10 mm in the Z direction. The in-built camera system has a spatial resolution better than 1 µm and a digitally controlled halogen illumination system. The NLP 2000 device was controlled with an onboard software system that allows designing patterns and setting dwell times (i.e., the contact time between stamps and substrates).

5.2.3.1. Single-ink inking

2 mm thick custom-made metal stamp-holders extending 30 mm × 80 mm with a square hole extending 10 mm × 10 mm were used. CPG surfaces of SCS stamps were glued onto the stamp-holders with a two-component epoxy resin adhesive (UHU, Germany) in such a way that stamps covered the holes in the stamp-holders. Then, stamp-holders were glued onto the bars of the custom-made holders that were in turn mounted on the NLP 2000 device. For inking, 200 µL poly(1-decene) was deposited into the holes of the metal stamp-holders. After a wait time of 2 h, the ink-soaked SCS stamps were fully transparent.

5.2.3.2. Multi-ink inking

For multi-ink stamping, 2 mm thick custom-made stamp holders extending 30 mm × 80 mm that contained two holes extending 5 mm × 10 mm were used. The CPG surfaces of SCS stamps were glued onto the stamp-holders as described above. SCS stamps were then cut into two separate parts (part I and part II) with a sharp knife in such a way that each part covered one of the holes in the stamp-holders. 20 µL portions of inks I and II were deposited directly onto surfaces of the pyramid-shaped dispensing element tips of parts I and II of the SCS stamps using an Eppendorf pipette. After a wait time of 1 h, the stamp-holders were mounted onto the NLP 2000 device. Then, 100 µL poly(1-decene) was deposited onto each part of the SCS stamps through the two holes in the stamp-holders. After a wait time of 2 h, the ink-soaked SCS stamps were fully transparent.

5.2.3.3. Leveling of the SCS stamps

As SCS stamps were manually glued onto the stamp-holders, slight misalignment between the plane of the stamps' contact elements and the substrate surfaces could not be avoided. To compensate this misalignment, the leveling of the stamps was performed by adaptation of an optical leveling method reported previously [123]. In the beginning, the substrate stage was moved into its starting position ($T_x = 0$ and $T_y = 0$). The silicon substrate was brought into contact with pyramid-shaped tips of the dispensing elements of the SCS stamp. As soon as the substrate stage was approached to a position about 100–200 µm away to from the tips of the pyramid-shaped dispensing elements, shadows around the contact elements appeared due to the reflective nature of the silicon substrates. When the pyramid-shaped tips of the dispensing elements contacted the substrate surface, circular ink droplets formed that were imaged by the camera of the NLP 2000 device located on top of the inked transparent SCS stamp. In the course of the initial approach of the silicon substrate towards to the stamp, some pyramid-shaped dispensing element tips might touch the silicon substrate harder than others, resulting in local

variations of the sizes of the deposited ink drops. The substrate stage was stepwisely tilted about the two goniometer axes. For each T_x/T_y setting, a stamping process was carried out, and the variance in microdroplet sizes was evaluated by the naked eye. This procedure was repeated until the microdroplet size was uniform all over the silicon substrates, indicating that the plane of the silicon substrate stage was parallel to the plane of the stamps. For leveling of SCS stamps for multi-ink stamping, a similar method was applied, but only one of the two separated parts was leveled assuming conformity of the other part. Small misalignments are still to be expected after the leveling.

5.2.3.4. Stamping

After leveling, silanized silicon wafers were mounted onto the substrate stage of the NLP 2000 device and employed as substrates in the subsequent stamping procedures. The silanized silicon wafers were approached to the SCS stamps until the distance amounted to about 100 µm. Then, the SCS stamps were further approached to the silanized silicon wafers in steps of 10 µm towards until contact was formed. Contact formation was detected optically by the in-built camera when observing formation of circular dots at the contact points of the tips of the dispensing elements and the substrate to be stamped. After a predefined dwell time, the silanized silicon wafers were retracted by 50 µm, moved to the next set position, and brought in contact with the SCS stamps again for the next stamping step. This cycle was repeated multiple times until the predefined stamping program was completed.

The general procedure for multi-ink stamping was an adaptation of a previously published approach [124,125]. Multi-ink microdroplet patterns were stamped by repositioning the piezo-driven substrate stage in such a sequence that sub-patterns of each particular ink were generated next to each other. The initial offset between parts I and II of the SCS stamps was corrected by visual *in situ* alignment using an optical microscope attached to the NLP 2000 device.

5.2.4. Characterization

5.2.4.1. Mercury intrusion porosimetry

Mercury intrusion porosimetry (MIP) measurements were carried out on a Pascal 140/440 porosimeter (Thermo Fisher Scientific, Waltham, MA) over a pressure range of 0.15–200 MPa. Pore size distributions were derived from the MIP data with the Pascal software according to the Washburn equation, setting the mercury contact angle to 141°; the measured pressure range corresponds to pore diameters between 14 nm and 10 µm.

5.2.4.2. Scanning electron microscopy

SEM investigations were carried out on a Zeiss Auriga microscope operated at an accelerating voltage of 5 kV. Prior to the SEM investigations, the samples were coated with a ~5 nm thick iridium layer.

5.2.4.3. Contact angle measurements

Ink contact angles were measured in the sessile drop mode at a humidity of 27% and a temperature of 23 °C using a drop shape analyzer DSA100 (Krüss, Germany). The volumes of the liquid droplets were 3 µL. All contact angle measurements for a specific sample type were repeated on six different samples. P2VP homopolymer films were prepared by spin coating a solution of 10 wt% P2VP in ethanol onto a silicon wafer at 1000 rpm, followed by drying in vacuum.

5.2.4.4. Optical microscopy

Optical images of drop arrays generated by capillary microstamping were acquired with an

upright fluorescence microscope (reflection mode, Eclipse 80i, Nikon Germany) equipped with a sensitive camera (Nikon DS-Qi2 camera from Nikon Germany), a broadband excitation light source (Intensilight, Nikon), and a Texas Red filter set (Y-2E/C, Nikon). Drop diameter analysis was carried out using NIS-Elements imaging software.

5.2.4.5. White light interferometry

White light interferometry was carried out on a ContourGT-K 3D Optical Microscope using Vision64® Operation and Analysis Software for analyses.

5.3. Results and discussion

5.3.1. Fabrication of SCS stamps

Nanoporous SCS stamps consisting of the asymmetric block copolymer PS-*b*-P2VP attached to CPG [122] are schematically displayed in Figure 5.1A–D. Since the CPG pores had oxidic walls with high surface energy, strong adhesion drew the PS-*b*-P2VP into the CPG pores. The CPG support reinforced the PS-*b*-P2VP specimens. In this way, bending of the PS-*b*-P2VP specimens and formation of undulations during the preparation of the SCS stamps were prevented. In this way, the uniformity and the smoothness of the SCS stamps was significantly improved, and SCS stamps extending 5 mm × 5 mm were obtained (Figure 5.2A). Without the rigid supporting CPGs, the SCS stamps would bend so that they could not be used. As a result, while still connected to the CPGs, PS-*b*-P2VP films with arrays of pyramid-shaped tips at the initial positions of the silicon master molds were obtained (Figure 5.1B–D and Figure 5.2B). Silicon master molds could be reused.

In the next step, continuous nanopore systems in the topographically patterned PS-*b*-P2VP specimens were formed that were still attached to the CPGs by swelling-induced pore
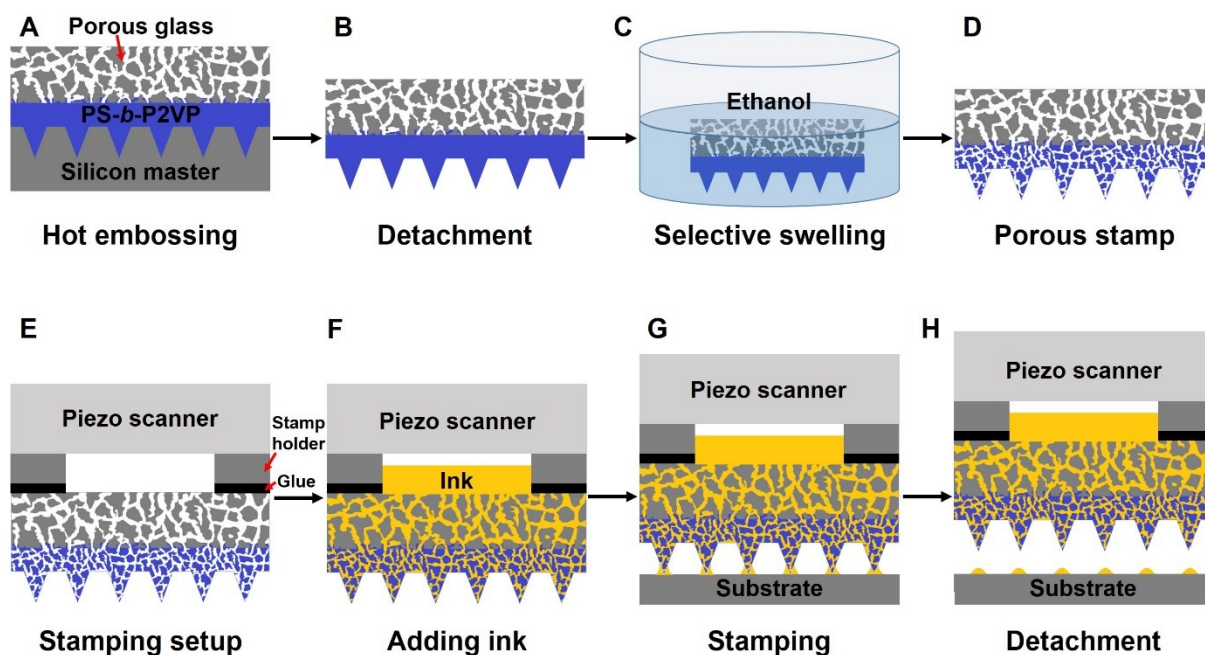
Figure 5.1. Schematic illustration of the scanner-based capillary stamping (SCS). (A) A molten PS-*b*-P2VP film is sandwiched between CPG and a surface-modified silicon master mold in such a way that the openings of the CPG and the surface-modified silicon master mold are in contact with the PS-*b*-P2VP. (B) After cooling to room temperature, the PS-*b*-P2VP/CPG composite is immersed into ethanol to non-destructively detach the surface-modified silicon master. (C) The obtained PS-*b*-P2VP/CPG composite is treated with hot ethanol for swelling-induced pore generation in the PS-*b*-P2VP to obtain (D) spongy nanoporous SCS stamp. (E) The SCS stamp is attached to a custom-made stamp-holder and mounted on an NLP 2000 stamping device. (F) Ink is added through a hole in the stamp-holder and infiltrates the SCS stamp. (G) For stamping, the stamp is brought into contact with the substrate. (H) After stamp retraction, microdroplet arrays remain on the substrate.

generation with hot ethanol, which is a solvent selective to P2VP and non-solvent to PS [20,23,84,85]. We applied a protocol established for the PS-*b*-P2VP used here that results in the formation of continuous nanopore systems (Figure 5.1D and Figure 5.2C–F) characterized by a mean pore diameter of ~40 nm, a specific surface area of 10 m^2/g, and a total pore volume of 0.05 cm^3/g (section 2.4). Bending and the development of macroscopic waviness related to volume expansion during swelling-induced pore generation in the PS-*b*-P2VP specimens were prevented by the reinforcement with rigid CPGs. To ensure that an isotropic pore network inside a sufficiently stable spongy-continuous scaffold forms, we used asymmetric PS-*b*-P2VP containing PS as matrix component. Notably, swelling-induced pore generation method also

applies to the PS-*b*-P2VP inserted into the nanopores of CPGs (Figure 5.2F). As a result, CPG, PS-*b*-P2VP film and PS-*b*-P2VP dispensing elements formed composite SCS stamps with continuous, spongy nanopore systems penetrating the entire SCS stamp. The thickness of the PS-*b*-P2VP layer amounted to ∼62.5 µm (Figure 5.2D).
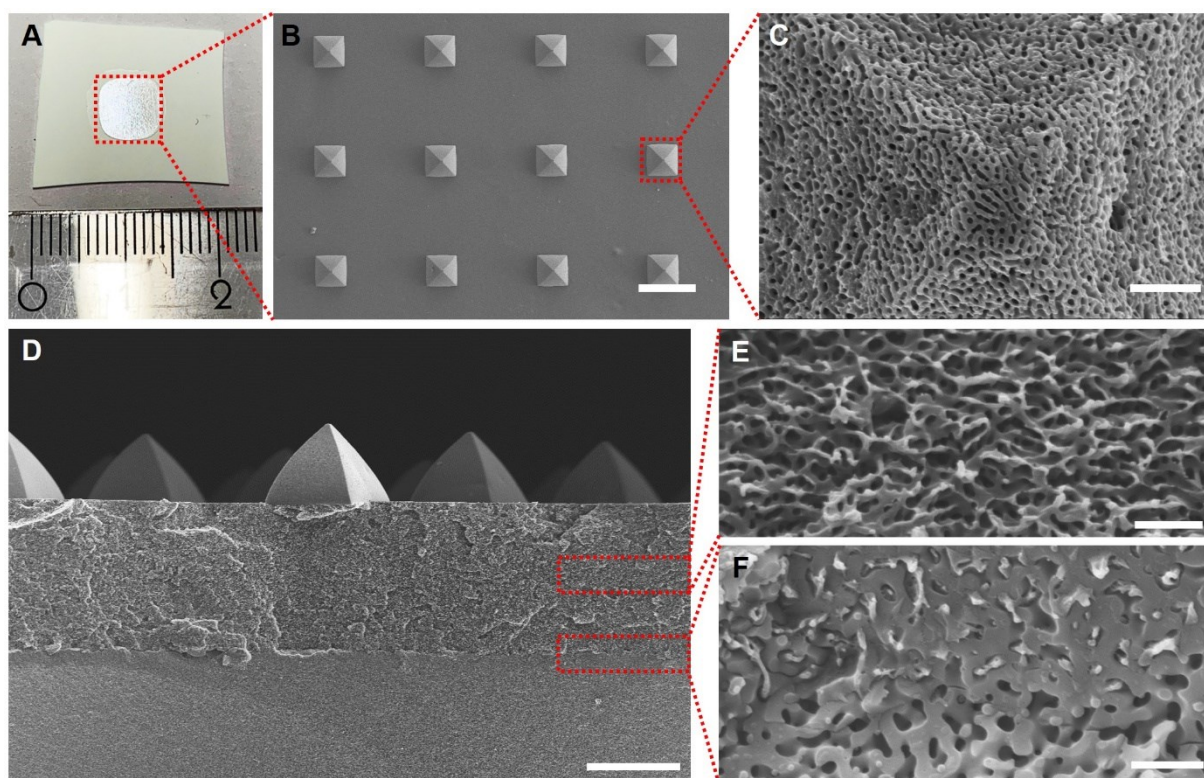
Figure 5.2. SCS stamps. (A) Photograph of a spongy nanoporous SCS stamp extending ∼5 mm × 5 mm (within the square enclosed by the dotted red line) located on a square-shaped CPG membrane extending ∼20 mm × 20 mm. (B–F) Scanning electron microscopy images of the SCS stamp. (B) Top view of the of the contact surface topographically patterned with pyramidal dispensing elements. (C) Tip of a single pyramid-shaped dispensing element. (D) Cross-sectional view of a SCS stamp. (E) Detail of the stamp cross section showing the pore system of the nanoorous PS-*b*-P2VP layer. (F) Detail of the stamp cross section showing the interface between the CPG membrane and the PS-*b*-P2VP layer. The length of the scale bars corresponds to (B) 100 µm, (C) 1 µm, (D) 50 µm, (E,F) 500 nm.

5.3.2. Scanner-based capillary stamping

The SCS experiments were carried out by using poly(1-decene) as a model ink for the following reasons: (i) poly(1-decene) is compatible with PS-*b*-P2VP and does not chemically or

physically react with the material of the SCS stamps. (ii) The kinematic viscosity of the poly(1-decene) used here at 40 °C, as specified by the manufacturer, is 53 cSt. (iii) Poly(1-decene) has an extremely low vapor pressure at room temperature ($< 1\times10^{-7}$ torr), as specified by the manufacturer. Therefore, the evaporation of the stamped poly(1-decene) microdroplets can be neglected.
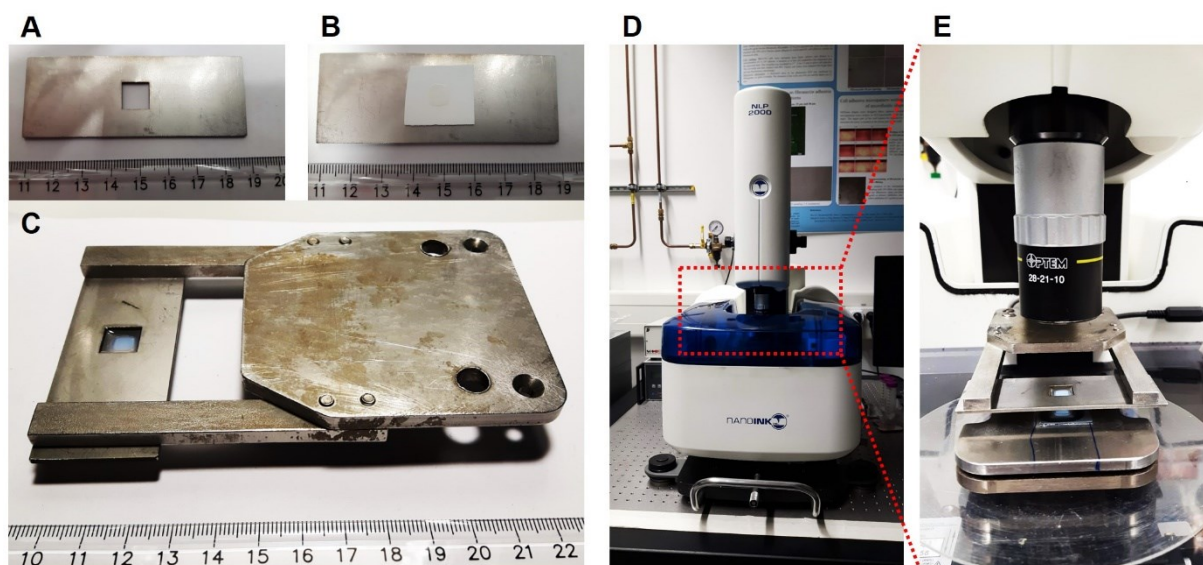
Figure 5.3. Photographs of the SCS setup. (A) Custom-made stamp-holder with one single hole. (B) SCS stamp attached to the custom-made stamp-holder with glue. (C) Stamp-holder with the SCS stamp mounted on the sample holder of the NLP 2000 device. Ink was deposited into the hole of the stamp-holder. (D,E) NLP 2000 device.

In a typical stamping experiment, SCS stamps with dispensing element arrays extending ~0.5 cm × 0.5 cm in size were used. The contact angle of the ink poly(1-decene) on the HMDS-modified silicon wafers (HMDS-Si) used as substrates for SCS is 49.6° ± 2.3°. 2 mm thick custom-made metal stamp-holders extending 30 mm × 80 mm with a square hole extending 10 mm × 10 mm were used (Figure 5.3A). CPG surfaces of SCS stamps were glued onto the stamp-holders (Figure 5.3B) with a two-component epoxy resin adhesive (UHU, Germany) in such a way that stamps covered the holes in the stamp-holders. Then, stamp-holders were glued onto the bars of the custom-made holders (Figure 5.3C,E) that were in turn mounted on the NLP 2000 device (Figure 5.3D). For inking, 200 µL poly(1-decene) was deposited into the holes of

the metal stamp-holders. After a wait time of 2 h, the ink-soaked SCS stamps were fully transparent.

As SCS stamps were manually glued onto the stamp-holders, slight misalignment between the plane of the stamps' contact elements and the substrate surface could not be avoided. To compensate this misalignment, the leveling of the stamps was performed by adaptation of an optical leveling method reported previously [123]. In the beginning, the substrate stage was moved into its starting position ($T_x = 0$ and $T_y = 0$). The silicon substrate was brought into contact with pyramid-shaped tips of the dispensing elements of the SCS stamp. As soon as the substrate stage was approached to a position about 100–200 μm away to from the tips of the pyramid-shaped dispensing elements, shadows (Figure 5.4A) around the contact elements appeared due to the reflective nature of the silicon substrates. When the pyramid-shaped tips of the dispensing elements contacted the substrate surface, circular ink droplets formed that were imaged by the camera of the NLP 2000 device located on top of the inked transparent SCS stamp (Figure 5.4B). In the course of the initial approach of the silicon substrate towards to the stamp, some pyramid-shaped dispensing element tips might touch the silicon substrate harder than others, resulting in local variations of the sizes of the deposited ink drops. The substrate stage was stepwisely tilted about the two goniometer axes. For each T_x/T_y setting, a stamping process was carried out, and the variance in microdroplet sizes was evaluated by the naked eye. This procedure was repeated until the microdroplet size was uniform all over the silicon substrates, indicating that the plane of the silicon substrate stage was parallel to the plane of the stamps. For leveling of SCS stamps for multi-ink stamping, a similar method was applied, but only one of the two separated parts was leveled assuming conformity of the other part. Small misalignments are still to be expected after the leveling.
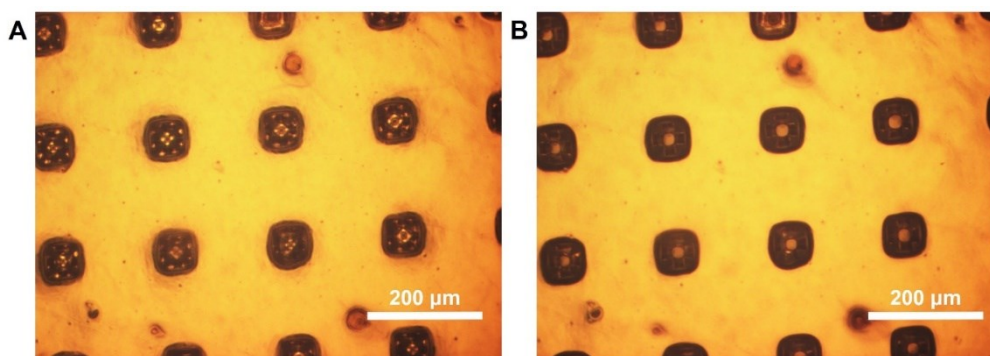
Figure 5.4. Optical microscopy images captured during leveling (A) before and (B) after the tips of the pyramid-shaped dispensing elements of the nanoporous SCS stamp contacted the substrate. The droplet size formed at the contact point is the reference for the leveling in this technique.

After leveling, HMDS-Si was mounted onto the substrate stage of the NLP 2000 device (Figure 5.3D,E). The HMDS-Si was approached to the SCS stamp until the distance amounted to about 100 μm. Following the pre-defined SCS program, the individual pyramid-shaped dispensing elements of the SCS stamp were successively brought into contact with the HDMS-Si multiple times in such a way that the positions where the dispensing elements contacted the HMDS-Si where slightly shifted. The stamp displacements between successive SCS steps were about one order of magnitude smaller than the distances between the tips of the dispensing elements. Typically, matrices of 8 × 10 microdroplets with a microdroplet spacing of 20 μm were generated by one single dispensing element in 80 successive stamping steps with a dwell time of 10 s per stamping step without re-inking. Moreover, a single dispensing element can successively generate several 8 × 10 matrices on different substrates without reinking. Figure 5.5A and Figure 5B show optical microscopy images of adjacent matrices of 8 × 10 matrices consisting of microdroplets with average diameters of 7.78 ± 1.40 μm on the first stamped substrate. Figure 5.5C and Figure 5.5D show optical microscopy images of adjacent matrices of 8 × 10 matrices consisting of microdroplets with average diameters of 7.20 ± 1.33 μm on the tenth successively stamped substrate. Therefore, one individual dispensing element of the SCS stamp can generate at least 800 microdroplets without re-inking. Moreover, Figure 5.6 shows large area views of of poly(1-decene) microdroplet arrays on the first stamped HDMS-Si substrate.
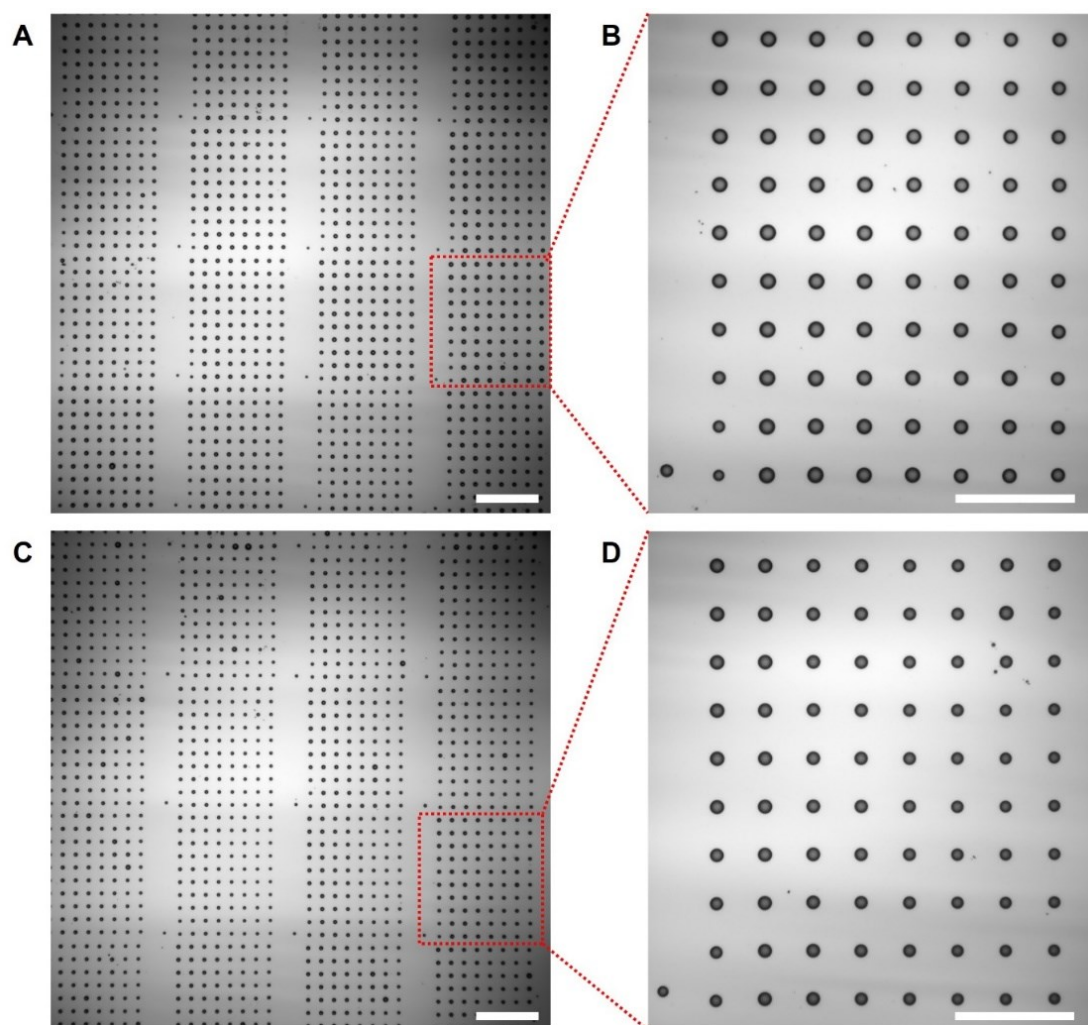
Figure 5.5. Optical microscopy images of poly(1-decene) microdroplet arrays consisting of adjacent matrices of 8 × 10 microdroplets that were generated by 80 stamping cycles with a single dispensing element on HMDS-Si substrates applying a dwell time of 10 s. Exemplary matrices of 8 × 10 microdroplets enclosed by dotted red lines on panels (A) and (C) are shown at higher magnification in panels (B) and (D). (A,B) First printing cycle, (C,D) tenth printing cycle. The lengths of the scale bars correspond to (A,C) 100 µm and (B,D) 50 µm.
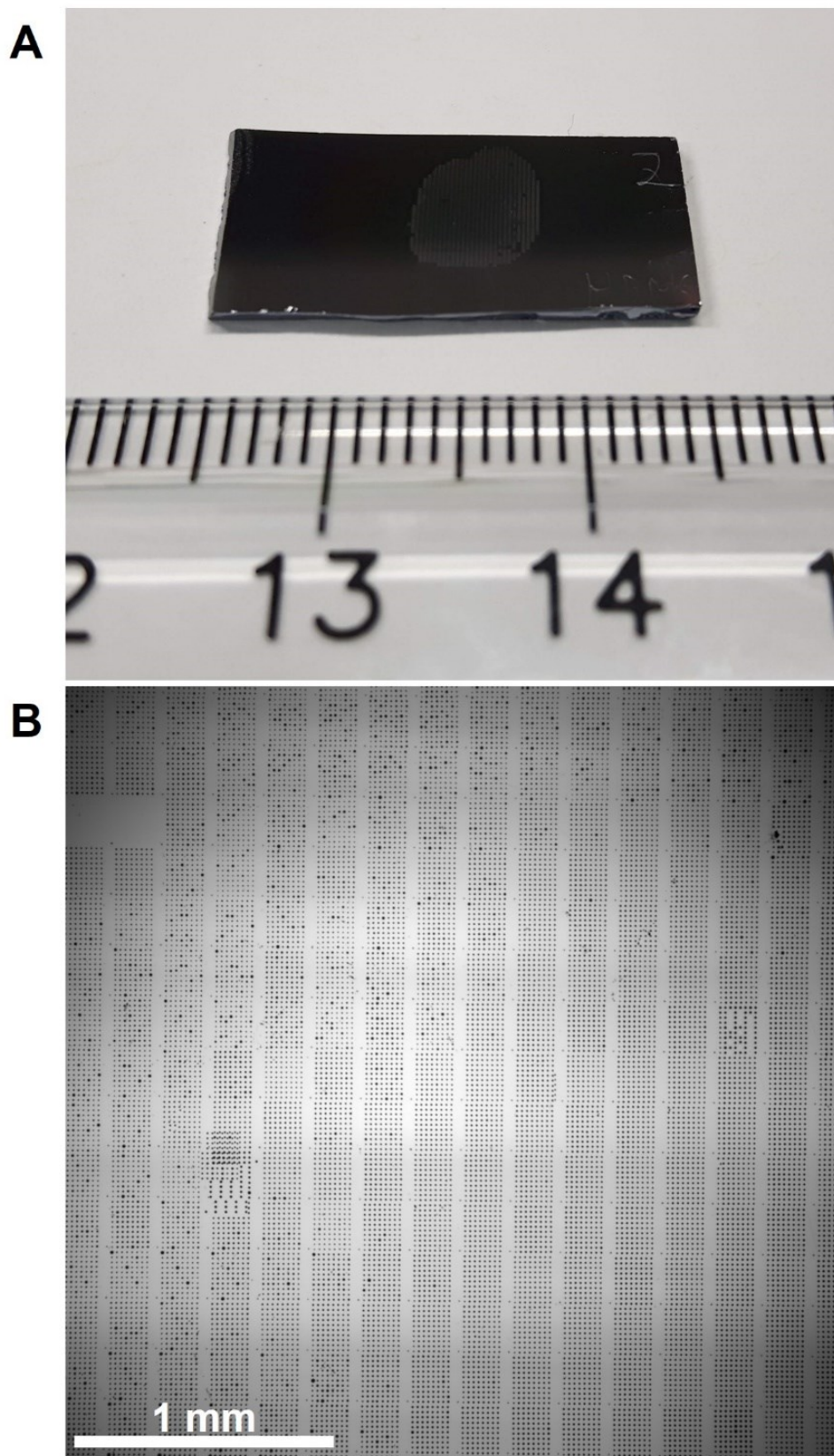
Figure 5.6. Large area views of of poly(1-decene) microdroplet arrays produced on the first stamped HDMS-Si substrate. (A) Photograph image and (B) optical microscopy image.

With the computer-aided control of the movement of the dispensing elements, complex and arbitrary structures can be easily produced. As exemplary, arbitrary patterns, the logo of "INT & UOS" composed of microdroplets with an average diameter of 7.55 ± 0.94 µm (dwell time: 10 s) was stamped (Figure 5.7).
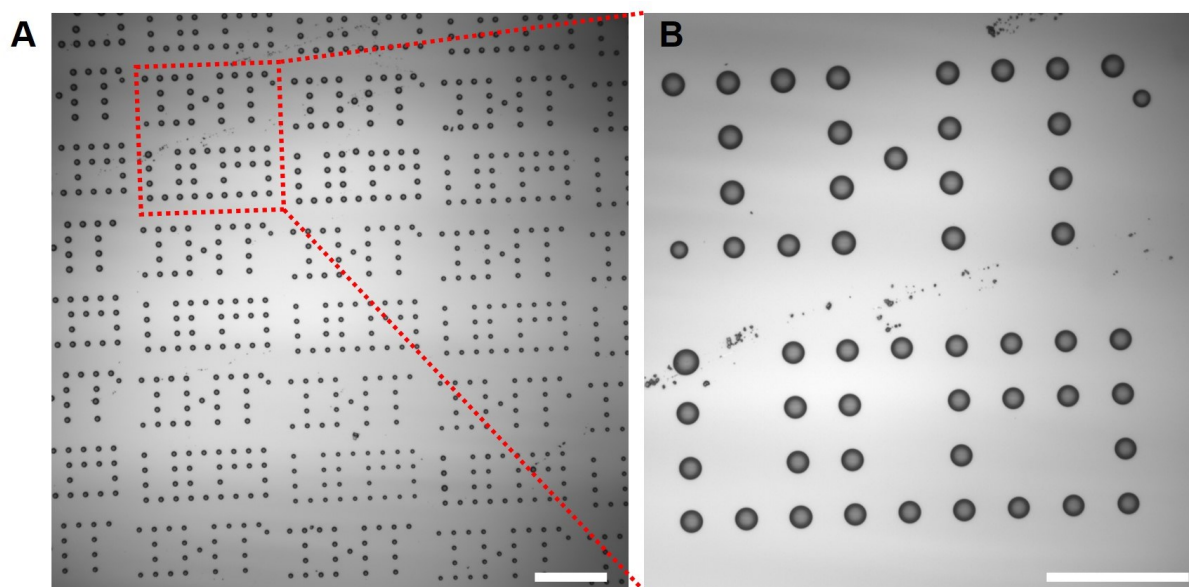
Figure 5.7. Optical microscopy images of arbitrary patterns consisting of poly(1-decene) microdroplets stamped on a HMDS-Si substrate with a dwell time of 10 s. The logo "INT & UOS" was generated within one 8 × 10 matrix of microdroplets generated with a single dispensing element by deliberate omission of selected matrix points. The average droplet size is 7.55 ± 0.94 µm. The lengths of the scale bars correspond to (A) 100 µm and (B) 50 µm.

5.3.3. Adjusting sizes of the stamped microdroplets by surface wettability and dwell time

Like most contact stamping strategies, ink transport during capillary stamping depends on dwell time and the wettability of the substrate [78]. Figure 5.8A and Figure 5.8B show SCS conducted on HMDS-Si with different dwell times. Each matrix of poly(1-decene) microdroplets generated by 32 successive contacts between a specific dispensing element and HMDS-Si contains 4 × 8 microdroplets. The dwell time was varied for every column of drops from 1 s to 5 s to 10 s to 20 s. The average diameters of the microdroplets were 4.0 ± 0.6 µm, 4.5 ± 0.4 µm, 5.9 ± 0.8 µm, and 6.4 ± 0.7 µm. Figure 5.8C and Figure 5.8D show SCS conducted on a Si

wafer modified with (3-aminopropyl)triethoxysilane (APTES) thereafter referred to APTES-Si. The contact angle of the ink/poly(1-decene) is ~0° Again, each matrix also contains 4 × 8 poly(1-decene) microdroplets, and every column of microdroplets was produced with different dwell time 1 s, 5 s, 10 s, and 20 s. For a dwell time of 1 s, the diameter of the stamped microdroplets amounted to 16.9 ± 0.6 μm. With the increase of the dwell time, the stamped microdroplets started to impinge on each other, thus forming a liquid threads.
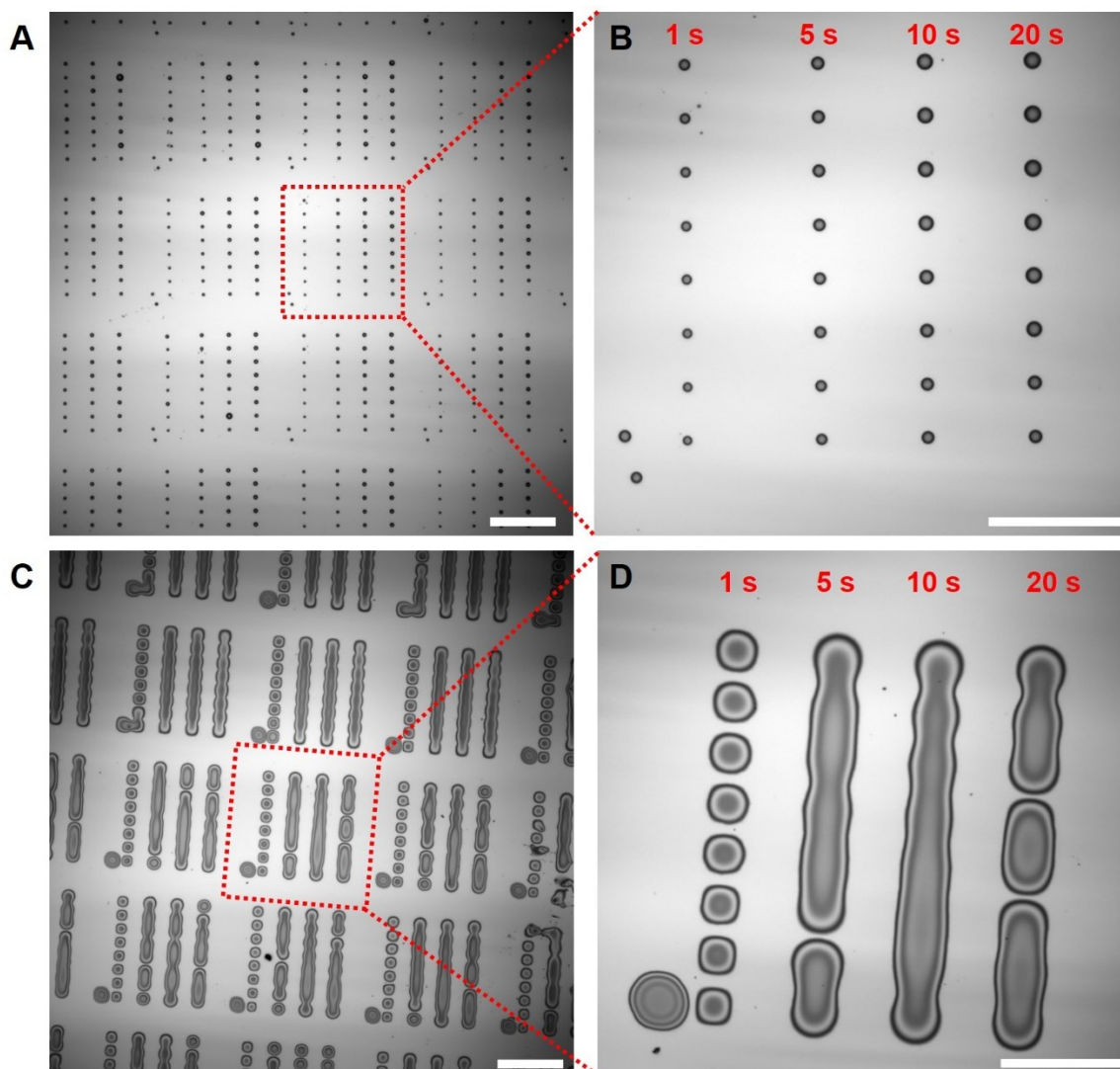
Figure 5.8. Optical microscopy images displaying the influence of surface wettability and dwell time on the size of stamped poly(1-decene) microdroplets. (A,B) 4 × 8 microdroplets within each matrix were stamped by one dispensing element onto HMDS-Si (the contact angle of the ink/poly(1-decene) is 49.6° ± 2.3°). Within each matrix, every column of microdroplets was formed with different dwell times of 1 s, 5 s, 10 s, and 20 s. (C,D) 4 × 8 microdroplets within each matrix were stamped by one dispensing element onto APTES-Si (the contact angle of the ink/poly(1-decene) is ~0°)Within each matrix, every column of microdroplets was formed with different dwell times of 1 s, 5 s, 10 s, and 20 s. The lengths of the scale bars correspond to (A,C) 100 μm and (B,D) 50 μm.

5.3.4. Multi-ink SCS

Multi-ink patterning or multiplexing has been desired since the beginning of soft lithography [126,127]. Hirtz and coworkers developed general procedure for multi-ink stamping based on polymer pen lithography [124,125]. Here, as proof-of-concept, the multi-ink stamping potential of SCS was described. For this purpose, lipid I (ink I) and lipid II (ink II) in poly(1-decene) with a concentration of 0.1 mg/ml were used as inks (section 5.2.1.5). And HMDS-Si was used as the substrate. We used 2 mm thick custom-made stamp-holders extending 30 mm × 80 mm that contained two holes extending 5 mm × 10 mm (Figure 5.9A). The CPG surfaces of SCS stamps were glued onto the stamp-holders as described above (Figure 5.9B). SCS stamps were then cut into two separate parts (part I and part II, each part has dispensing element arrays of ∼0.5 cm × 0.4 cm in size) with a sharp knife in such a way that each part covered one of the holes in the stamp-holders (Figure 5.9C and Figure 5.10B). Lipids are amphipathic molecules that will form micelles in a selective solvent, making them difficult, if not impossible, to penetrate SCS stamps. Therefore, 20 μL portions of inks I and II were deposited directly onto the surfaces of the pyramid-shaped dispensing elements of parts I and II of the SCS stamps using an Eppendoff pipette (Figure 5.10C). After a wait time of 1 h, stamp-holders were mounted onto the NLP 2000 device. Then, 100 μL poly(1-decene) was deposited onto each part of the SCS stamp through the two holes in the stamp-holders (Figure 5.10D). After a wait time of 2 h, the ink-soaked SCS stamp was fully transparent (Figure 5.9D). For leveling SCS stamps for multi-ink stamping, a similar method was used as for the single-ink stamping described above, but only one of the two separated parts was leveled assuming conformity of the other part. Small misalignments were still expected after the leveling. After leveling, multi-ink microdroplet patterns were stamped by repositioning the piezo-driven substrate stage in such a sequence that sub-patterns of each particular ink were generated next to each other (Figure 5.10E,F). The initial offset between parts I and II of the SCS stamp was corrected by visual *in situ* alignment using an optical microscope attached to the NLP 2000 device. Because lipid inks were deposited directly onto surfaces of the pyramid-shaped dispensing elements of parts I and

II of the SCS stamp, there was still extra ink solutions on the surfaces of the pyramid-shaped dispensing element tips of parts I and II of the SCS stamps even after a wait time of 1 h, which increased the volume of the stamped microdroplets with relative large as well as heterogeneous sizes as shown in Figure 5.10G and Figure 5.10H.
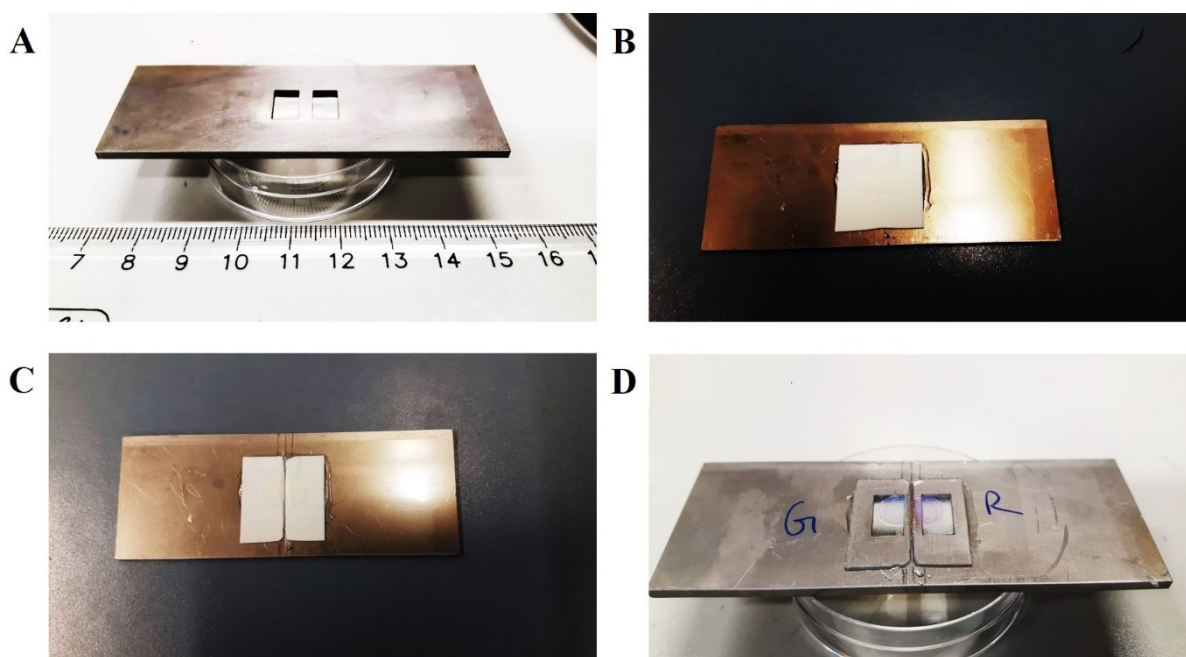
Figure 5.9. Photographs of custom-made stamp-holder, stamp cutting, and stamp inking. (A) Custom made stamp-holder with two separate square holes for multi-ink stamping. (B) The stamp glued to the stamp-holder. (C) The stamp was then separated into part I and part II with a sharp knife. (D) 20 µL of inks I and II were deposited directly onto the surfaces of the pyramid-shaped dispensing elements of parts I and II of the SCS stamp using an Eppendoff pipette. After a wait time of 1 h, 100 µL poly(1-decene) was deposited onto each part of the SCS stamp through the two holes in the stamp-holders and the stamp became transparent after 2 h wait time.
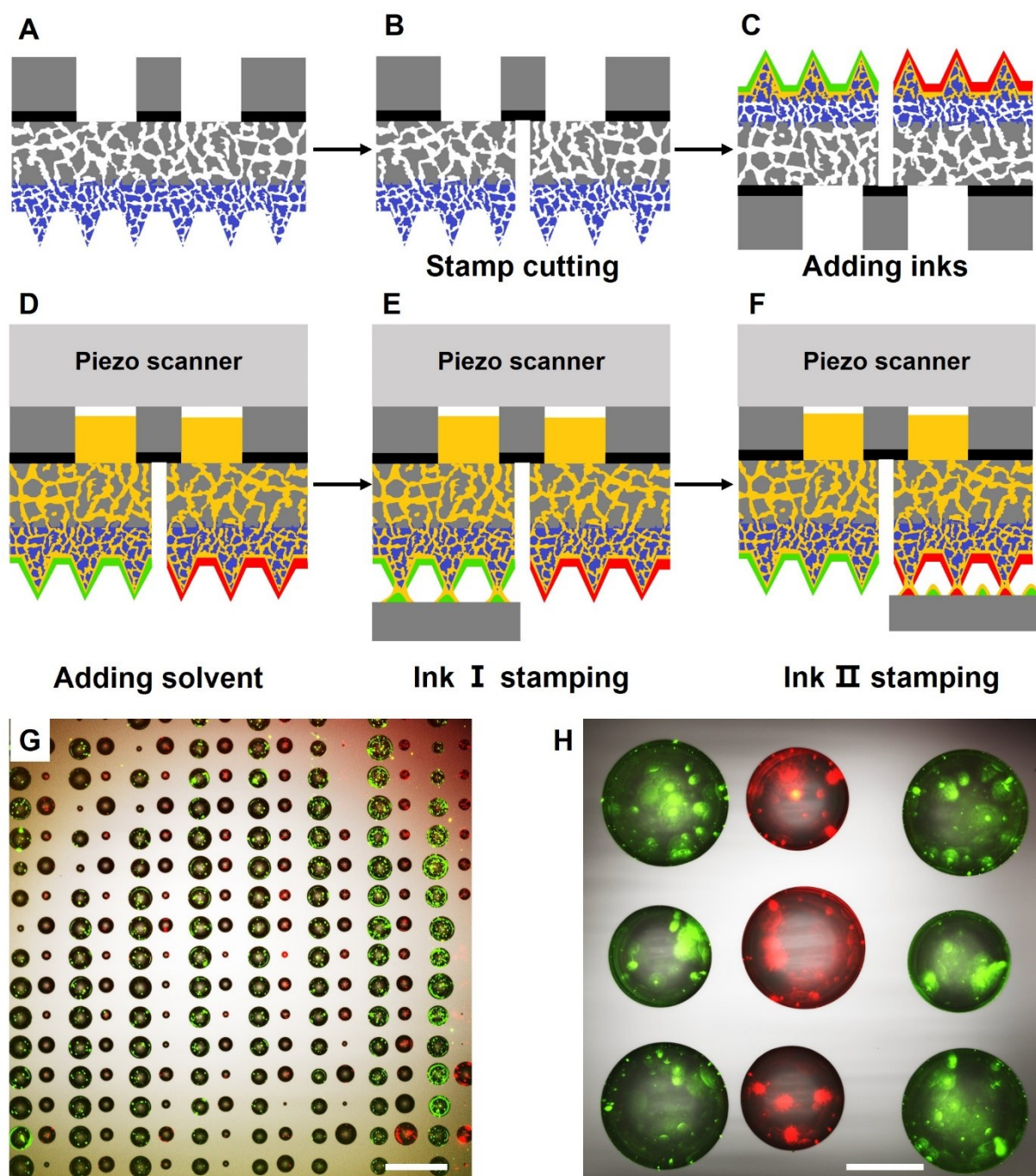
Figure 5.10. Multi-ink SCS. (A)–(F) Schematic illustration of multi-ink SCS (A) The SCS stamp was glued onto a custom-made stamp-holder having two separate holes. (B) The SCS stamp was separated into two parts with a sharp knife. (C) Inks I and II were dropped onto the surfaces of the two separated SCS stamps . (D) Poly(1-decene) was deposited into the two holes of the custom-made stamp-holder. (E) Stamping of ink I. (F) The substrate was displaced and and ink II was stamped.   (G), (H) Superimposed optical and fluorescence microscopy images of stamped microdroplets of inks I and II. The lengths of the scale bars correspond to (G) 200 μm, and (H) 50 μm.

5.4. Conclusion

In conclusion, this Chapter reports the main achievement of the present thesis, scanner-based capillary stamping or SCS, a technique combining the advantages of parallel stamping approaches and continuous ink supply to achieve high-throughput, low-cost, and digitized generation of large-area microdroplet arrays. By computer-controlled displacement of the SCS stamps, complex and arbitrary structures can be produced. Sizes of the stamped microdroplets can be controlled by adjusting both the surface wettability and the dwell time of the contact. In addtition, the ability of SCS technique for multi-ink stamping was also demonstrated. Above all, SCS will be an important member of the big family of the contact-lithographic methods.

6. Summary and outlook

This PhD thesis describes the development of a contact-lithographic patterning technique, named as scanner-based capillary stamping (SCS), which combines parallel stamping of large areas with porous stamps enabling continuous ink supply. On the way to develop SCS method, two unexpected incidental techniques have been established: (i) One is the immobilization of water droplets on hydrophobic surfaces by contact line pinning at non-lithographically generated polymer microfiber rings, discovered in the course of the stamp design and fabrication using replication molding of PS-*b*-P2VP against hydrophobized macroporous silicon molds. PS-*b*-P2VP fiber rings remain on the hydrophobized macroporous silicon molds after swelling-induced pore formation and detachment of the PS-*b*-P2VP stamps. The PS-*b*-P2VP fiber allow immobilization of water drops on the hydrophobically modified surface of the macroporous silicon molds. Water drops immobilized by these rings can be prevented from dewetting within the PS-*b*-P2VP fiber rings. (ii) The second one is the lithographic deposition of nanostructured submicron BCP dots by sacrificial stamping, as revealed by preliminary SCS experiments with non-inked nanoporous PS-*b*-P2VP stamps. Parts of the stamps' contact elements can be lithographically transferred to a counterpart surface.

In this thesis, the SCS technique has been successfully established, which combines parallel stamping of large areas with continuous ink supply. Large-area arrays of non-volatile ink microdroplets were generated on substrates in a parallel stamping approach. However, with computer-aided control of the displacement of the stamp dispensing elements complex and arbitrary structures can be easily produced so that SCS combined features of parallel and serial patterning methods. The size of the stamped microdroplets can be controlled by adjusting both the surface wettability of the substrate and the stamp-substrate contact time. Moreover, multi-ink SCS has been proved to be realizable.

SCS is a platform that can be extended by the fabrication of nanoporous stamps consisting of

other materials than polymers including inorganic materials and metals, by developing new stamping modes such as high-temperature SCS, organic solution SCS, and micro-3D stamping. SCS may pave the way for the development of new contact-lithographic surface patterning techniques that feature parallel stamping of large areas with continuous ink supply.

Bibliography

1.   Xia, Y. and G.M. Whitesides, *Soft lithography.* Annual Review of Materials Science, 1998. **28**, 153-184.

2.   Qin, D., Y. Xia, and G.M. Whitesides, *Soft lithography for micro-and nanoscale patterning.* Nature Protocols, 2010. **5**, 491-502.

3.   Perl, A., D.N. Reinhoudt, and J. Huskens, *Microcontact printing: limitations and achievements.* Advanced Materials, 2009. **21**, 2257-2268.

4.   Kaufmann, T. and B.J. Ravoo, *Stamps, inks and substrates: polymers in microcontact printing.* Polymer Chemistry, 2010. **1**, 371-387.

5.   Huo, F., et al., *Polymer pen lithography.* Science, 2008. **321**, 1658-1660.

6.   Braunschweig, A.B., F. Huo, and C.A. Mirkin, *Molecular printing.* Nature Chemistry, 2009. **1**, 353-358.

7.   Carbonell, C. and A.B. Braunschweig, *Toward 4D nanoprinting with tip-induced organic surface reactions.* Accounts of Chemical Research, 2016. **50**, 190-198.

8.   Piner, R.D., et al., *"Dip-pen" nanolithography.* Sscience, 1999. **283**, 661-663.

9.   Liu, G., et al., *Development of Dip-Pen Nanolithography (DPN) and Its Derivatives.* Small, 2019. **15**, 1900564.

10.   Rodolfa, K.T., et al., *Nanoscale pipetting for controlled chemistry in small arrayed water droplets using a double-barrel pipet.* Nano Letters, 2006. **6**, 252-257.

11.   Fang, A., E. Dujardin, and T. Ondarçuhu, *Control of droplet size in liquid nanodispensing.* Nano Letters, 2006. **6**, 2368-2374.

12.   Kim, K.-H., et al., *A Novel AFM Chip for Fountain Pen Nanolithography-Design and Microfabrication.* Materials Research Society Symposium Proceedings, 2003. **782**, A5.56.1.

13.   Meister, A., et al., *FluidFM: combining atomic force microscopy and nanofluidics in a universal liquid delivery system for single cell applications and beyond.* Nano Letters, 2009. **9**, 2501-2507.

14.   Lewis, A., et al., *Fountain pen nanochemistry: Atomic force control of chrome etching.* Applied Physics Letters, 1999. **75**, 2689-2691.

15.   Chen, C.-C., Y. Zhou, and L.A. Baker, *Scanning ion conductance microscopy.* Annual Review of Analytical Chemistry, 2012. **5**, 207-228.

16.   Leichle, T., et al., *A microcantilever-based picoliter droplet dispenser with integrated force sensors and electroassisted deposition means.* Journal of Microelectromechanical Systems, 2008. **17**, 1239-1253.

17.   Xu, T., et al., *Block copolymer surface reconstuction: A reversible route to nanoporous films.* Advanced Functional Materials, 2003. **13**, 698-702.

18.   Xue, L., et al., *Humidity-enhanced wet adhesion on insect-inspired fibrillar adhesive pads.* Nature Communications, 2015. **6**, 6621-6629.

19.   Wang, Y., U. Gö̈sele, and M. Steinhart, *Mesoporous block copolymer nanorods by swelling-induced morphology reconstruction.* Nano Letters, 2008. **8**, 3548-3553.

20.   Wang, Y. and F. Li, *An Emerging Pore-Making Strategy: Confined Swelling-Induced Pore Generation in Block Copolymer Materials.* Advanced Materials, 2011. **23**, 2134-2148.

21. Wang, Y., et al., *Nanoscopic morphologies in block copolymer nanorods as templates for atomic-layer deposition of semiconductors.* Advanced Materials, 2009. **21**, 2763-2766.

22. Wang, Y., L. Tong, and M. Steinhart, *Swelling-induced morphology reconstruction in block copolymer nanorods: Kinetics and impact of surface tension during solvent evaporation.* ACS Nano, 2011. **5,** 1928-1938.

23. Wang, Y., et al., *Nanoporous Metal Membranes with Bicontinuous Morphology from Recyclable Block-Copolymer Templates.* Advanced Materials, 2010. **22**, 2068-2072.

24. Xue, L., et al., *Reversible adhesion switching of porous fibrillar adhesive pads by humidity.* Nano Letters, 2013. **13**, 5541-5548.

25. Xue, L., et al., *Humidity-enhanced wet adhesion on insect-inspired fibrillar adhesive pads.* Nature Communications, 2015. **6**, 6621-6629.

26. Xue, L., et al., *Advanced SERS Sensor Based on Capillarity-Assisted Preconcentration through Gold Nanoparticle-Decorated Porous Nanorods.* Small, 2017. **13**, 1603947.

27. Ueda, E., et al., *DropletMicroarray: facile formation of arrays of microdroplets and hydrogel micropads for cell screening applications.* Lab on a Chip, 2012. **12**, 5218-5224.

28. Huebner, A., et al., *Static microdroplet arrays: a microfluidic device for droplet trapping, incubation and release for enzymatic and cell-based assays.* Lab on a Chip, 2009. **9**, 692-698.

29. Mugherli, L., et al., *In Situ Assembly and Screening of Enzyme Inhibitors with Surface-Tension Microarrays.* Angewandte Chemie International Edition, 2009. **48**, 7639-7644.

30. Burchak, O.N., et al., *Combinatorial discovery of fluorescent pharmacophores by multicomponent reactions in droplet arrays.* Journal of the American Chemical Society, 2011. **133**, 10058-10061.

31. Tronser, T., et al., *Droplet Microarray Based on Patterned Superhydrophobic Surfaces Prevents Stem Cell Differentiation and Enables High-Throughput Stem Cell Screening.* Advanced Healthcare Materials, 2017. **6**, 1700622.

32. Popova, A.A., et al., *Fish-Microarray: A Miniaturized Platform for Single-Embryo High-Throughput Screenings.* Advanced Functional Materials, 2018. **28**, 1703486.

33. Efremov, A.N., et al., *Micropatterned superhydrophobic structures for the simultaneous culture of multiple cell types and the study of cell–cell communication.* Biomaterials, 2013. **34**, 1757-1763.

34. Neto, A.I., et al., *Fabrication of Hydrogel Particles of Defined Shapes Using Superhydrophobic-Hydrophilic Micropatterns.* Advanced Materials, 2016. **28**, 7613-7619.

35. Tsotsalas, M., et al., *Freestanding MOF microsheets with defined size and geometry using superhydrophobic–superhydrophilic arrays.* Advanced Materials Interfaces, 2016. **3**, 1500392.

36. Butler, J.H., et al., *In situ synthesis of oligonucleotide arrays by using surface tension.* Journal of the American Chemical Society, 2001. **123**, 8887-8894.

37. Zhang, G., et al., *Binary DNA arrays on heterogeneous patterned surfaces.* Langmuir, 2003. **19**, 9850-9854.

38. Lee, Y.Y., et al., *Elucidating drug resistance properties in scarce cancer stem cells using droplet microarray.* Nano Today, 2012. **7**, 29-34.

39. Mandsberg, N.K. and R. Taboryski, *Spatial control of condensation on chemically homogeneous pillar-built surfaces.* Langmuir, 2017. **33**, 5197-5203.

40. Yen, T.M., et al., *Self-Assembled Pico-Liter Droplet Microarray for Ultrasensitive Nucleic Acid Quantification.* ACS Nano, 2015. **9**, 10655-10663.

41. Yu, H., et al., *Large scale flow-mediated formation and potential applications of surface*

nanodroplets. ACS Applied Materials & Interfaces, 2016. **8**, 22679-22687.

42. Bao, L., et al., *Highly ordered arrays of femtoliter surface droplets.* Small, 2015. **11**, 4850-4855.

43. Peng, S., et al., *Morphological transformation of surface femtodroplets upon dissolution.* the Journal of Physical Chemistry Letters, 2017. **8**, 584-590.

44. Wu, L., et al., *Printing patterned fine 3D structures by manipulating the three phase contact line.* Advanced Functional Materials, 2015. **25**, 2237-2242.

45. Arrabito, G. and B. Pignataro, *Solution processed micro-and nano-bioarrays for multiplexed biosensing.* Analytical Chemistry, 2012. **84**, 5450-5462.

46. Huang, J.Y., et al., *Multifunctional superamphiphobic TiO2 nanostructure surfaces with facile wettability and adhesion engineering.* Small, 2014. **10**, 4865-4873.

47. Pelkmans, L., et al., *Genome-wide analysis of human kinases in clathrin-and caveolae/raft-mediated endocytosis.* Nature, 2005. **436**, 78-86.

48. Kittler, R., et al., *An endoribonuclease-prepared siRNA screen in human cells identifies genes essential for cell division.* Nature, 2004. **432**, 1036-1040.

49. Jackman, R.J., et al., *Fabricating large arrays of microwells with arbitrary dimensions and filling them using discontinuous dewetting.* Analytical Chemistry, 1998. **70**, 2280-2287.

50. Thalladi, V.R. and G.M. Whitesides, *Crystals of crystals: fabrication of encapsulated and ordered two-dimensional arrays of microcrystals.* Journal of the American Chemical Society, 2002. **124**, 3520-3521.

51. Biebuyck, H.A. and G.M. Whitesides, *Self-organization of organic liquids on patterned self-assembled monolayers of alkanethiolates on gold.* Langmuir, 1994. **10**, 2790-2793.

52. Zahner, D., et al., *A Facile Approach to Superhydrophilic–Superhydrophobic Patterns in Porous Polymer Films.* Advanced Materials, 2011. **23**, 3030-3034.

53. Geyer, F.L., et al., *Superhydrophobic–Superhydrophilic Micropatterning: Towards Genome-on-a-Chip Cell Microarrays.* Angewandte Chemie International Edition, 2011. **50**, 8424-8427.

54. Li, J.S., et al., *Printable superhydrophilic–superhydrophobic micropatterns based on supported lipid layers.* Langmuir, 2012. **28**, 8286-8291.

55. Hirtz, M., et al., *Porous polymer coatings as substrates for the formation of high-fidelity micropatterns by quill-like pens.* Beilstein Journal of Nanotechnology, 2013. **4**, 377-384.

56. Auad, P., E. Ueda, and P.A. Levkin, *Facile and multiple replication of superhydrophilic–superhydrophobic patterns using adhesive tape.* ACS Applied Materials & Interfaces, 2013. **5**, 8053-8057.

57. Ueda, E. and P.A. Levkin, *Micropatterning Hydrophobic Liquid on a Porous Polymer Surface for Long-Term Selective Cell-Repellency.* Advanced Healthcare Materials, 2013. **2**, 1425-1429.

58. Efremov, A.N., M. Grunze, and P.A. Levkin, *Digital liquid patterning: a versatile method for maskless generation of liquid patterns and gradients.* Advanced Materials Interfaces, 2014. **1**, 1300075.

59. Feng, W., et al., *Surface Patterning via Thiol-Yne Click Chemistry: An Extremely Fast and Versatile Approach to Superhydrophilic-Superhydrophobic Micropatterns.* Advanced Materials Interfaces, 2014. **1**, 1400269.

60. Popova, A.A., et al., *Facile One Step Formation and Screening of Tumor Spheroids Using Droplet-Microarray Platform.* Small, 2019. **15**, 1901299.

61. Ueda, E. and P.A. Levkin, *Emerging Applications of Superhydrophilic-Superhydrophobic Micropatterns.* Advanced Materials, 2013. **25**, 1234-1247.

62.   Kim, Y.-K., G.T. Kim, and J.S. Ha, *Simple Patterning via Adhesion between a Buffered-Oxide Etchant-Treated PDMS Stamp and a SiO2 Substrate.* Advanced Functional Materials, 2007. **17**, 2125-2132.

63.   Wang, J., et al., *Surface treatment-assisted switchable transfer printing on polydimethylsiloxane films.* Journal of Materials Chemistry C, 2016. **4**, 3467-3476.

64.   Ghatkesar, M.K., et al., *Scanning probe microscope-based fluid dispensing.* Micromachines, 2014. **5**, 954-1001.

65.   Le, H.P., *Progress and Trends in Ink-jet Printing Technology.* Journal of Imaging Science and Technology, 1998. **42**, 49-62.

66.   Cummins, G., *Inkjet printing of conductive materials: a review.* Circuit World, 2012. **38**, 193-213.

67.   Onses, M.S., et al., *Mechanisms, Capabilities, and Applications of High-Resolution Electrohydrodynamic Jet Printing.* Small, 2015. **11**, 4237-4266.

68.   Taylor, G.I., *Electrically driven jets.* Proceedings of the Royal Society of London. A. Mathematical and Physical Sciences, 1969. **313**, 453-475.

69.   Taylor, G.I., *Disintegration of water drops in an electric field.* Proceedings of the Royal Society of London. Series A. Mathematical and Physical Sciences, 1964. **280**, 383-397.

70.   Park, J.-U., et al., *High-resolution electrohydrodynamic jet printing.* Nature Materials, 2007. **6**, 782-789.

71.   Park, J.-U., et al., *Nanoscale patterns of oligonucleotides formed by electrohydrodynamic jet printing with applications in biosensing and nanomaterials assembly.* Nano Letters, 2008. **8**, 4210-4216.

72.   Collins, R.T., et al., *Electrohydrodynamic tip streaming and emission of charged drops from liquid cones.* Nature Physics, 2007. **4**, 149-154.

73.   Ferraro, P., et al., *Dispensing nano–pico droplets and liquid patterning by pyroelectrodynamic shooting.* Nature Nanotechnology, 2010. **5**, 429-435.

74.   Foresti, D., et al., *Acoustophoretic printing.* Science Advances, 2018. **4**, eaat1659.

75.   Jaschke, M. and H.-J. Butt, *Deposition of organic material by the tip of a scanning force microscope.* Langmuir, 1995. **11**, 1061-1064.

76.   Ginger, D.S., H. Zhang, and C.A. Mirkin, *The Evolution of Dip-Pen Nanolithography.* Angewandte Chemie International Edition, 2004. **43**, 30-45.

77.   Hong, S., J. Zhu, and C.A. Mirkin, *Multiple ink nanolithography: toward a multiple-pen nano-plotter.* Science, 1999. **286**, 523-525.

78.   Hong, S. and C.A. Mirkin, *A nanoplotter with both parallel and serial writing capabilities.* Science, 2000. **288**, 1808-1811.

79.   Zheng, Z., et al., *Multiplexed Protein Arrays Enabled by Polymer Pen Lithography: Addressing the Inking Challenge.* Angewandte Chemie International Edition, 2009. **48**, 7626-7629.

80.   Hu, J. and M.-F. Yu, *Meniscus-confined three-dimensional electrodeposition for direct writing of wire bonds.* Science, 2010. **329**, 313-316.

81.   Kim, K.-H., N. Moldovan, and H.D. Espinosa, *A Nanofountain Probe with Sub-100nm Molecular Writing Resolution.* Small, 2005. **1**, 632-635.

82.   Lehmann, V. and H. Föll, *Formation mechanism and properties of electrochemically etched trenches in n-type silicon.* Journal of the Electrochemical Society, 1990. **137**, 653-659.

83.   Birner, A., et al., *Macroporous Silicon: A Two-Dimensional Photonic Bandgap Material Suitable for*

the Near-Infrared Spectral Range. Physica Status Solidi (a), 1998. **165**, 111-117.

84. Wang, Y., *Nondestructive creation of ordered nanopores by selective swelling of block copolymers: toward homoporous membranes.* Accounts of Chemical Research, 2016. **49**, 1401-1408.

85. Eichler-Volf, A., et al., *The influence of surface topography and surface chemistry on the anti-adhesive performance of nanoporous monoliths.* ACS Applied Materials & Interfaces, 2016. **8**, 22593-22604.

86. Fadeev, A.Y. and T.J. McCarthy, *Self-assembly is not the only reaction possible between alkyltrichlorosilanes and surfaces: monomolecular and oligomeric covalently attached layers of dichloro-and trichloroalkylsilanes on silicon.* Langmuir, 2000. **16**, 7268-7274.

87. Hou, P., et al., *Nanostructured Submicron Block Copolymer Dots by Sacrificial Stamping: A Potential Preconcentration Platform for Locally Resolved Sensing, Chemistry, and Cellular Interactions.* ACS Applied Nano Materials, 2018. **1**, 1413-1419.

88. Quéré, D., *Wetting and roughness.* Annual Review of Materials Research, 2008. **38**, 71-99.

89. MacGregor-Ramiasa, M.N. and K. Vasilev, *Questions and Answers on the Wettability of Nano-Engineered Surfaces.* Advanced Materials Interfaces, 2017. **4**, 1700381.

90. Extrand, C.W., *Origins of wetting.* Langmuir, 2016. **32**, 7697-7706.

91. Nie, Z. and E. Kumacheva, *Patterning surfaces with functional polymers.* Nature Materials, 2008. **7**, 277-290.

92. Traub, M.C., W. Longsine, and V.N. Truskett, *Advances in nanoimprint lithography.* Annual Review of Chemical and Biomolecular Engineering, 2016. **7**, 583-604.

93. Guo, L.J., *Nanoimprint lithography: methods and material requirements.* Advanced Materials, 2007. **19**, 495-513.

94. Suh, K.Y., M.C. Park, and P. Kim, *Capillary force lithography: a versatile tool for structured biomaterials interface towards cell and tissue engineering.* Advanced Functional Materials, 2009. **19**, 2699-2712.

95. Ho, D., et al., *Capillary force lithography: the versatility of this facile approach in developing nanoscale applications.* Nanoscale, 2015. **7**, 401-414.

96. Cavallini, M., C. Albonetti, and F. Biscarini, *Nanopatterning soluble multifunctional materials by unconventional wet lithography.* Advanced Materials, 2009. **21**, 1043-1053.

97. Simeone, F.C., C. Albonetti, and M. Cavallini, *Progress in micro-and nanopatterning via electrochemical lithography.* The Journal of Physical Chemistry C, 2009. **113**, 18987-18994.

98. Lee, B.H., H. Shin, and M.M. Sung, *Patterning a two-dimensional colloidal crystal by water-mediated particle transfer printing.* Chemistry of Materials, 2007. **19**, 5553-5556.

99. Cucinotta, F., et al., *Microcontact transfer printing of zeolite monolayers.* Advanced Materials, 2009. **21**, 1142-1145.

100. Kehr, N.S., et al., *Cell Adhesion and Cellular Patterning on a Self-Assembled Monolayer of Zeolite L Crystals.* Advanced Functional Materials, 2010. **20**, 2248-2254.

101. Wang, Y., et al., *Orienting zeolite L microcrystals with a functional linker.* Angewandte Chemie International Edition, 2010. **49**, 1434-1438.

102. Yoon, K.B., *Organization of zeolite microcrystals for production of functional materials.* Accounts of Chemical Research, 2007. **40**, 29-40.

103. Zabala Ruiz, A., H. Li, and G. Calzaferri, *Organizing supramolecular functional dye–zeolite crystals.* Angewandte Chemie International Edition, 2006. **45**, 5282-5287.

104.   Lee, J., et al., *Ultrasound-Aided Remarkably Fast Assembly of Monolayers of Zeolite Crystals on Glass with a Very High Degree of Lateral Close Packing.* Advanced Materials, 2005. **17**, 837-841.

105.   Wang, S. and J. Zhao, *First-order conformation transition of single poly (2-vinylpyridine) molecules in aqueous solutions.* 2007, The Journal of Chemical Physics. 2007. **126**, 091104.

106.   Bang, J., et al., *Block copolymer nanolithography: translation of molecular level control to nanoscale patterns.* Advanced Materials, 2009. **21**, 4769-4792.

107.   Deng, R., et al., *Mesoporous block copolymer nanoparticles with tailored structures by hydrogen-bonding-assisted self-assembly.* Advanced Materials, 2012. **24**, 1889-1893.

108.   Jin, Z. and H. Fan, *Self-assembly of nanostructured block copolymer nanoparticles.* Soft Matter, 2014. **10**, 9212-9219.

109.   Fan, H. and Z. Jin, *Selective swelling of block copolymer nanoparticles: size, nanostructure, and composition.* Macromolecules, 2014. **47**, 2674-2681.

110.   Masuda, H., K. Yada, and A. Osaka, *Self-ordering of cell configuration of anodic porous alumina with large-size pores in phosphoric acid solution.* Japanese Journal of Applied Physics, 1998. **37**, L1340.

111.   Xie, W., et al., *Synthesis of gold nanopeanuts by citrate reduction of gold chloride on gold–silver core–shell nanoparticles.* Chemical Communications, 2009. 5263-5265.

112.   Xue, L., et al., *Advanced SERS Sensor Based on Capillarity-Assisted Preconcentration through Gold Nanoparticle-Decorated Porous Nanorods.* Small, 2017. **13**, 1603947.

113.   Roth, C.B., et al., *Eliminating the enhanced mobility at the free surface of polystyrene: fluorescence studies of the glass transition temperature in thin bilayer films of immiscible polymers.* Macromolecules, 2007. **40**, 2568-2574.

114.   Gurmessa, B. and A.B. Croll, *Influence of thin film confinement on surface plasticity in polystyrene and poly (2-vinylpyridine) homopolymer and block copolymer films.* Macromolecules, 2015. **48**, 5670-5676.

115.   Lee, J.-Y. and A.J. Crosby, *Crazing in glassy block copolymer thin films.* Macromolecules, 2005. **38**, 9711-9717.

116.   Fetters, L.J., et al., *Packing length influence in linear polymer melts on the entanglement, critical, and reptation molecular weights.* Macromolecules, 1999. **32**, 6847-6851.

117.   Brown, H.R. and T.P. Russell, *Entanglements at polymer surfaces and interfaces.* Macromolecules, 1996. **29**, 798-800.

118.   Si, L., et al., *Chain entanglement in thin freestanding polymer films.* Physical Review letters, 2005. **94**, 127801.

119.   Meister, A., et al., *Nanodispenser for attoliter volume deposition using atomic force microscopy probes modified by focused-ion-beam milling.* Applied Physics Letters, 2004. **85**, 6260-6262.

120.   Deladi, S., et al., *Fabrication of micromachined fountain pen with in situ characterization possibility of nanoscale surface modification.* Journal of Micromechanics and Microengineering, 2004. **15**, 528-534.

121.   Kim, K.H., N. Moldovan, and H.D. Espinosa, *A nanofountain probe with sub-100 nm molecular writing resolution.* Small, 2005. **1**, 632-635.

122.   Enke, D., F. Janowski, and W. Schwieger, *Porous glasses in the 21st century—a short review.* Microporous and Mesoporous Materials, 2003. **60**, 19-30.

123.   Kumar, R., et al., *Click-Chemistry Based Allergen Arrays Generated by Polymer Pen Lithography for*

Mast Cell Activation Studies. Small, 2016. **12**, 5330-5338.

124. Kumar, R., et al., *Multi-color polymer pen lithography for oligonucleotide arrays.* Chemical Communications, 2016. **52**, 12310-12313.

125. Brinkmann, F., et al., *Interdigitated multicolored bioink micropatterns by multiplexed polymer pen lithography.* Small, 2013. **9**, 3266-3275.

126. Bano, F., et al., *Toward multiprotein nanoarrays using nanografting and DNA directed immobilization of proteins.* Nano Letters, 2009. **9**, 2614-2618.

127. Barbulovic-Nad, I., et al., *Bio-microarray fabrication techniques—a review.* Critical Reviews in Biotechnology, 2006. **26**, 237-259.

Acknowledgments

First of all, I would like to thank my supervisor Prof. Dr. Martin Steinhart, who provided me an opportunity to join the program ERC-CoG-2014, project 646742 INCANA. Without his instructions, advices and revisions, this PhD thesis would not have been finished. I also appreciate the freedom and space he has given to me.

Besides my supervisor, I would like to thank PD Dr. Dr. Michael Hirtz and Dr. Ravi Kumar for their hospitality. Dr. Hirtz gave me access to the laboratories and research facilities at the Institute of Nanotechnology, Karlsruhe Institute of Technology (KIT). I was fortunate to have the chance to work with Dr. Ravi Kumar, who helped me with the liquid microdroplets stamping work using stamping machine NLP 2000. I have enjoyed my stay in KIT.

I am very grateful to Prof. Dr. Dirk Enke, Bastian Oberleiter and Richard Kohns from University of Leipzig for their kind supply of controlled pore glasses (CPGs). Without their help, I could not finish the project of liquid microdroplets stamping. Also, many thanks to Prof. Dr. Uwe Beginn and Ms. Juliane Kiemstedt at our institute for the GPC measurement of commercial poly(1-decene).

I am also very thankful to our technical assistants, Heinrich Tobergte, Schulz-Kölbel Christine, and Claudia Heß, who helped me a lot with preparation of AAO templates, chemicals booking and supported me by doing SEM. Many thanks to all my lab collegues (especially, Dr. Helmut Schaefer, Dr. Gitte Graubner, Dr. Sachar Ichilmann, Dr. Anna Eichler-Volf, Dr. Mercedes Schmidt, Dr. Leiming Guo, Ruza Periz, Michael Philippi, Fernando Vazquez Luna, Qaiser Ali Khan, Wajiha Akram, Weijia Han, and Fatih Alarslan) for their support, helpful discussions and pleasant time spent together. I would also like to thank Ms. Barbara Gunkel, secretary of our group, who has helped me a lot for my life here in Osnabrueck.

Finally, I take this opportunity to thank my parents, parents-in-law, and my two sisters in China for their long-term encouragement. Many heartfelt thanks should go out to my wife Feifei Zou for her love all these years for supporting me whenever I have difficulties. Most of all, many thanks to my two cute sons Minmu Hou and Xuwen Hou from the bottom of my heart. You are the most precious gift that life could have made me. I love you forever!

List of publications

(A) Publications that report results of this thesis

1. **Hou, P.**; Steinhart, M.; et al., Scanner-based capillary stamping. To be submitted.

2. **Hou, P.**; Steinhart, M., Immobilization of water drops on hydrophobic surfaces by contact line pinning at nonlithographically generated polymer microfiber rings. *Advanced Materials Interfaces* **2018,** *5* (24), 1801191.

3. **Hou, P.**; Han, W.; Philippi, M.; Schäfer, H.; Steinhart, M., Nanostructured submicron block copolymer dots by sacrificial stamping: a potential preconcentration platform for locally resolved sensing, chemistry, and cellular interactions. *ACS Applied Nano Materials* **2018,** *1* (3), 1413-1419.

(B) Other publications

4. Han, W.; **Hou, P.**; Sadaf, S.; Schäfer, H.; Walder, L.; Steinhart, M., Ordered topographically patterned silicon by insect-inspired capillary submicron stamping. *ACS applied materials & interfaces* **2018,** *10* (8), 7451-7458.

5. Schäfer, H.; Küpper, K.; Schmidt, M.; Müller-Buschbaum, K.; Stangl, J.; Daum, D.; Steinhart, M.; Schulz-Kölbel, C.; Han, W.; Wollschläger, J.; **Hou, P.**; Liu, X., Steel-based electrocatalysts for efficient and durable oxygen evolution in acidic media. *Catalysis Science & Technology* **2018,** *8* (8), 2104-2116.

6. Han, W.; Kuepper, K.; **Hou, P.**; Akram, W.; Eickmeier, H.; Hardege, J.; Steinhart, M.; Schäfer, H., Free-sustaining three-dimensional S235 steel-based porous electrocatalyst for highly

99

efficient and durable oxygen evolution. *ChemSusChem* **2018,** *11* (20), 3661-3671.

Curriculum Vitae

First Name	Peilong
Family Name	Hou
Date of Birth	March 10, 1987
Place of Birth	Linyi City, Shandong Province, China
Nationality	Chinese
E-mail	peilong.hou@uos.de; peilong.hou@hotmail.com

EDUCATION

11/2015-10/2019: Ph.D. in Physical Chemistry, University of Osnabrueck, Germany

Supervisor: Prof. Dr. Martin Steinhart

Research Topic: Nanoporous block copolymer stamps: design and applications

09/2012-06/2015: Master in Polymer Science, Renmin University of China, China

Supervisor: Prof. Dr. Zhaoxia Jin

Research Topic: Self-assembly of block-copolymer under confinement

09/2008-07/2012: B.S. in Chemistry, Xiamen University, China

Supervisor: Prof. Dr. Shunhua Li

Research Topic: Fluorescent probe with light-triggered allosteric response

Statement of Authorship

I hereby declare that this doctoral thesis describes my own work, unless otherwise acknowledged in the text. I have not used any sources other than those listed in the bibliography and identified as references. I further declare that I have not submitted this thesis at any other institution in order to obtain a degree.

October 2019, Osnabrueck   Signature